

arXiv:2207.04919v1 [nucl-th] 11 Jul 2022

Nuclear fission and fusion in a random-walk model

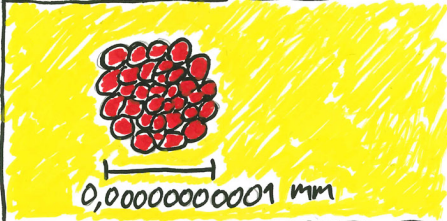
MARTIN ALBERTSSON

FACULTY OF SCIENCE | DEPARTMENT OF PHYSICS | LUND UNIVERSITY 2021

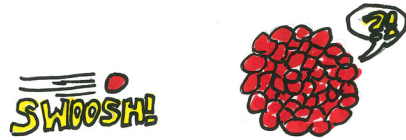


NUCLEAR ENERGY

1 AN ATOMIC NUCLEUS IS A COLLECTION OF NUCLEONS.



2 SOME NUCLEI WILL FISSION INTO TWO FRAGMENTS WHEN HIT BY A NEUTRON.



3 THE TWO RESULTING FRAGMENTS WILL FLY AWAY VERY FAST AND COLLIDE WITH NEARBY ATOMS, WHICH WILL TURN THE SURROUNDING WATER INTO STEAM.



4 THE TWO FRAGMENTS WILL ALSO EMIT NEUTRONS, WHICH CAN INDUCE FISSION OF OTHER NUCLEI, THIS CREATING A CHAIN REACTION.



5 THE GENERATED STEAM IS THEN USED TO POWER TURBINES, WHICH IN TURN PRODUCES ELECTRICITY THROUGH ELECTRIC GENERATORS.



6 THIS IS HOW ELECTRICITY IS GENERATED IN NUCLEAR REACTORS.



Nuclear fission and fusion in a random-walk model

Nuclear fission and fusion in a random-walk model

by Martin Albertsson



LUND
UNIVERSITY

Thesis for the degree of Doctor of Philosophy in Engineering
Thesis advisors: B. Gillis Carlsson, Sven Åberg, Andrea Idini
Faculty opponent: Christelle Schmitt

To be presented, with the permission of the Faculty of Engineering of Lund University, for public criticism in the Rydberg lecture hall (Rydbergsalen) at the Department of Physics on Thursday, the 17th of June 2021 at 09:00.

Organization LUND UNIVERSITY Department of Physics Box 118 SE-221 00 LUND Sweden		Document name DOCTORAL DISSERTATION	
		Date of disputation 2021-06-17	
		Sponsoring organization	
Author Martin Albertsson			
Title Nuclear fission and fusion in a random-walk model			
Abstract <p>This dissertation deals with theoretical descriptions of nuclear fission and synthesis of super-heavy elements via fusion. The associated shape evolutions are treated using a random-walk approach where both the potential energy and the nuclear level density influence the dynamics. The dissertation consists of seven original research papers, and an introductory part providing background information and some additional details of the studies.</p> <p>Paper I contains results for fission-fragment neutron multiplicities in $^{235}\text{U}(n, f)$ using an energy partition based on shape-dependent microscopic level densities.</p> <p>Paper II gives results regarding the energy dependence of fission-fragment neutron multiplicities in $^{235}\text{U}(n, f)$, using the same method as in Paper I.</p> <p>Paper III presents calculations of fission-fragment mass and total-kinetic-energy distributions following fission of the fermium isotopes $^{256,258,260}\text{Fm}$ at low excitation energies. A transition from asymmetric fission in ^{256}Fm to symmetric fission in ^{258}Fm is obtained with a correlated large change in total kinetic energy.</p> <p>Paper IV provides results of fission-fragment mass and total-kinetic-energy distributions following fission of even-even nuclei in the region $74 \leq Z \leq 126$ and $92 \leq N \leq 230$. An island of asymmetric fission is obtained in the superheavy region where the heavy fragment is found to be close to ^{208}Pb and a corresponding light fragment.</p> <p>Paper V presents calculations of neutron multiplicities from fission fragments with specified mass numbers for events having a specified total fragment kinetic energy in $^{235}\text{U}(n, f)$. With increasing neutron energy a superlong fission mode is found to grow increasingly prominent.</p> <p>Paper VI studies the persistence of the symmetric super-short fission mode versus both particle number and excitation energy of even fermium isotopes $^{254-268}\text{Fm}$.</p> <p>Paper VII investigates the shape dynamics in the fusion process in production of superheavy elements and how this competes with quasifission.</p>			
Key words fission, Brownian shape motion, energy partition, neutron multiplicity, kinetic energy, fusion, quasifission			
Classification system and/or index terms (if any)			
Supplementary bibliographical information		Language English	
ISSN and key title		ISBN 978-91-7895-869-6 (print) 978-91-7895-870-2 (pdf)	
Recipient's notes		Number of pages 130	Price
		Security classification	

I, the undersigned, being the copyright owner of the abstract of the above-mentioned dissertation, hereby grant to all reference sources the permission to publish and disseminate the abstract of the above-mentioned dissertation.

Signature _____

Date 2021-05-10 _____

Nuclear fission and fusion in a random-walk model

by Martin Albertsson



LUND
UNIVERSITY

This thesis consists of two parts. An introductory text puts the research work into context and summarizes the results of the papers. Then, the research publications themselves are reproduced, together with a description of my individual contribution. The research Papers I-V are published, Paper VI has been submitted for publication, and Paper VII is a manuscript in preparation.

Cover illustrations: Artistic rendition of the island of stability (front cover) and cartoon describing how nuclear energy is extracted in nuclear reactors (back cover) made by the author.

Funding information: The thesis work was financially supported by Knut and Alice Wallenberg Foundation (Grant No. KAW 2015.0021).

© Martin Albertsson 2021

Faculty of Engineering, Department of Physics

ISBN: 978-91-7895-869-6 (print)

ISBN: 978-91-7895-870-2 (pdf)

Printed in Sweden by Media-Tryck, Lund University, Lund 2021



*Harmony makes small things grow,
lack of it makes great things decay*

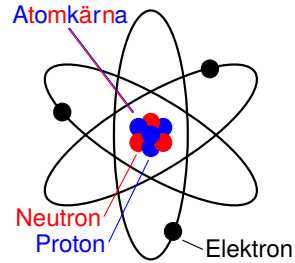
Sallust

Acknowledgements

I would like to thank my excellent thesis advisors, Gillis Carlsson, Sven Åberg and Andrea Idini for giving me the opportunity to do research with them in the exciting field of nuclear physics. I am very grateful to Thomas Døssing, Jørgen Randrup and Peter Möller for introducing me to low-hanging fruits and sharing their immense knowledge. Also, I wish to thank all the great people at mathematical physics for providing an inspiring and uplifting atmosphere. Lastly, I would like to thank my family for everything.

Populärvetenskaplig sammanfattning på svenska

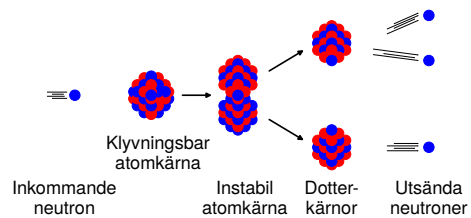
All materia som vi normalt observerar består av atomer. Väte består av väteatomer, syre består av syreatomer och så vidare. En enskild atom utgörs av cirkulerande elektroner omkring en liten atomkärna. Om atomen skulle ha en diameter på 50 meter skulle atomkärnan vara lika stor som en ärtä. Atomkärnan är en samling av protoner och neutroner (kärnpartiklar) som sitter ihop. Antalet protoner Z i kärnan bestämmer vilket grundämne och antalet neutroner N vilken isotop som atomen utgör.



Många olika kombinationer av antal protoner och neutroner kan sättas samman och bilda en atomkärna, men de flesta atomkärnor är inte stabila utan sönderfaller efter en tid. Att en atomkärna sönderfaller innebär att byggstenarna i atomkärnan spontant ändrar om sig till en energimässigt mer gynnsam konfiguration.

Fission

Fission av tunga element är det sönderfall som frigör mest energi och innebär en delning i två mindre dotterkärnor som flyger iväg med en fart på ungefär 10000 mil per sekund. Detta kan användas till att koka vatten, producera ånga, och driva en ångturbin,

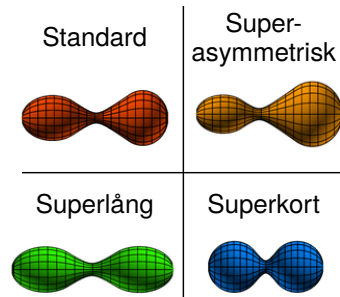


vilket i sin tur kan generera elektricitet. Vid fission av ett gram uran frigörs lika mycket energi som när 3 ton olja bränns eller när 100 000 ton vatten faller 100 meter. Fission av tunga kärnor kan induceras genom beskjutning med en neutron. De resulterande dotterkärnorna sänder sedan ut neutroner som kan inducera fission av en ny atomkärna, och därmed resultera i en kedjereaktion. Detta är den grundläggande processen som utnyttjas för att generera energi i dagens kärnkraftsreaktorer.

I den här avhandlingen används en teoretisk modell för beskrivningen av fission där processen framförallt antas ske väldigt långsamt, ungefär som när en klump sirap delar sig. Under detta antagande kan formändringen i fissionsprocessen modelleras som en slumpvandring i ett energilandskap som beror på formen hos kärnan. Vandringen startar i en punkt motsvarande en sfärisk form och slutar när man kommit till en punkt som motsvarar en delning i två mindre bitar.

I artikel IV tillämpas modellen på alla atomkärnor som teoretiskt sett kan fissionera för att beräkna sannolikheten att en kärna delar sig i specifika dotterkärnor och hur snabbt de flyger iväg. Det är sedan länge känt att de vanligaste fissionerande kärnorna som uran och plutonium föredrar att dela sig i en stor och en liten dotterkärna, där den stora dotterkärnan är ungefär tenn-132. Denna kärnan är väldigt speciell eftersom kvantmekaniska effekter gör att den är stabilare än förväntat, vilket resulterar i en sfärisk form med starkt bundna partiklar. Denna specifika typ av delning sägs motsvara en “standard fissionsmod” vilket innebär en särskild form hos kärnan precis innan den delar sig och som påverkar farten hos dotterkärnorna och antal neutroner de utsänder. I studien framkom ett liknande fenomen för kärnor med $Z \approx 110$ där kärnan delar sig i en väldigt stor dotterkärna och en väldigt liten dotterkärna, som därför kallas super-asymmetrisk mod, där den stora dotterkärnan motsvarar den stabila kärnan bly-208. För tillfället finns det dock inte tillräckligt med experiment för att påvisa om detta stämmer.

Efter delningen så är de två resulterande dotterkärnorna varma och de avger denna värmen genom att sända ut neutroner. Ett mysterium har varit varför den stora dotterkärnan tenn-132 sänder ut färre neutroner än den motsvarande lilla dotterkärnan, eftersom detta strider mot enkla statistiska förväntningar. I artikel I antas att termisk jämvikt hinner uppnås precis innan den delar sig, vilket innebär att den



tillgängliga värmen fördelas baserat på de olika tillstånden i dotterkärnorna. En kvantmekanisk modell används för att beräkna dessa tillstånd där stabiliteten hos tenn-132 innebär få tillstånd och därmed mindre andel av värmen i uppdelningen. Detta i sin tur resulterar i färre antal utsända neutroner från tenn-132. När den inkommande neutronens fart ökar så försvinner effekten av stabiliteten hos tenn-132. Den får därmed större andel av värmen och sänder därför ut fler neutroner, vilket även har observerats i experiment. I artikel II beräknas hur summan av antalet neutroner från de två dotterkärnorna ändras när farten hos den inkommande neutronen ändras och vad sannolikheten är för att sända ut ett specifikt antal neutroner.

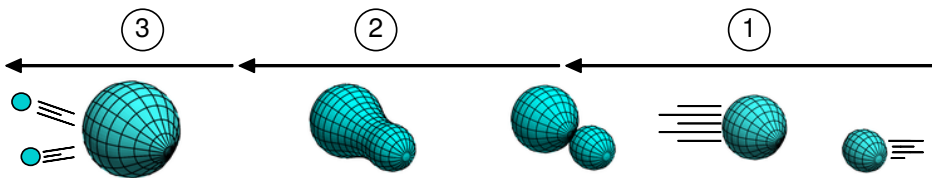
Fission är en kvantmekanisk process vilket innebär att identiska experiment kan ge olika utfall. I experiment utförs därför samma försök många gånger för att på så sätt ta fram sannolikhetsfördelningar över olika kvantiteter. Den teoretiska modell som tillämpas i avhandlingen bygger på samma princip och kan därmed även beskriva korrelationer mellan olika kvantiteter. Detta studeras för fission

av uran-236 i artikel V där det bland annat beräknas hur många neutroner en specifik dotterkärna utsänder i medeltal då den åker iväg med en specifik fart. De beräknade resultaten stämmer väl överens med de experimentella resultaten då den inkommande neutronen har låg fart. I det fallet blir tenn-132 nära sfärisk motsvarande standardmoden och sänder ut få neutroner. När farten på den inkommande neutronen ökar så framkommer istället en "superlång mod" kring tenn-132, där den får en utdragen form och sänder ut många neutroner om den får liten hastighet. Motsvarande experiment för högre fart har ännu inte utförts.

En unik observation är att vissa isotoper av fermium har möjlighet att dela sig i två nästan sfäriska tenn-132 kärnor. Detta innebär att fission sker i en superkort mod där dotterkärnorna flyger iväg väldigt fort och sänder ut få neutroner. I artikel III undersöks hur fermium-256 fissionerar i standardmoden, medan fermium-260 fissionerar i den superkorta moden. För fermium-258 erhålls att båda moderna kan samexistera, allt i enlighet med experiment. I artikel VI undersöks vidare hur den superkorta moden övergår till standardmoden då den initiala energin hos kärnan ökar.

Skapande av nya grundämnen via fusion

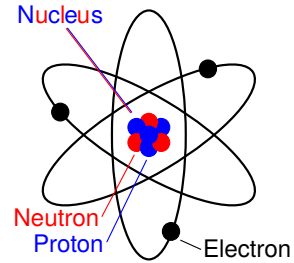
I det periodiska systemet är alla kända grundämnen ordnade efter deras ökande antal protoner, och även kemiska och fysikaliska egenskaper. Det tyngsta grundämne som finns i någorlunda kvantiteter i naturen är uran med 92 protoner. Tyngre grundämnen har dock skapats i laboratorier vanligtvis genom fusion där två lättare kärnor slås ihop. Det tyngsta grundämne som hittills har skapats har 118 protoner och namngavs 2016 till oganesson efter den ryske kärnfysikern Yuri Oganessian. På grund av den väldigt låga sannolikheten för att ett nytt grundämne faktiskt ska bildas vid fusion så krävs pålitliga teoretiska modeller för olika reaktioner och energier för planeringen av sådana experiment.



Fusionsprocessen kan ungefärligt beskrivas som den motsatta processen till fission och kan schematiskt delas upp i tre steg: (1) de två kolliderande kärnorna kommer i kontakt med varandra, (2) de två kärnorna bildar en ny sammansatt kärna, (3) den sammansatta atomkärnan kyls av genom utsändning av neutroner. I artikel VII undersöks hur formändringen i steg (2) sker genom att tillämpa samma modell som används för beskrivningen av fission.

Popular summary in English

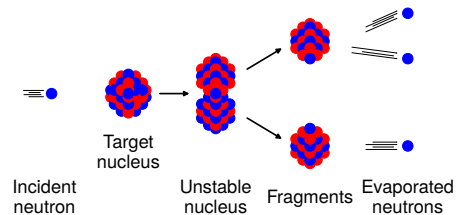
All matter that we normally observe is made of atoms. An atom consists of orbiting electrons around a tiny nucleus. If the atom would have a diameter of 50 meter, then the nucleus would be the size of a pea. The nucleus is a collection of protons and neutrons (nucleons) glued together. The number of protons Z in the nucleus determines the element and the number of neutrons N determines the isotope.



Many different combinations of the number of protons and neutrons can be combined into an atomic nucleus, but most atomic nuclei are not stable but decay after some time. That a nucleus decays means that the constituents in the nucleus spontaneously rearrange to a more energetically favourable configuration.

Fission

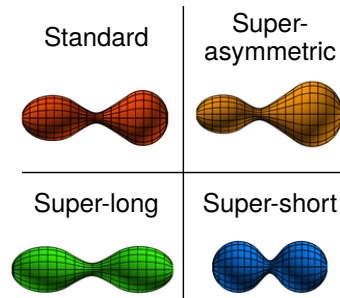
Fission of heavy elements is the decay mode in which the largest amount of energy is released and corresponds to a split into two smaller daughter nuclei that fly away with a speed of about 100 000 km per second. This can be utilized to boil water, produce steam, power a steam turbine, which in turn can generate electricity. Fission of one gram of uranium releases the same amount of energy as when 3 tons of oil is burnt or when 100 000 tons of water falls 100 meters. Fission of heavy nuclei can be induced by bombardment of a neutron. The resulting daughter nuclei then emit neutrons that can induce fission of another nucleus, and thus creating a chain reaction. Fission is the process used to generate energy in today's nuclear reactors.



In this thesis a theoretical model is used for the description of fission where the process is assumed to be very slow, somewhat like when a chunk of syrup splits. The shape evolution in the fission process can under this assumption be modeled as a random walk in an energy landscape which depends on the shape of the nucleus. The random walk starts at a point corresponding to a spherical shape and stops when a point is reached corresponding to a split into two smaller pieces.

In paper IV the model is applied to all nuclei that theoretically can fission in order to calculate the probability that a nucleus splits into two specific daughter nuclei and how fast they fly away. It has long been known that the most common fissioning nuclei like uranium and plutonium prefer to split in one heavy and one light daughter nucleus, where the heavy one is roughly the nucleus tin-132. This nucleus is very special since quantum mechanical effects make it more stable than expected, leading to a spherical form with tightly bound particles. This specific type of split is referred to as a “standard fission mode” which corresponds to a certain shape of the nucleus just before it splits and which affects the speed of the daughter nuclei and the number of neutrons emitted. In the study a similar phenomenon appeared for nuclei with $Z \approx 110$ where the nucleus splits into one very heavy and one very light daughter nucleus, thus called super-asymmetric mode, where the heavy daughter nucleus corresponds to the stable lead-208. At the moment there are not enough experimental data to say if this is the case.

The two resulting daughter nuclei are warm after the split and they get rid of this heat by evaporating neutrons. A mystery has been why tin-132 emits less neutrons than the corresponding light daughter nucleus, since this appears to differ from simple statistical expectations. In Paper I it is assumed that thermal equilibrium is achieved right before it splits, which implies that the available heat is divided



based on the different states in the two daughter nuclei. A quantum-mechanical model is used to calculate these states where the stability of tin-132 implies few states and therefore less share of the heat. This in turn results in less neutrons emitted from tin-132. When the incident neutron’s speed is increased the effect of the stability in tin-132 disappears. It then obtains a larger share of the heat and thus emits more neutrons, which have also been observed in experiments. In Paper II, the sum of the number of neutrons emitted from the two daughter nuclei is calculated when the speed of the incident neutron changes and what the probability is that a specific number of neutrons will be emitted.

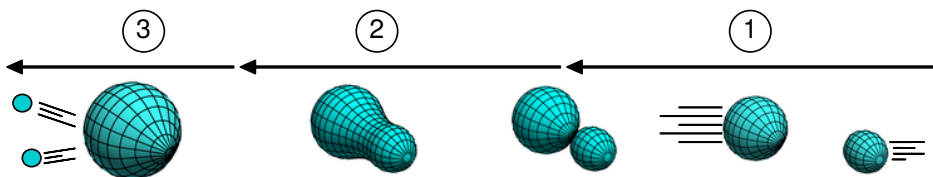
Fission is a quantum-mechanical process which means that identical experiments can generate different outcomes. An experiment is therefore repeated many times in order to acquire probability distributions of various quantities. The theoretical model used in the thesis is based on the same principle and can therefore describe correlations between quantities. This is investigated for fission of uranium-236 in Paper V, where it is studied how many neutrons a specific daughter nucleus emits on average when it flies away with a specific speed. The

calculated results compare well with the experimental results when the speed of the incident neutron is low. In that case, tin-132 becomes almost spherical according to the standard mode and emits few neutrons. When the speed of the incident neutron increases a “superlong mode” appears around tin-132, where it obtains a more elongated shape and emits many neutrons if it flies away slowly.

A unique observation is that certain isotopes of fermium has the possibility to split into two almost spherical tin-132 nuclei. This implies that fission occur in a “super-short” mode where the daughter nuclei fly away very fast and emits few neutrons. In Paper III it is investigated how fermium-256 fission in the standard mode, while fermium-260 fission in the super-short mode. For fermium-258 both modes exist, in accordance with experiments. Paper VI investigates further how the super-short mode transitions to the standard mode when the initial energy of the nucleus is increased.

Creation of new elements via fusion

The period table is a collection of all the known elements organized according to their proton number, and also their chemical and physical properties. The heaviest element occurring in Nature in appreciable quantities is uranium with 92 protons. Heavier elements have however been produced in laboratories through fusion where two lighter nuclei collide with each other. The heaviest element that so far has been produced has 118 protons and was in 2016 named to oganesson after the Russian nuclear physicist Yuri Oganessian. Due to the very low probability that a new element will actually be produced in fusion reactions, reliable theoretical models for different reactions and energies are needed for planning of these kinds of experiments.



The fusion process can roughly be described as the opposite process to fission and can schematically be divided into three steps: (1) the two colliding nuclei come into contact with each other, (2) the two nuclei form a compound nucleus, (3) the compound nucleus cools down by emitting neutrons. The shape evolution in step (2) is investigated in Paper VII by applying the same model used in the description of fission.

List of publications

This thesis is based on the following publications, referred to by their Roman numerals. All papers are reproduced with permission of their respective publishers.

- I **Excitation energy partition in fission**
M. Albertsson, B.G. Carlsson, T. Døssing, P. Möller, J. Randrup, S. Åberg
Phys. Lett. B **803**, 135276 (2020)

- II **Energy dependence of fission-fragment neutron multiplicity in $^{235}\text{U}(n,f)$**
M. Albertsson
Acta Phys. Pol. B **12**, 499 (2019)

- III **Fission modes in fermium isotopes with Brownian shape-motion model**
M. Albertsson, B.G. Carlsson, T. Døssing, P. Möller, J. Randrup, S. Åberg
EPJ Web of Conferences **223**, 01002 (2019)

- IV **Calculated fission-fragment mass yields and average total kinetic energies of heavy and superheavy nuclei**
M. Albertsson, B.G. Carlsson, T. Døssing, P. Möller, J. Randrup, S. Åberg
Eur. Phys. J. A **56**, 46 (2020)

- V **Correlation studies of fission fragment neutron multiplicities**
M. Albertsson, B.G. Carlsson, T. Døssing, P. Möller, J. Randrup, S. Åberg
Phys. Rev. C **103**, 014609 (2021), Editor's suggestion

VI The super-short fission mode in fermium isotopes

M. Albertsson, B.G. Carlsson, T. Døssing, P. Möller, J. Randrup, S. Åberg

Submitted to Phys. Rev. Lett. (2021)

VII Fusion-quasifission dynamics in a random-walk model

M. Albertsson, B.G. Carlsson, T. Døssing, P. Möller, J. Randrup, D. Rudolph, S. Åberg

Work in progress

Publications not included in this thesis:

Spectroscopy along flerovium decay chains: Discovery of ^{280}Ds and an excited state in ^{282}Cn

A. Sâmark-Roth, D.M. Cox, D. Rudolph, L.G. Sarmiento, B.G. Carlsson, J.L. Egido, P. Golubev, J. Heery, A. Yakushev, S. Åberg, H.M. Albers, **M. Albertsson**, M. Block, H. Brand, T. Calverley, R. Cantemir, R.M. Clark, Ch.E. Düllman, J. Eberth, C. Fahlander, U. Forsberg, J.M. Gates, F. Giacoppo, M. Götz, S. Götz, R.-D. Herzberg, Y. Hrabar, E. Jäger, D. Judson, J. Khuyagbaatar, B. Kindler, I. Kojouharov, J.V. Kratz, J. Krier, N. Kurz, L. Lens, J. Ljungberg, B. Lommel, J. Louko, C.-C. Meyer, A. Mistry, C. Mokry, P. Papadakis, E. Parr, J.L. Pore, I. Ragnarsson, J. Runke, M. Schädel, H. Schaffner, B. Schausten, D.A. Shaughnessy, P. Thörle-Pospiech, N. Trautmann, J. Unusitalo
Phys. Rev. Lett. **126**, 032503 (2021)

Spectroscopy along flerovium decay chains

A. S amark-Roth, D.M. Cox, D. Rudolph, L.G. Sarmiento, B.G. Carlsson, J.L. Egido, P. Golubev, J. Heery, A. Yakushev, S.  berg, H.M. Albers, **M. Albertsson**, M. Block, H. Brand, T. Calverley, R. Cantemir, R.M. Clark, Ch.E. D ullman, J. Eberth, C. Fahlander, U. Forsberg, J.M. Gates, F. Giacoppo, M. G tz, S. G tz, R.-D. Herzberg, Y. Hrabar, E. J ager, D. Judson, J. Khuyagbaatar, B. Kindler, I. Kojouharov, J.V. Kratz, J. Krier, N. Kurz, L. Lens, J. Ljungberg, B. Lommel, J. Louko, C.-C. Meyer, A. Mistry, C. Mokry, P. Papadakis, E. Parr, J.L. Pore, I. Ragnarsson, J. Runke, M. Sch adel, H. Schaffner, B. Schausten, D.A. Shaughnessy, P. Th rle-Pospiech, N. Trautmann, J. Unusitalo
To be submitted to Phys. Rev. C

Spectroscopy along flerovium decay chains: Fine structure in odd- A ^{289}Fl and a note on ^{290}Fl

D.M. Cox, A. S amark-Roth, D. Rudolph, L.G. Sarmiento, B.G. Carlsson, J.L. Egido, P. Golubev, J. Heery, A. Yakushev, S.  berg, H.M. Albers, **M. Albertsson**, M. Block, H. Brand, T. Calverley, R. Cantemir, R.M. Clark, Ch.E. D ullman, J. Eberth, C. Fahlander, U. Forsberg, J.M. Gates, F. Giacoppo, M. G tz, S. G tz, R.-D. Herzberg, Y. Hrabar, E. J ager, D. Judson, J. Khuyagbaatar, B. Kindler, I. Kojouharov, J.V. Kratz, J. Krier, N. Kurz, L. Lens, J. Ljungberg, B. Lommel, J. Louko, C.-C. Meyer, A. Mistry, C. Mokry, P. Papadakis, E. Parr, J.L. Pore, I. Ragnarsson, J. Runke, M. Sch adel, H. Schaffner, B. Schausten, D.A. Shaughnessy, P. Th rle-Pospiech, N. Trautmann, J. Unusitalo
To be submitted to Phys. Rev. Lett.

List of figures

1.1	Periodic table of elements	9
1.2	Structure of the atom	9
1.3	Binding energy per nucleon	12
1.4	Decay modes of nuclei	13
2.1	Three-quadratic-surface parametrization	19
2.2	Mass difference $M_{\text{exp}} - M_{\text{th}}$ in FRLDM	22
4.1	Fission barriers with LDM	34
4.2	Chart of fission-barrier heights in FRLDM	35
4.3	Fission-mode shapes	37
4.4	Fission valleys in ^{236}U	38
4.5	Fission valleys in $^{256,258,260,262}\text{Fm}$	39
4.6	Fission valleys in ^{274}Hs	40
6.1	Fission-fragment mass yields in $^{235}\text{U}(\text{n}, \text{f})$	48
6.2	Chart of fission-fragment mass yields	49
6.3	Systematics of fission-fragment mass numbers	50
6.4	Fission-fragment mass yields in ^{274}Hs , ^{278}Cn , ^{284}Ds	51
6.5	Fission-fragment mass yields in $^{256,258,260}\text{Fm}$	51
6.6	Fragment deformations in $^{235}\text{U}(\text{n}, \text{f})$ for $E_{\text{n}} = 0, 5.55, 14$ MeV	53
6.7	Fragment deformations vs. q_2 in $^{235}\text{U}(\text{n}, \text{f})$ for $E_{\text{n}} = 0$ MeV	54
6.8	Fragment deformations vs. q_2 in $^{235}\text{U}(\text{n}, \text{f})$ for $E_{\text{n}} = 5.55$ MeV	55
6.9	Fragment deformations in ^{260}Fm for $E_0^* = 0, 6.13, 50$ MeV	56
6.10	Phase diagram of fission modes in fermium isotopes	57
6.11	Fragment deformations in ^{274}Hs for $E_0^* = 6.7, 10$ MeV	57
7.1	Energies in the fission process	60
7.2	TKE vs. A in $^{235}\text{U}(\text{n}, \text{f})$ for $E_{\text{n}} = 0$ and 5.55 MeV	62
7.3	Contour figure of TKE in $^{235}\text{U}(\text{n}_{\text{th}}, \text{f})$	63
7.4	Chart of fission-fragment total kinetic energy	64
7.5	Viola TKE systematics minus calculated average TKE	64
7.6	TKE yields in $^{256,258,260}\text{Fm}$ for SF and thermal energy	65

7.7	Contour figure of total kinetic energy in ^{260}Fm	66
7.8	Energy dependence of TKE in fission of fermium isotopes	67
7.9	Contour figure of total kinetic energy in ^{274}Hs	68
7.10	Energy-partition distributions in $^{235}\text{U}(\text{n}, \text{f})$	69
7.11	Fragment excitation energy vs. A in $^{235}\text{U}(\text{n}_{\text{th}}, \text{f})$	70
7.12	Bimodal fission in $^{235}\text{U}(\text{n}, \text{f})$	71
8.1	Neutron energy spectrum	75
8.2	$\bar{\nu}$ vs. A in $^{235}\text{U}(\text{n}_{\text{th}}, \text{f})$	76
8.3	$P(\nu_{\text{tot}})$ in $^{235}\text{U}(\text{n}_{\text{th}}, \text{f})$	76
8.4	$\bar{\nu}$ vs. A in $^{235}\text{U}(\text{n}, \text{f})$ for $E_{\text{n}} = 0.5, 5.55, 14$ MeV	77
8.5	$\bar{\nu}(A)$ and $P(\nu_{\text{tot}})$ in ^{260}Fm for $E_0^* = 0, 6.13, 15$ MeV	78
8.6	Energy dependence of $\bar{\nu}_{\text{tot}}$ in fission of fermium isotopes	78
8.7	$\bar{\nu}(A)$ and $P(\nu_{\text{tot}})$ in ^{274}Hs for $E_0^* = 0, 6.7, 10$ MeV	79
8.8	Neutron multiplicity systematics	81
8.9	$\bar{\nu}(A, \text{TKE})$ in $^{235}\text{U}(\text{n}, \text{f})$ for $E_{\text{n}} = 0$ MeV	82
8.10	$\bar{\nu}(A, \text{TKE})$ in $^{235}\text{U}(\text{n}, \text{f})$ for $E_{\text{n}} = 5.55$ MeV	83
9.1	Schematic depiction of the fusion process	86
9.2	Potential energy vs. (α, q_2) for ^{258}Rf	87
9.3	Potential energy vs. q_2 for $^{256}\text{No}, ^{258}\text{Rf}, ^{262}\text{Sg}, ^{266}\text{Hs}$	88
9.4	Neck radius and friction coefficient along fusion valley in ^{258}Rf	89
9.5	Neck radii along fusion valley for $^{256}\text{No}, ^{258}\text{Rf}, ^{262}\text{Sg}, ^{266}\text{Hs}$	90
9.6	Fusion and QF trajectories in ^{258}Rf for $E_{\text{CN}}^* = 12$ and 30 MeV	92
9.7	QF events vs. $(A, \text{TKE}_{\text{QF}})$ in ^{258}Rf for $E_{\text{CN}}^* = 12$ and 30 MeV	93

Contents

Acknowledgements	xi
Populärvetenskaplig sammanfattning på svenska	xii
Popular summary in English	xv
List of publications	xviii
List of figures	xxi
I Introduction and background theory	3
1 Introduction	5
1.1 Brief history of nuclear physics	5
1.2 Structure of the nucleus	8
1.3 Nuclear stability and radioactive decay	11
1.4 Thesis outline	14
2 Mass models	17
2.1 Shape parametrization	18
2.2 Macroscopic models	20
2.3 Microscopic corrections	23
3 Nuclear level densities	27
3.1 Fermi-gas level density	27
3.2 Combinatorial level density method	29
II Fission and fusion	31
4 Potential-energy surfaces	33
4.1 Liquid-drop model	33
4.2 Finite-range liquid-drop model	35
5 Fission dynamics	41
5.1 Stochastic dynamics formalism	41
5.2 Metropolis walk method	44
6 Scission quantities	47
6.1 Mass distributions	47

6.2	Shapes of scission fragments	52
7	Energy release	59
7.1	Energies in the fission process	59
7.2	Fragment kinetic energy	61
7.3	Fragment excitation energy	68
8	Neutron evaporation from fragments	73
8.1	Formalism	73
8.2	Neutron multiplicities	75
8.3	Correlations between neutron multiplicities and TKE	82
9	Fusion-quasifission dynamics	85
9.1	Introduction	85
9.2	Method	86
9.3	Simulations	91
10	Outlook	95
	References	99

Part I

Introduction and background theory

Chapter 1

Introduction

1.1 Brief history of nuclear physics

600 B.C. - 400 B.C.: Classical elements

The search for the fundamental nature of matter is a long-standing question and was undertaken in many ancient cultures. One of the earliest known sources of questions regarding this issue date back to the Greek philosophers around 600 B.C. Leucippus and his student Democritus suggested that everything in Nature is made of “atoms” (from the Greek word *atomos* meaning uncuttable) and that different types and combinations of these atoms constituted the various forms of matter [1]. They also argued that there must be considerable open space between these atoms, called the void. This contrasted the theory by Empedocles that the nature of matter could be reduced to the four classical elements - earth, water, air, and fire - which were assumed to be continuous. The theory of the atoms was dismissed by Aristotle and, due to his large influence at the time, the theory of the classical elements became the standard dogma for almost two millennia.

1661 - 1868: Chemical elements

The atomic theory of Democritus was not properly reconsidered until the 17th century. The chemist Robert Boyle proposed that elements are composed of atoms of various types and sizes which can organize themselves into different chemical substances. He defined an element as a substance that could not be

decomposed into other substances. In 1789 Antoine Lavoisier constructed the first modern list of chemical elements which contained 33 elements (of which only 23 are considered chemical elements today). The atomic theory was placed on more solid ground by John Dalton who argued that all matter consists of tiny atoms which are indestructible and unchangeable. He further argued that elements are characterized by the weight of their atoms, and that the atoms combine to form new compounds when elements react. In 1828, Jöns Jakob Berzelius compiled a table of atomic weights relative to oxygen of all the known elements at the time, which supported Dalton's atomic theory.

1869 - 1895: The periodic table of elements

Up until the 1860s the chemists had discovered more than 60 different elements, but they were not sure if there was a system of the elements. The Russian chemist Dmitri Mendeleev organized the elements according to their atomic mass in increasing order, which resulted in the periodic table of elements (see Fig. 1.1 for the most up-to-date version). He noticed that elements with similar properties seemed to be repeated with certain intervals. Although there were gaps in the table, Mendeleev suggested that these gaps corresponded to undiscovered elements. Sure enough, these elements were later discovered.

1896 - 1910: Radioactivity

In 1896 Henri Becquerel discovered radioactivity [2], i.e. the process in which an unstable atomic nucleus loses energy by emitting radiation. This indicated that the atom was neither indivisible nor immutable. In the years that followed, radioactivity was investigated in particular by Marie and Pierre Curie as well as by Ernest Rutherford. Three types of radiation emanating from atoms were discovered which were named α , β , and γ radiation. The discovery of the electron by J.J. Thomson in 1897 [3] was a further indication that the atom had internal structure. This led to the "plum pudding" model in which the atom was a positively charged ball with smaller negatively charged electrons embedded inside it.

1911 - 1932: The atomic nucleus

Experiments done by Rutherford and his colleagues resulted in the Rutherford model of the atom in 1911 [4], in which the atom consists of a small positively

charged massive nucleus surrounded by very distant orbiting negatively charged electrons. The positive charge of the nucleus is due to Z number of protons, each carrying one positive unit of electric charge. It was later discovered in 1932 [5], that the nucleus also contains N number of particles that are very similar to protons but electrically neutral, hence called neutrons.

1934 - 1939: Fission

Since the neutron is electrically neutral it can easily enter the nucleus. This was utilized by Enrico Fermi and his colleagues in 1934 who bombarded ever heavier elements with neutrons. The bombarded nucleus would typically absorb the neutron and then undergo β -decay which would result in an element with higher proton number. After bombarding uranium ($Z = 92$), Fermi concluded that the experiments had created new elements with 93 and 94 protons [6]. Though Fermi received the Nobel price for these discoveries, the German chemist Ida Noddack suggested that instead of creating a new heavier element, that "it is conceivable that the nucleus breaks up into several large fragments" [7]. However, Noddack's suggestion was not pursued at that time.

In 1938, Hahn and Strassmann [8] also bombarded uranium with neutrons and identified barium ($Z = 56$) as one of the products. This large change in proton number then had to be the result of a new type of nuclear transmutation. Meitner and Frisch suggested [9] that the nucleus could be described as a deformable charged liquid drop that had split into two smaller nuclei of roughly equal size. Based on this model, and making use of the mass-energy equivalence $E = mc^2$ discovered by Albert Einstein, Meitner calculated that the energy released in each split would be very high, which soon after was observed by Frisch [10]. The process was named "nuclear fission" in analogy to binary fission of cells in biology.

The Hungarian physicist Leó Szilárd realized that neutron-induced fission of uranium could be used to create a nuclear chain reaction. It would thus be a possibility of generating huge amounts of energy; either for civilian purposes as in electric power generation, but also for military purposes with atomic bombs. In 1939 Szilárd therefore wrote a letter that was signed by Albert Einstein to President Franklin D. Roosevelt, advising him to fund research into the possibility of using nuclear fission as a weapon as Nazi Germany may also be conducting such research [11]. This led to the creation of the Manhattan project that produced the first nuclear weapons.

1935 - 1964: The nuclear force and particle zoo

Since protons repel each other due to the electrical Coulomb force, the nucleus would blow apart if there were not some other force inside the nucleus holding it together. The idea of a new strong nuclear force was therefore introduced and the first theory was developed by the Japanese physicist Hideki Yukawa in 1935 [12]. Similar to the theory of the electromagnetic interaction where the interaction is mediated by a massless photon, the interaction between the nucleons would be mediated by a massive particle called meson.

The meson was eventually discovered in 1947 in cosmic rays, which are highly energetic particles coming from space and entering the earth's atmosphere. The collisions of cosmic rays with nuclei in the air lead to creations of many new exotic particles in "cosmic showers". These cosmic showers could be reproduced in laboratory settings with the developments of high-energy particle accelerators, and ever more particles were discovered through the 1950s and 1960s. Many of them were believed to be elementary particles and the entire collection was nicknamed the "particle zoo". Most of these particles were eventually explained to be combinations of more fundamental particles called quarks introduced by Gell-Mann and Zweig in 1964 [13, 14].

1911 - present: Modeling the nucleus

Ever since the nucleus was discovered in 1911 various models have been developed for describing the nucleus. Nuclei are systems of strongly interacting particles and present many challenging issues. A few of the most common models for modeling the nucleus are described in the following section.

1.2 Structure of the nucleus

The understanding today is that all ordinary matter in the universe is composed of chemical elements, where a chemical element is a species of atoms. The structure of an atom is illustrated in Fig. 1.2. The number of protons Z in the nucleus determines the element and the number of neutrons N determines the isotope. The number of nucleons $A = Z + N$ is called the mass number and the general notation for an element El is ${}^A_Z\text{El}_N$. The properties of the chemical elements are summarized in the periodic table in Fig. 1.1.

The protons and neutrons are themselves composed of smaller particles called

Group	1	2	3	4	5	6	7	8	9	10	11	12	13	14	15	16	17	18					
Period			Alkali metals						Post-transition metals														
1	1 H	Alkaline earth metals						Metalloids						2 He									
2	3 Li	4 Be	Lanthanides						Other non-metals						5 B	6 C	7 N	8 O	9 F	10 Ne			
3	11 Na	12 Mg	Transition metals						Noble gases						13 Al	14 Si	15 P	16 S	17 Cl	18 Ar			
4	19 K	20 Ca	21 Sc	22 Ti	23 V	24 Cr	25 Mn	26 Fe	27 Co	28 Ni	29 Cu	30 Zn	31 Ga	32 Ge	33 As	34 Se	35 Br	36 Kr					
5	37 Rb	38 Sr	39 Y	40 Zr	41 Nb	42 Mo	43 Tc	44 Ru	45 Rh	46 Pd	47 Ag	48 Cd	49 In	50 Sn	51 Sb	52 Te	53 I	54 Xe					
6	55 Cs	56 Ba	Unknown properties						72 Hf	73 Ta	74 W	75 Re	76 Os	77 Ir	78 Pt	79 Au	80 Hg	81 Tl	82 Pb	83 Bi	84 Po	85 At	86 Rn
7	87 Fr	88 Ra	104 Rf	105 Db	106 Sg	107 Bh	108 Hs	109 Mt	110 Ds	111 Rg	112 Cn	113 Nh	114 Fl	115 Mc	116 Lv	117 Ts	118 Og						
	57 La	58 Ce	59 Pr	60 Nd	61 Pm	62 Sm	63 Eu	64 Gd	65 Tb	66 Dy	67 Ho	68 Er	69 Tm	70 Yb	71 Lu								
	89 Ac	90 Th	91 Pa	92 U	93 Np	94 Pu	95 Am	96 Cm	97 Bk	98 Cf	99 Es	100 Fm	101 Md	102 No	103 Lr								

Figure 1.1: Periodic table of elements.

quarks. The quarks are bound together by the strong interaction described by Quantum Chromodynamics. Quarks, gluons and their dynamics are mostly confined within nucleons, but residual influences extend slightly beyond nucleon boundaries to give rise to the nuclear force.

The large variety of nuclear models can broadly be grouped into four different approaches: ab initio methods, shell-model theories, self-consistent mean-field models, and macroscopic-microscopic models.

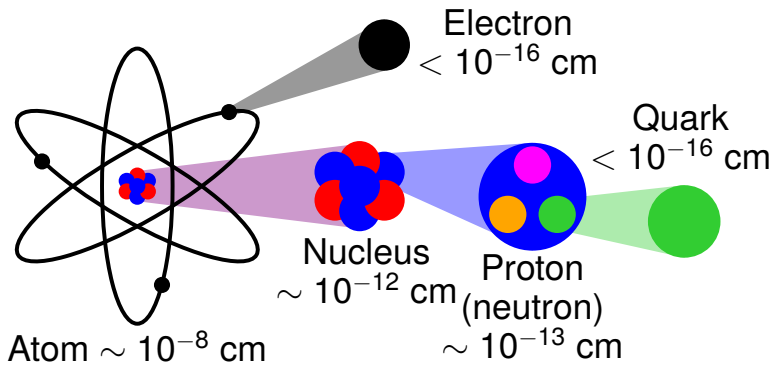


Figure 1.2: Structure of the atom.

1.2.1 Ab initio models

Ab initio models denote models that try to describe the atomic nucleus by solving the non-relativistic Schrödinger equation for all constituent nucleons and the forces between them (see e.g. Ref. [15] for a review).

The first difficult task in ab initio modeling is to obtain a nuclear interaction from the theory of Quantum Chromodynamics. The most promising methods are based on Chiral effective field theory and Lattice QCD.

After arriving at a Hamiltonian \hat{H} one must solve the Schrödinger equation $\hat{H}|\Psi\rangle = E|\Psi\rangle$, where $|\Psi\rangle$ is the many-body wave function of the A nucleons in the nucleus. Various ab initio methods have been devised to numerically find solutions to this equation such as No Core Shell Model or Coupled Cluster. All of these methods are very computationally intensive and are at the moment limited to relatively light nuclei.

1.2.2 Shell models

Nuclei with certain “magic numbers” of protons or neutrons are seen to be especially stable. This observation was the origin of the Non-Interacting Shell Model developed by Eugene Paul Wigner, Maria Goeppert Mayer and J. Hans D. Jensen [16, 17], who shared the 1963 Nobel Prize. Despite the magnitude of the nuclear force, the nucleus is not a very dense system. The nucleons in a nucleus can therefore be considered as independent particles moving on almost unperturbed single-particle orbits governed by some average potential created by all the other nucleons in the nucleus.

The original shell model employs a spherical potential and can explain many features of spherical nuclei near the magic numbers. A modification is needed in order to describe nuclei with nucleon numbers between the magic numbers. This was developed by Sven Gösta Nilsson who considered a deformed potential, which became very successful and is now called the Nilsson Model [18].

Another method of describing nuclei between the magic numbers is to include a residual two-body interaction in a valence space above a closed shell (the core), corresponding to the Interacting Shell model. A configuration-mixing calculation is then performed involving the many-body states in the valence space. This is equivalent to the No Core Shell Model if the core is included in the valence space.

1.2.3 Self-consistent mean-field models

The success of the phenomenologically introduced shell model justifies the assumption that the nucleons approximately move independently in an average potential produced by all the other nucleons. The task then is to extract such a single-particle potential out of the sum of two-body interactions, which can be done with the self-consistent Hartree-Fock method. However, nuclei with an even number of nucleons are systematically more bound than those with an odd one, which implies that each nucleon binds with another one to form a pair. Consequently the system cannot be described as independent particles subjected to a common mean field. The nucleons are then subject to both the mean field potential and to the pairing interaction within the Hartree-Fock-Bogoliubov theory [19].

1.2.4 Macroscopic-microscopic models

Another model is the liquid-drop model (LDM), which is based on observations that a nucleus show similar properties as that of a drop of incompressible fluid. This model parametrizes the energy of the nucleus in terms of macroscopic properties such as volume energy and surface energy. The actual parameters are fitted phenomenologically. The LDM describes very well the average trends of nuclear quantities, but is usually augmented by corrections that approximate the quantum-mechanical effects not taken into account in the LDM. Models which combine the LDM with quantum mechanical corrections are usually called macroscopic-microscopic models. They have been developed to be both highly descriptive of many nuclear properties and have high predictive accuracy for properties not yet measured experimentally. The macroscopic-microscopic method is described in more detail in Sec. 2.

1.3 Nuclear stability and radioactive decay

Since energy must be added to a nucleus to separate it into its individual protons and neutrons, the total rest energy (mass) of the separated nucleons is greater than the rest energy of the nucleons assembled into a nucleus. The energy that must be added to separate the nucleons is called the binding energy E_B . A measure of how tightly a nucleus is bound is the binding energy per nucleon, E_B/A . Experimental binding energies per nucleon are shown in Fig. 1.3 as a function of N and Z . The highest value is approximately at the position of

iron and nickel ($Z \approx 28$, $N \approx 34$), which are therefore the most stable nuclei. Consequently, energy is released in reactions where the end products are closer to iron and nickel.

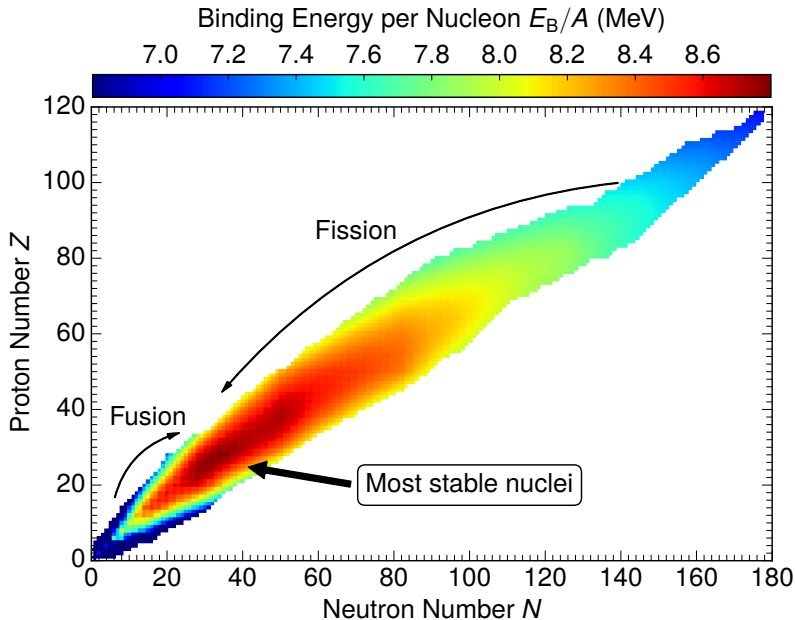


Figure 1.3: Binding energy per nucleon with experimental masses taken from Ref. [20].

1.3.1 Radioactive decay

Different proton and neutron numbers can be combined to form an atomic nucleus, but most nuclei are unstable and decay after some time. Figure 1.4 shows the typical decay modes for known nuclei and correspond to:

1. *Proton/neutron emission*: Proton-rich nuclei can obtain a more stable ratio of protons to neutrons via proton emission (and analogously neutron emission for neutron-rich nuclei).
2. *α -decay*: α -decay means that an atomic nucleus splits into a Helium nucleus (α particle) and a new daughter nucleus with two less protons and two less neutrons. This is typical for heavier nuclei.
3. *β -decay*: A nucleus with excess neutrons can transform a neutron into a proton by the emission of an electron accompanied by an antineutrino. Similarly, proton-rich nuclei can transform a proton into a neutron by

emitting a positron with a neutrino. By this process, unstable nuclei obtain a more stable ratio of protons to neutrons by emitting a β particle (electron or positron).

4. *Spontaneous fission (SF)*: The higher values of binding energy near $A \approx 60$ mean that energy is released when a heavy nucleus with $A \approx 200$ splits into two lighter nuclei that lie closer to $A \approx 60$. SF occur only for heavy nuclei and competes with α -decay.

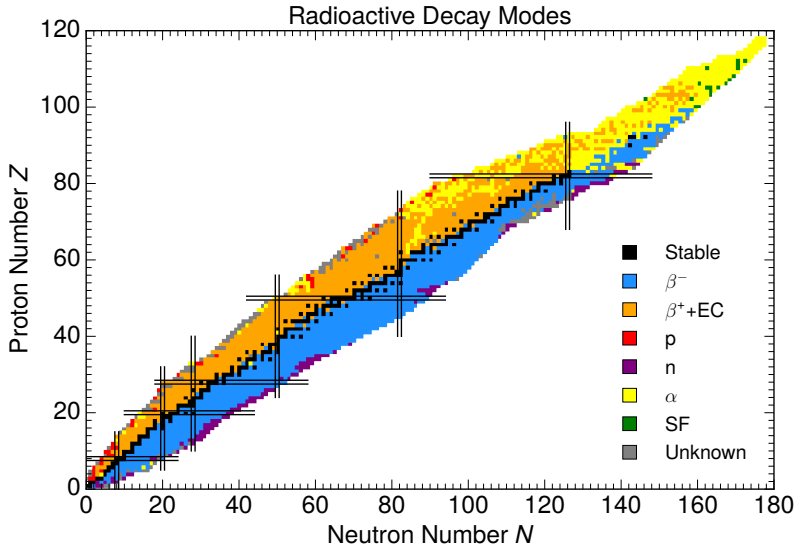


Figure 1.4: Experimental decay modes of nuclei in the form of a nuclear chart [21]. Pairs of parallel lines indicate magic neutron and proton numbers.

1.3.2 Nuclear reactions

While a radioactive decay is a spontaneous event, a nuclear reaction is an induced reaction between a nucleus and some other particle. Two common reactions are:

1. *Induced fission*: In addition to SF, fission can also be induced through a nuclear reaction of a target nucleus with projectiles such as neutrons, protons, α particles or γ rays.
2. *Fusion*: In similar way energy is released when a heavy nucleus fission into two lighter nuclei, energy is also released when two light nuclei with $A \leq 20$ are combined to form a heavier nucleus.

1.3.3 Superheavy elements

The stability or instability of a particular nucleus is determined by the competition between the attractive nuclear force among the protons and neutrons and the repulsive electrical interaction among the protons. For heavy nuclei, the Coulomb repulsion energy grows rapidly, so extra neutrons are required to supply the additional binding energy needed for stability. Eventually, the repulsive forces between protons cannot be compensated for by the addition of more neutrons, because of the asymmetry energy.

The heaviest naturally occurring element in appreciable quantities is uranium with proton number $Z = 92$. However, heavier elements have been produced in laboratories via fusion reactions, neutron capture and nucleon transfer. While energy is released in fusion of light nuclei, energy must be provided in fusion of heavy elements. Superheavy nuclei ($Z \geq 104$) up to $Z = 118$ (oganesson) have been created in experiments. What are the heaviest atomic nuclei that can exist, and thus where the periodic table ends, is an active field of research in nuclear physics and is discussed more in Ch. 9.

1.4 Thesis outline

This thesis presents theoretical descriptions of fission and fusion of heavy elements, where the system evolves from a near-spherical shape towards two separated fragments in fission, and vice versa in fusion. Jørgen Randrup and Peter Möller developed in 2011 a model that simulated the dynamics of the fission process as a random walk in the potential-energy landscape of shapes, based on the assumption that shape evolution is strongly damped [22]. This provided a quantitative description of the shape evolution in fission with predictive power for the fission-fragment mass yield, which sparked an increased activity in the field of fission. The random-walk model was developed further in Ref. [23] by incorporating how microscopically calculated level densities affect the shape evolution.

The work in this thesis extends the random-walk model by, in addition to the previous description of fragment mass yields, also simulating how much kinetic energy the fission-fragments obtain and the number of neutrons they emit, as well as how these two quantities are correlated. The thesis also presents studies of how different ways of fissioning, called fission modes, are present in different nuclei and how the presence of these modes depends on the energy of the system. The model is furthermore applied to the description of the shape evolution in

fusion for production of superheavy elements.

The remainder of this part of the thesis, Part I, is focused on nuclear theory relevant for the subsequent description of fission and fusion in Part II. Ch. 2 describes the employed parametrization of the nuclear shape and calculations of nuclear masses within the macroscopic-microscopic model, while Ch. 3 describes calculations of level densities.

Part II is mostly devoted to the description of fission where particular focus will be on three cases; ^{236}U , fermium isotopes around ^{258}Fm , and ^{274}Hs . Fission barriers and potential-energy surfaces are described in Ch. 4. Fission dynamics within the random-walk model is outlined in Ch. 5. Scission quantities, such as fragment masses and deformations, are presented in Ch. 6. The energy released in fission in terms of kinetic energy and excitation energy is described in Ch. 7. Ch. 8 covers neutron evaporation from fission-fragments. Ch. 9 is devoted to fusion for production of superheavy elements. An outlook on the research of fission and fusion is given in Ch. 10.

Finally, in Part III the scientific publications are included. See the List of publications in the thesis preamble for an overview of the articles. A poster is also presented in the appendix.

Chapter 2

Mass models

The nuclear binding energy E_B is defined as the difference in energy between the nucleus and its constituent protons and neutrons:

$$E_B(N, Z, \text{shape}) = ZM_H + NM_n - E(Z, N, \text{shape}), \quad (2.1)$$

where M_H and M_n are the free neutron and hydrogen atom masses (in units of MeV), and where $E(Z, N, \text{shape})$ is the potential energy of the nucleus.

In the macroscopic-microscopic method the total energy of the nucleus consists of two parts; macroscopic and microscopic. Both parts are calculated at a fixed shape of the nuclear surface. Thus the total nuclear potential energy can be written as

$$E(Z, N, \text{shape}) = E_{\text{mac}}(Z, N, \text{shape}) + E_{\text{mic}}(Z, N, \text{shape}). \quad (2.2)$$

The macroscopic part accounts for most of the energy and describes the smooth variations in energy when N , Z , and the nuclear shape are varied. The microscopic part accounts for the fluctuation of the energy around the smooth trends, due to the shell structure.

A parametrization of the nuclear shape is described in Sec. 2.1. Methods for calculating the macroscopic and microscopic terms are discussed in Sec. 2.2 and 2.3, respectively.

2.1 Shape parametrization

The fact that the nucleus can be considered to have a surface comes from the properties of the nuclear interaction; it is repulsive at short distances but attractive when nucleons are just beyond touching. There is therefore an optimal spacing between neighbouring nucleons to be situated. As a consequence, nuclei have a fairly uniform interior and a relatively thin surface that reflects the short range of the nuclear force. It is therefore reasonable to consider nuclei as incompressible diffuse droplets of nuclear matter.

2.1.1 Three-quadratic surface parametrization

A common shape parametrization for the description of fission is the three-quadratic-surface (3QS) parametrization [24], in which the shape of the nuclear surface is specified in terms of three smoothly joined portions of quadratic surfaces of revolution. In terms of a cylindrical coordinate system, the equation for the nuclear surface can be written explicitly as

$$\rho^2 = \begin{cases} a_1^2 - \frac{a_1^2}{c_1^2}(z - l_1)^2, & l_1 - c_1 \leq z \leq z_1, \\ a_2^2 - \frac{a_2^2}{c_2^2}(z - l_2)^2, & z_2 \leq z \leq l_2 + c_2, \\ a_3^2 - \frac{a_3^2}{c_3^2}(z - l_3)^2, & z_1 \leq z \leq z_2. \end{cases} \quad (2.3)$$

This expression contains 11 parameters and are illustrated in Fig. 2.1(a). However, the conditions of constancy of volume and continuous function and first derivative at z_1 and z_2 reduces it to six numbers. By introducing an auxiliary unit of distance

$$u = \left[\frac{1}{2}(a_1^2 + a_2^2) \right]^{1/2}, \quad (2.4)$$

one can define three symmetric coordinates σ_i and three reflection-asymmetric coordinates α_i as

$$\begin{aligned} \sigma_1 &= \frac{l_2 - l_1}{u}, & \alpha_1 &= \frac{1}{2} \frac{(l_1 + l_2)}{u}, \\ \sigma_2 &= \frac{a_3^2}{c_3^2}, & \alpha_2 &= \frac{(a_1^2 - a_2^2)}{u^2}, \\ \sigma_3 &= \frac{1}{2} \left(\frac{a_1^2}{c_1^2} + \frac{a_2^2}{c_2^2} \right), & \alpha_3 &= \frac{a_1^2}{c_1^2} - \frac{a_2^2}{c_2^2}. \end{aligned} \quad (2.5)$$

The coordinate α_1 is furthermore determined by requiring that the center of mass to be at the origin, so there are only five independent shape coordinates.

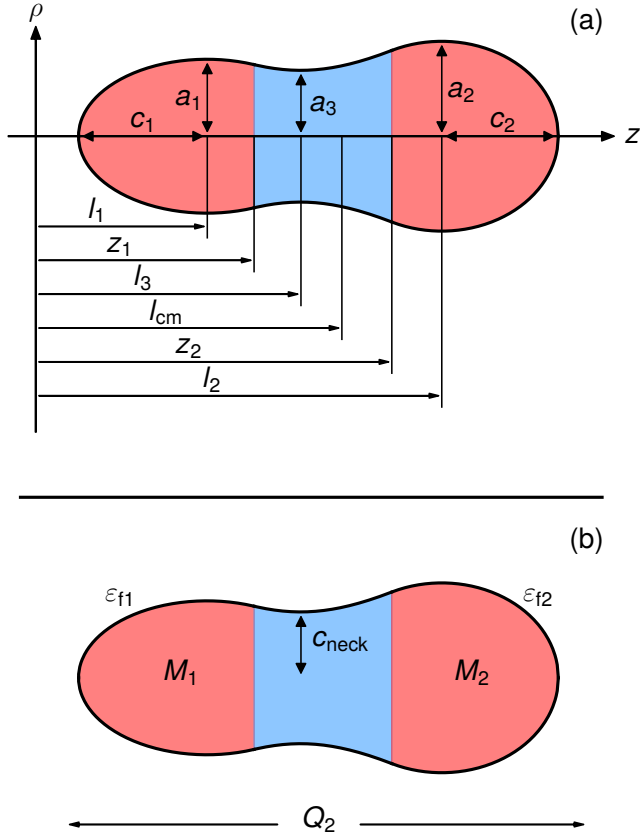


Figure 2.1: Shape described by three smoothly joined portions of quadratic surfaces of revolution. (a) Each surface is specified by the position l_i of its center, its transverse semi-axis a , and its semi-symmetry axis c . The middle hyperboloid of revolution joins smoothly with the two end spheroids at z_1 and z_2 . The location l_{cm} of the center of mass of the drop is also shown. (b) Parametrization in terms of five independent shape coordinates: charge quadrupole moment Q_2 ; neck c_{neck} ; nascent-fragment deformations ε_{f1} , ε_{f2} ; and mass asymmetry $\alpha = (M_1 - M_2)/(M_1 + M_2)$, where M_1 and M_2 are the volumes inside the end-body quadratic surfaces, were they completed to form closed-surface spheroids.

The shapes in 3QS coordinates can be defined in five more familiar shape coordinates (see Fig. 2.1(b)): (1) elongation coordinate expressed in terms of the quadrupole moment Q_2 of the nuclear charge distribution. The dimensionless elongation parameter q_2 is defined as

$$q_2 = \frac{4\pi Q_2}{3ZR_A^2}, \quad (2.6)$$

where R_A is the nuclear radius; (2) neck radius c_{neck} ; (3) left nascent-fragment deformation ε_{f1} ; (4) right nascent-fragment deformation ε_{f2} ; and (5) mass asym-

metry $\alpha = (M_1 - M_2)/(M_1 + M_2)$, where M_1 and M_2 are the volumes inside the end-body quadratic surfaces, were they completed to form closed-surface spheroids. The five shape coordinates are denoted as $\chi = (q_2, c_{\text{neck}}, \varepsilon_{\text{fl}}, \varepsilon_{\text{f2}}, \alpha)$.

2.2 Macroscopic models

The macroscopic part of the energy, E_{mac} , can be obtained from the LDM or refinements such as the finite-range droplet model (FRDM) or the finite-range liquid-drop model (FRLDM) [25–27].

2.2.1 Liquid-drop model

The LDM has its origin in the semi-empirical mass model, usually attributed to von Weizsäcker [28] and Bethe and Bacher [29]. This model relies on the analogy with an incompressible liquid drop and the formula for the nuclear binding energy includes five contributions:

1. *Volume term:* The nuclear forces show saturation, which means that an individual nucleon interacts only with its nearest neighbours. This gives a binding-energy term that is proportional to the number of nucleons, i.e. a volume term (since the nuclear radius is proportional to $A^{1/3}$).
2. *Surface term:* The nucleons on the surface are less tightly bound than those in the interior because they have no neighbours outside the surface. This decrease in binding energy gives a negative energy term proportional to the surface area $4\pi R^2 = 4\pi A^{2/3}$.
3. *Coulomb term:* The Z protons in the nucleus repel each other due to the Coulomb force, which is proportional to Z^2 and inversely proportional to the radius $R \propto A^{1/3}$. This energy term is negative because the nucleons are less tightly bound than they would be without the repulsion.
4. *Asymmetry term:* Due to the Pauli principle it is more favourable to have an approximately equal number of protons and neutrons. A negative energy term corresponding to the difference $|N - Z|$ is therefore needed. The best agreement with observed binding energies is obtained if this term is proportional to $(N - Z)^2/A$.
5. *Pairing term:* Nuclei with an even number of nucleons are systematically more bound than those with an odd one. This gives rise to a pairing term

E_{oe} , where $E_{\text{oe}} = \Delta$ for even-even nuclei, $E_{\text{oe}} = 0$ for odd-mass nuclei and $E_{\text{oe}} = -\Delta$ for odd-odd nuclei.

The total nuclear binding energy E_{B} is then given by

$$E_{\text{B}} = a_{\text{V}}A - a_{\text{S}}A^{2/3} - a_{\text{C}}\frac{Z^2}{A^{1/3}} - a_{\text{A}}\frac{(N-Z)^2}{A} + E_{\text{oe}}, \quad (2.7)$$

called the semi-empirical binding formula. The constants are chosen to make this formula best fit the observed binding energies of nuclei.

Soon after fission was discovered, Bohr and Wheeler [30] suggested a generalization of the semi-empirical mass model to describe the shape changes in the division of the nucleus. Only the Coulomb and surface energies were assumed to depend on deformation, so that

$$E_{\text{B}} = a_{\text{V}}A - a_{\text{S}}A^{2/3}B_{\text{S}}(\alpha) - a_{\text{C}}\frac{Z^2}{A^{1/3}}B_{\text{C}}(\alpha) - a_{\text{A}}\frac{(N-Z)^2}{A} + E_{\text{oe}}, \quad (2.8)$$

where $B_{\text{S}}(\alpha)$ and $B_{\text{C}}(\alpha)$ are the ratios of the surface and Coulomb energies at deformation α to that for spherical shape.

It has also been argued that the surface term should be isospin-dependent, so that the surface term is written as $-a_{\text{S}}(1 - \kappa_{\text{S}}I^2)A^{2/3}B_{\text{S}}(\alpha)$, where $I = (N - Z)/A$ is the relative neutron excess. The macroscopic energy is then with Eq. (2.1) given by

$$\begin{aligned} E_{\text{mac}} &= ZM_{\text{H}} + NM_{\text{n}} && \begin{pmatrix} \text{(masses of } Z \text{ hydrogen} \\ \text{atoms and } N \text{ neutrons)} \end{pmatrix} \\ &- a_{\text{V}}(1 - \kappa_{\text{V}}I^2)A && \text{(volume and volume-asymmetry energies)} \\ &+ a_{\text{S}}(1 - \kappa_{\text{S}}I^2)A^{2/3}B_{\text{S}}(\alpha) && \text{(surface and surface-asymmetry energy)} \\ &+ a_{\text{C}}\frac{Z^2}{A^{1/3}}B_{\text{C}}(\alpha) && \text{(Coulomb energy)} \\ &- E_{\text{oe}} && \text{(pairing energy),} \end{aligned} \quad (2.9)$$

where $\kappa_{\text{V}} = a_{\text{A}}/a_{\text{V}}$.

2.2.2 Finite-range liquid-drop model

The surface-energy term in the LDM accounts for the fact that nucleons at the surface have fewer neighbours than the nucleons at the center. However, the

nuclear force has a range of about 1 fm. Thus, the surface-energy term in the LDM is inadequate for systems with strong variations in the nuclear surface. The typical example is fission where the nucleus develops a small neck before it splits. The surface nucleons in the neck region then obtain some binding due to their interaction with the nucleons on the other side of the neck.

The effect of the finite range of the nuclear force on the surface energy is one of the additional effects taken into account in the FRLDM [27], which has provided reliable predictions of a large number of nuclear-structure properties for all nuclei between the proton and neutron drip lines. Figure 2.2 shows the difference between experimental masses from the AME2012 evaluation [31] and masses calculated in the FRLDM (with microscopic corrections included) for nuclei in their ground-state shapes. The resulting error is $\sigma_{\text{th}} = 0.6764$ MeV. Although the preferred model of ground-state masses is the FRDM [27], with an error of $\sigma_{\text{th}} = 0.5728$ MeV, the FRLDM is more suitable for the very deformed shapes occurring in fission.

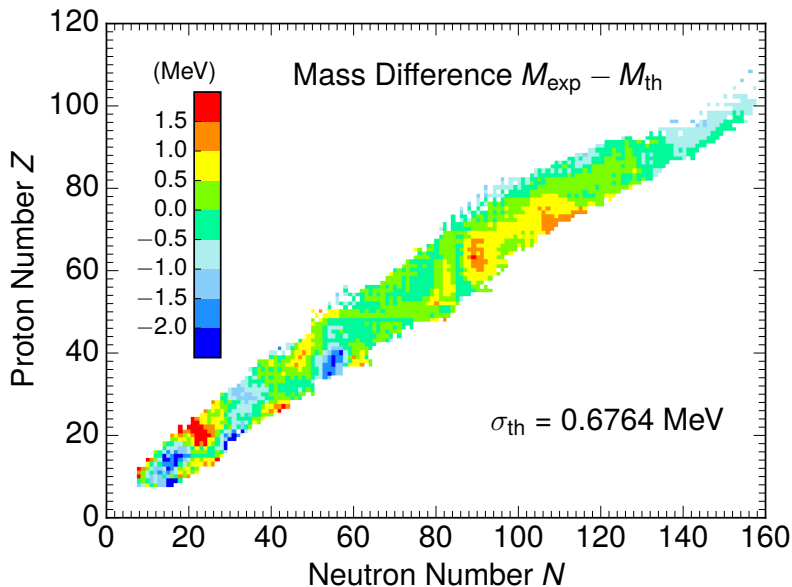


Figure 2.2: Difference between experimental masses from the AME2012 evaluation [31] and masses calculated in the FRLDM [27] for ground-state shapes, with an error $\sigma_{\text{th}} = 0.6764$ MeV.

The macroscopic energy in the FRLDM is expressed as

$$\begin{aligned}
E_{\text{mac}} = & ZM_{\text{H}} + NM_{\text{n}} && \left(\begin{array}{l} \text{masses of } Z \text{ hydrogen} \\ \text{atoms and } N \text{ neutrons} \end{array} \right) \\
& - a_{\text{V}} (1 - \kappa_{\text{V}} I^2) A && \text{(volume and volume-asymmetry energies)} \\
& + a_{\text{S}} (1 - \kappa_{\text{S}} I^2) B_1 A^{2/3} && \text{(surface energy)} \\
& + a_{\text{C}} \frac{Z^2}{A^{1/3}} B_3 && \text{(Coulomb energy)} \\
& - E_{\text{oe}} && \text{(average pairing energy)} \\
& + a_0 A^0 && (A^0 \text{ energy)} \\
& - c_4 \frac{Z^{4/3}}{A^{1/3}} && \text{(Coulomb exchange correction)} \\
& + f(k_{\text{F}} r_{\text{p}}) \frac{Z^2}{A} && \left(\begin{array}{l} \text{proton form-factor correction} \\ \text{to the Coulomb energy} \end{array} \right) \\
& - c_a (N - Z) && \text{(charge-asymmetry energy)} \\
& + E_{\text{W}} && \text{(Wigner energy)} \\
& - a_{\text{el}} Z^{2.39} && \text{(energy of bound electrons)}
\end{aligned} \tag{2.10}$$

The quantity B_1 is a generalization of the surface area of the nucleus at the actual shape to the surface area of the nucleus at the spherical shape, which also accounts for the effect of the finite range of the nuclear force. B_3 is the relative Coulomb energy. The pairing term E_{oe} in this expression contains separate average pairing gaps for protons and neutrons, $\overline{\Delta}_{\text{n}}$ and $\overline{\Delta}_{\text{p}}$, and an average neutron-proton interaction energy δ_{np} . For further details of the additional terms see Ref. [27].

2.3 Microscopic corrections

Strutinsky observed that the deviation of the binding energy from the macroscopic LDM prediction was large for nuclei with a smaller than average single-particle level density above the Fermi surface. He therefore proposed a method [32, 33] in which these shell effects are considered as small deviations from a uniform single-particle level spectrum. This deviation is then added as a correction to the macroscopic energy. The effect of pairing can also be treated as a correction in a similar way and the total microscopic correction is then given

by the sum of both corrections,

$$E_{\text{mic}} = E_{\text{sh}} + E_{\text{pc}}. \quad (2.11)$$

Both terms are calculated separately for protons and neutrons and then summed, i.e.

$$E_{\text{sh}} = E_{\text{sh}}^{\text{neut}} + E_{\text{sh}}^{\text{prot}}, \quad E_{\text{pc}} = E_{\text{pc}}^{\text{neut}} + E_{\text{pc}}^{\text{prot}}. \quad (2.12)$$

2.3.1 Folded-Yukawa single-particle potential

The Strutinsky method employs the single-particle energies from a phenomenological mean-field potential. The single-particle potential felt by a nucleon is given by

$$V = V_1 + V_{\text{s.o.}} + V_{\text{C}}, \quad (2.13)$$

where V_1 is the spin-independent nuclear part of the potential, $V_{\text{s.o.}}$ is the spin-orbit potential, and V_{C} is the Coulomb potential for protons. In the FRLDM the V_1 term is calculated in terms of the folded-Yukawa potential

$$V_1(\mathbf{r}) = -\frac{V_0}{4\pi a_{\text{pot}}^3} \int_V \frac{e^{-|\mathbf{r}-\mathbf{r}'|/a_{\text{pot}}}}{|\mathbf{r}-\mathbf{r}'|/a_{\text{pot}}} d^3r', \quad (2.14)$$

where the integration is over the volume of the shape, and where a_{pot} is the range of the Yukawa function.

2.3.2 Shell correction

The shell-correction energy E_{sh} is defined as the difference between the sum of the actual single-particle energies in the mean-field potential and the single-particle energies corresponding to a smearing of the actual single-particle energies. The expression for neutrons is (analogous expression hold for protons)

$$E_{\text{sh}}^{\text{neut}} = \sum_{i=1}^N e_i - \tilde{E}^{\text{neut}}, \quad (2.15)$$

where e_i are the calculated single-particle energies. The quantity \tilde{E}^{neut} is the smooth single-particle energy sum obtained by smearing the calculated energies e_i over an energy range γ using a Gaussian function modified with a polynomial of order p . The values of the two constants p and the range γ are chosen by requiring stability of the results.

2.3.3 Pairing correction

The pairing correction is defined in terms of a pairing correlation energy E_{pair} and an average pairing correlation energy \tilde{E}_{pair} . For neutrons it is given by (analogous expression hold for protons)

$$E_{\text{pc}}^{\text{neut}} = E_{\text{pair}}^{\text{neut}} - \tilde{E}_{\text{pair}}^{\text{neut}}. \quad (2.16)$$

The pairing corrections are the differences between the pairing energies calculated in the Lipkin-Nogami approximation [34–36] and the average pairing energies calculated as discussed in Ref. [37].

Chapter 3

Nuclear level densities

Nuclear excited energy levels display a discrete spectrum for low excitation energies. The nuclear level density is defined as the number of levels per unit energy at a certain excitation energy. In other words it is the number of different ways in which individual nucleons can be placed in the various single particle orbitals such that the excitation energy lies in the range E to $E+dE$. It increases rapidly with excitation energy.

3.1 Fermi-gas level density

The simplest type of model for calculations of level densities is the Fermi-gas (FG) model, which is derived for a uniform single particle spectra. For an excitation energy E^* this results in a level density $\rho_{\text{FG}}(E^*) \sim e^{2\sqrt{aE^*}}$ [38]. The level-density parameter a is given by $a = \pi^2/(6g_0)$, where g_0 is the density of single-particle states [39].

For a deformed nucleus with shape χ the formula becomes [40]

$$\rho_{\text{FG}}(E^*(\chi), I) = \frac{2I+1}{48} \left(\frac{\hbar^2}{2\mathcal{J}} \right)^{1/2} (E_{\text{intr}})^{-3/2} \exp\left(2\sqrt{aE_{\text{intr}}}\right), \quad (3.1)$$

where

$$E_{\text{intr}} = E^*(\chi) - I(I+1)\hbar^2/2\mathcal{J}(\chi), \quad (3.2)$$

is the intrinsic energy of a state with angular momentum I and moment of inertia $\mathcal{J}(\chi)$.

3.1.1 Back-shifted Fermi-gas level density

Actual single particle spectra display irregular structures due to microscopic effects. These effects can approximately be taken into account by introducing a back-shift in the energy. The relevant FG level density is then given by

$$\rho_{\text{BFG}}(E^*(\chi), I) = \frac{2I + 1}{48} \left(\frac{\hbar^2}{2\mathcal{J}} \right)^{1/2} (\tilde{E}_{\text{intr}})^{-3/2} \exp \left(2\sqrt{a\tilde{E}_{\text{intr}}} \right), \quad (3.3)$$

where \tilde{E}_{intr} is a back-shifted excitation energy. Ignatyuk has suggested the following expression for the back-shifted excitation energy [41]

$$\tilde{E}_{\text{intr}} = E_{\text{intr}} + \left(1 - e^{-E_{\text{intr}}(\chi)/E_{\text{d,sh}}} \right) E_{\text{sh}} + \left(1 - e^{-E_{\text{intr}}(\chi)/E_{\text{d,pc}}} \right) E_{\text{pc}}, \quad (3.4)$$

where $E_{\text{d,sh}}$ and $E_{\text{d,pc}}$ are the damping interval for the shell energy E_{sh} and the pairing energy E_{pc} , respectively.

3.1.2 Effective level density

Similarly to the back-shifted energy in Eq. (3.3), an ‘‘effective’’ level density was introduced in Ref. [42] to take account of the gradual decrease in microscopic effects as the nuclear excitation energy is raised. For a nucleus with shape χ and excitation energy $E^*(\chi)$, an effective excitation energy $E_{\text{eff}}^*(\chi)$ is defined as

$$E_{\text{eff}}^*(\chi) = E^*(\chi) + [1 - \mathcal{S}(E^*(\chi))] E_{\text{mic}}(\chi), \quad (3.5)$$

where $E_{\text{mic}}(\chi)$ is the microscopic part of the potential energy. The suppression function \mathcal{S} is required to be equal to one at excitation energy zero, and should converge to zero for large $E^*(\chi)$. The function employed reads

$$\mathcal{S}(E^*(\chi)) = \frac{1 + e^{-E_1/E_0}}{1 + e^{(E^*(\chi) - E_1)/E_0}}, \quad (3.6)$$

with parameters $E_0 = 15$ MeV and $E_1 = 20$ MeV. The effective level density is obtained by inserting the effective excitation energy into the simple FG expression,

$$\rho_{\text{eff}}(E^*) \sim \exp \left(2\sqrt{aE_{\text{eff}}^*} \right), \quad (3.7)$$

with level-density parameter $a = A/(8 \text{ MeV})$.

3.2 Combinatorial level density method

A method was developed in Ref. [40] for microscopic calculations of level densities in deformed nuclei. For a specified shape χ , the single-particle levels for protons and neutrons are obtained by solving the Schrödinger equation in the associated folded-Yukawa potential (see Sec. 2.3.1). For each many-body state, blocked BCS calculations for neutrons and protons separately provide the energies of the intrinsic many-body states $E_i^n(\chi)$ and $E_i^p(\chi)$.

All shapes considered have axial symmetry. Rotation is treated by considering the diagonal contribution from the collective rotation in the particles+rotor model. This gives the rotational contribution E_i^{rot} to the energy,

$$E_i^{\text{rot}}(I, \chi) = \frac{(I(I+1) - K_i(\chi)^2)}{2\mathcal{J}_i(\chi)}, \quad (3.8)$$

where $\mathcal{J}_i(\chi)$ is the pairing and shape-dependent moment of inertia [43].

The total energy of a state is then given by

$$E_i(I, \chi) = E_i^n(\chi) + E_i^p(\chi) + E_i^{\text{rot}}(I, \chi). \quad (3.9)$$

The level density for a fixed angular momentum I is obtained by counting the states $E_i(I, \chi)$ in a bin of width ΔE centered around E_b ,

$$\rho(E_b, I) = \frac{1}{\Delta E} \int_{E_b - \Delta E/2}^{E_b + \Delta E/2} \sum_i \delta(E - E_i(I, \chi)) dE. \quad (3.10)$$

The bin width is in the present studies taken as $\Delta E = 200$ keV.

3.2.1 Extrapolation to high excitation energies

Since it is too time consuming to calculate level densities at all required excitation energies, an approximation is performed. The calculated combinatorial level density is employed up to an excitation energy $E^* \approx 6$ MeV and then smoothly continued upwards by an analytical expression. The following formula was used in Ref. [23],

$$\rho(E^*(\chi), I) = C(\chi) \tilde{E}_{\text{intr}}^{-3/2} \exp\left(2\sqrt{a\tilde{E}_{\text{intr}}}\right), \quad (3.11)$$

where \tilde{E}_{intr} is the back-shifted intrinsic excitation energy in Eq. (3.4), and where the level-density parameter is expressed as $a = A/e_0$. The constant $C(\chi)$

was determined by continuity with the corresponding microscopic value at the matching energy $E^*(\chi) = 5.9$ MeV. The three parameters e_0 , $E_{d,sh}$, $E_{d,pc}$ were determined by a nonlinear least-squares fit of the logarithm of the extrapolated values to the corresponding microscopically calculated level densities for ^{236}U .

For high excitation energies, the level densities should however approach the FG expression in Eq. (3.3). In order to obtain the correct asymptotic behavior of the level densities the extrapolation was therefore slightly modified to the following expression

$$\begin{aligned} \rho(E^*(\chi), I) &= \\ &= \left(1 + C(\chi)e^{-E^*(\chi)/E_{d,sh}}\right) \frac{2I+1}{48} \left(\frac{\hbar^2}{2\mathcal{J}}\right)^{1/2} \tilde{E}_{\text{intr}}^{-3/2} \exp\left(2\sqrt{a\tilde{E}_{\text{intr}}}\right), \end{aligned} \quad (3.12)$$

where the asymptotic value is approached at the same rate as the damping of the shell effects.

Part II

Fission and fusion

Chapter 4

Potential-energy surfaces

As already recognized shortly after its discovery, the fission process can be described as an evolution of the nuclear shape from a roughly spherical shape into two separate fragments. One therefore has to calculate the potential energy for the various shapes the nucleus can undertake on its way to fission.

There are two ways to construct these potential-energy surfaces. One method is to solve a self-consistent mean-field problem with appropriate constraints on the nuclear shape (see e.g. Ref. [44]). The other method, which is the one followed here, is to first define a class of shapes that are supposed to contain the relevant shapes and then employ the macroscopic-microscopic method to calculate the potential energy of those shapes.

4.1 Liquid-drop model

The most basic features of fission can be understood by considering only the macroscopic part of the energy as in Sec. 2.2.1. Since only the Coulomb term and the surface term depend on the deformation, the total deformation-dependent energy is then simply the sum of these two terms,

$$E(\alpha_2) = E_S(\alpha_2) + E_C(\alpha_2), \quad (4.1)$$

where the deformation parameter α_2 characterizes the elongation of the fissioning nucleus. The deformation-dependence of the Coulomb energy and the surface energy is shown in Fig. 4.1(a) for nucleus ^{236}U . The surface area is minimal for a sphere, while deformed shapes have larger surfaces. Therefore, the

surface energy increases with deformation. The Coulomb energy is on the other hand minimal when the nucleons are far apart and maximal for spherical shapes. Therefore, the Coulomb energy decreases with deformation. The counteracting effects of the two terms give rise to a fission barrier in the potential energy as a function of the elongation shape parameter (Fig. 4.1(b)). (Note the difference in scale in the two figures.) The fission barrier which the nucleus has to overcome in order to fission, has a maximum which is referred to as the saddle point. Beyond the saddle, the repulsive Coulomb force between the nascent fragments overtake the surface tension.

The fissioning nucleus usually start with a small deformation (close to spherical). In order to fission, the nucleus then has to pass the barrier. This can occur either spontaneously, where the nucleus tunnels through the barrier, or through induced fission where the nucleus gain energy from an inducing particle so that it can overcome the barrier. The point when the nucleus splits into two fragments is called the scission point.

The surface energy and the Coulomb energy also have different dependencies on

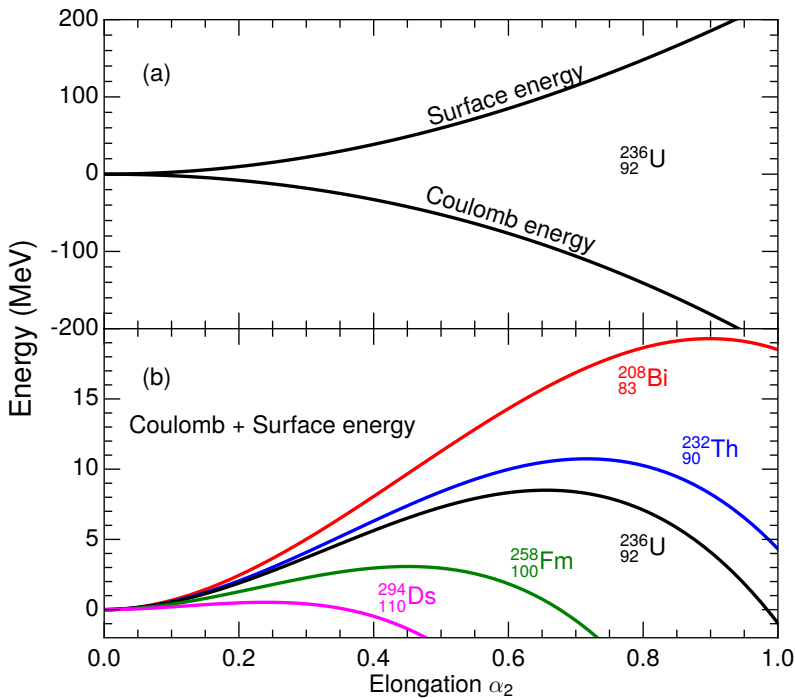


Figure 4.1: Surface energy and Coulomb energy in the LDM for nucleus $^{236}_{92}\text{U}$ (a) and the sum of the both terms for different nuclei (b) as a function of elongation coordinate α_2 .

the number of nucleons, which means that the fission barrier is different for each nucleus as shown in Fig. 4.1(b). The fission barrier is rather large for light nuclei, which are therefore very stable against fission. As one moves to heavier nuclei the fission barrier becomes ever smaller in both height and width. Accordingly, it will require correspondingly less excitation for the nucleus to overcome the barrier, as well as tunnel through the barrier, and undergo fission. Ultimately, for sufficiently heavy nuclei, the stability against deformation is lost altogether.

4.2 Finite-range liquid-drop model

Despite the success of the LDM, it has clear limitations to explain experimental observations, in particular the asymmetric mass-division seen in certain nuclei. The smooth macroscopic deformation energy in the LDM is modified as a result of the shell effects, leading to more complicated structures in the barriers. It can in particular lead to a double-humped barrier with a secondary minimum in which a long-lived shape isomeric state may be hosted. Microscopic effects, in particular those that lower the ground-state energy, can also increase the barrier for superheavy nuclei, thus giving rise to the possibility for those nuclei be more stable against fission. It was furthermore proposed that certain experimental

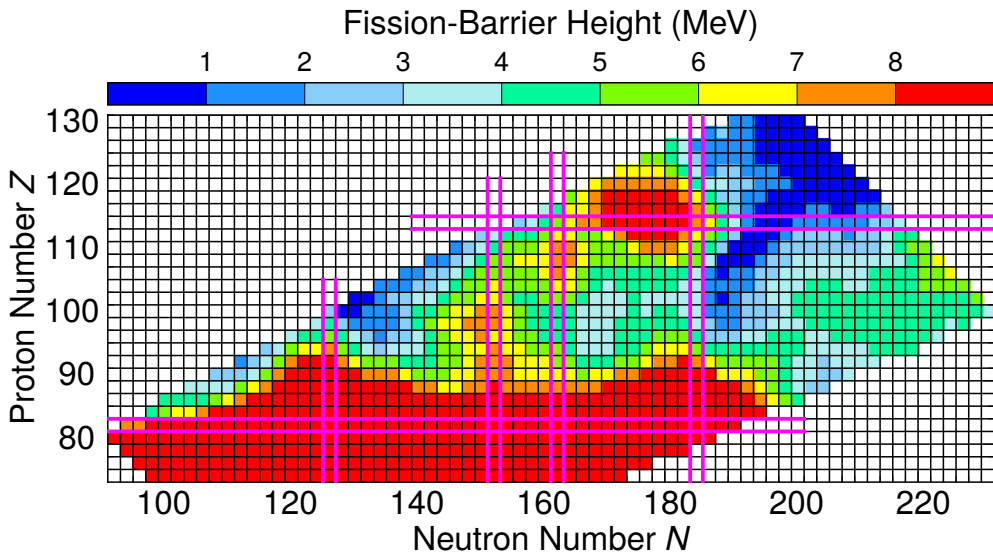


Figure 4.2: Fission-barrier heights versus proton and neutron number calculated within the FRLDM. Pairs of magenta parallel lines indicate magic neutron and proton numbers in the model ($N = 126, 184$ and $Z = 82, 114$). See Ref. [45] for further details.

data could best be explained if the barrier exhibited a triple-humped structure [46]. In the early studies of fission, the potential energy was usually calculated only for a few hundred nuclear shapes. Several million shapes are however needed to fully account for all possible fission paths.

In the present studies, the potential energy $U(\chi)$ is calculated within the FRLDM in a grid of more than 6 million shapes given in the 3QS parametrization, as described in Ch. 2. Several potential-energy studies within the FRLDM can be found in Refs. [45, 47–52]. The five-dimensional potential-energy landscape of a nucleus can be analyzed with the immersion techniques described in Ref. [50] in order to identify various saddle points. Figure 4.2 shows calculated fission-barrier heights for even-even nuclei in the FRLDM [45]. Higher barrier heights are seen around ${}^{252}_{100}\text{Fm}_{152}$, ${}^{270}_{108}\text{Hs}_{162}$, and ${}^{298}_{114}\text{Fl}_{184}$ due mostly to strong ground-state shell effects.

4.2.1 Fission modes

In order to explain the observation that fission could occur both in a symmetric and an asymmetric way, Turkevich and Niday [53] proposed in 1951 two different channels through which fission occurs. These are referred to as fission modes and differ both in mass and kinetic energy of the resulting fragments.

Additional fission modes were further introduced by Brosa [54] where values of the total kinetic energy (TKE) of the fragments are associated with different shapes at scission. The asymmetric mode is denoted the standard (St) mode since it is the dominating mode in low-energy fission of actinides (see Sec. 6.1). The St mode is further split into two modes called Standard 1 (St1) and Standard 2 (St2). They are ascribed to two different shell effects in the heavy fragment; the St1 mode is attributed to the doubly magic nucleus ${}^{132}\text{Sn}$, while the St2 mode is attributed to the deformed magic neutron number $N = 88$ [55]. The symmetric mode is called superlong (SL) mode, where the name refers to a more elongated scission shape and thus lower TKE.

For fission of nuclei around ${}^{258}\text{Fm}$ it was observed that it mainly split symmetrically with a very high TKE. This was argued to arise due to both fragments being close to doubly magic nucleus ${}^{132}\text{Sn}$, resulting in a very compact scission shape and thus a high TKE value [56]. This type of fission is therefore said to occur in a super-short (SS) fission mode.

In the calculations presented here it is also obtained that nuclei in the super-heavy region, $106 \leq Z \leq 114$ and $162 \leq N \leq 176$ fission in a very asym-

Standard (St)	Super-long (SL)	Super-short (SS)	Super- asymmetric (SA)
			
$A_H \approx 140$ $q_2 \approx 11$ $\varepsilon_H \approx -0.1$ $\varepsilon_L \approx 0.3$	$A_H \approx A_L$ $q_2 \approx 17$ $\varepsilon_H \approx 0.3$ $\varepsilon_L \approx 0.3$	$A_H \approx A_L$ $q_2 \approx 8$ $\varepsilon_H \approx 0.0$ $\varepsilon_L \approx 0.0$	$A_H \approx 208$ $q_2 \approx 8$ $\varepsilon_H \approx -0.1$ $\varepsilon_L \approx 0.3$

Figure 4.3: Typical shapes at scission of fission modes identified in the calculations. Also given are typical scission values of the elongation q_2 of the fissioning nucleus and deformations $\varepsilon_{L/H}$ and mass numbers $A_{L/H}$ of the fragments.

metric way, where the heavy fragment is found to be close to ^{208}Pb with a corresponding light fragment (see Sec. 6.1). This type of fission is denoted as a super-asymmetric (SA) mode¹.

Figure 4.3 shows typical shapes at scission for the fission modes identified in the calculations (see Ch. 6). Typical values are also given for the elongation q_2 of the fissioning nucleus and deformations $\varepsilon_{L/H}$ and mass numbers $A_{L/H}$ of the fragments. In the calculations we do not distinguish between the St1 and St2 modes.

The different modes generally follow different paths after the first saddle of the potential-energy surface. Beyond the fission isomer, different “fission valleys” can be determined in the calculated potential-energy surface [50]. This is done by determining, for each value of elongation coordinate q_2 , minima in the corresponding restricted space in the four other shape coordinates. Valleys are then defined as a sequence of similar minima that persist for successive q_2 values where the shape coordinates change gradually between neighbouring q_2 values.

¹The term “super-asymmetric mode” is also used by Brosa but in fission of ^{252}Cf where the heavy-fragment mass number is 161 [54].

Figure 4.4 shows two fission valleys for the nucleus ^{236}U as a function of elongation q_2 . The asymmetric valley (red curve) and the symmetric valley (green curve) exhibit similar values for the fragment masses and deformations to that of the St mode and the SL mode, respectively. The two valleys are separated by a ridge (black curve with triangles). The ground state is located at $q_2 \approx 0.7$ (not shown) with energy E_{gs} (horizontal dot-dashed line). The asymmetric St path exhibit a steep slope beginning around $q_2 \approx 9$, where the neck rapidly decreases. Scission in the St mode then typically occurs slightly further out in elongation at $q_2 \approx 11$. The symmetric SL path continues further out in q_2 until the neck starts to shrink; fission along this path therefore occur at a larger elongation around $q_2 \approx 17$.

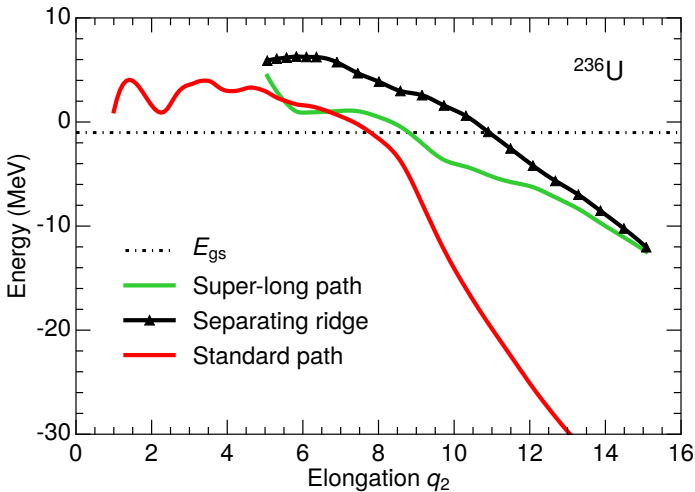


Figure 4.4: The potential energy along the fission paths for the St mode (solid red) and the SL mode (solid green), shown as function of the elongation q_2 for ^{236}U . The ridge separating the two paths is shown by the black curve with triangles. The ground state is located at $q_2 \approx 0.7$ (not shown) with energy E_{gs} (horizontal dot-dashed line).

Figure 4.5 shows fission valleys for even $^{256-262}\text{Fm}$ as a function of elongation q_2 . The thin black line shows the first saddle connecting the ground state (not shown) and the 2nd minimum. The symmetric SS path (blue curves) and the asymmetric St path (red curves) exhibit similar fragment masses and deformations as the SS mode and the St mode, respectively. The St valley is observed in all four isotopes, while the SS valley is fully developed first in ^{258}Fm and heavier

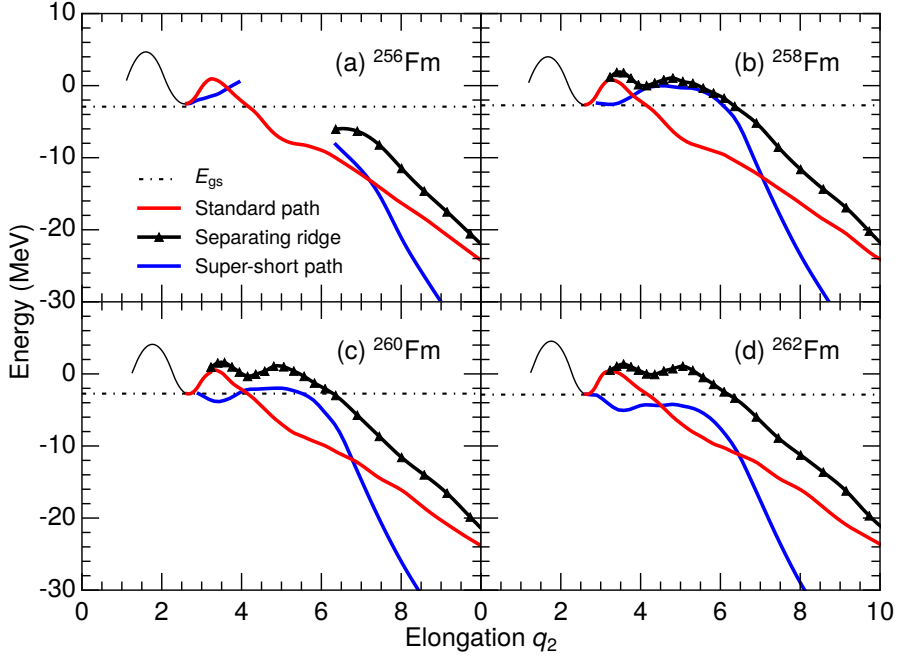


Figure 4.5: The potential energy along the fission paths for the St mode (solid red) and the SS mode (solid blue), shown as function of the elongation q_2 for (a) ^{256}Fm , (b) ^{258}Fm , (c) ^{260}Fm and (d) ^{262}Fm . The ridge separating the two paths is shown by the black curve with triangles. The ground-state energy is shown by the horizontal dot-dashed line. The ground-state minimum ($q_2 \approx 0.75$) is separated by the first barrier (black thin line) from the isomeric minimum ($q_2 \approx 2.5$).

isotopes. The potential energy in the SS valley dramatically decreases already at $q_2 \approx 6$ with an associated shrinking of the neck radius. This valley therefore leads to a very compact scission shape. The SS valley in ^{258}Fm is rather fragile since the ridge to the St valley is less than 1 MeV at $q_2 \approx 4$. The depth of the SS valley gradually increases when approaching ^{264}Fm , which corresponds to a split with exactly two doubly-magic ^{132}Sn .

^{274}Hs

Figure 4.6 shows fission valleys for ^{274}Hs as a function of q_2 ; the very asymmetric SA valley (orange curve) and a symmetric valley (dashed black curve). The SA valley corresponds to a spherical heavy fragment near ^{208}Pb and a prolate deformed light fragment. The neck has almost vanished for $q_2 \gtrsim 6$ and the valley approximately corresponds to a pure Coulomb interaction between the two fragments. This valley is similar to the “fusion valleys” discussed for neighbouring nuclei in Ref. [57] and in Ch. 9.

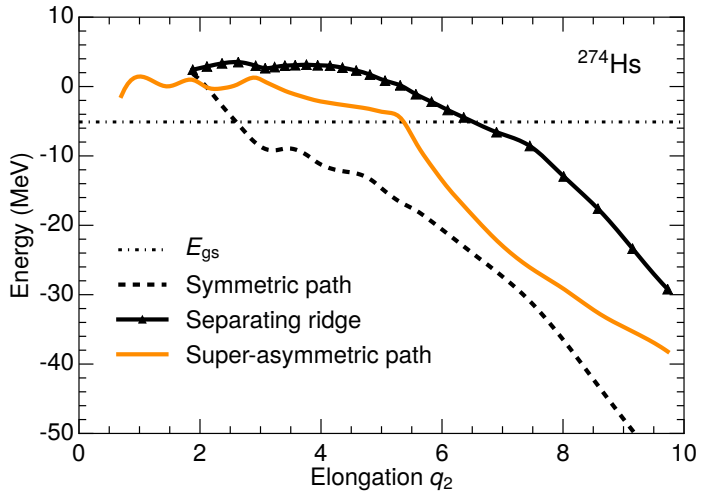


Figure 4.6: The potential energy along the fission paths for the SA mode (solid orange) and the symmetric path (dashed black), shown as function of the elongation q_2 for ^{274}Hs . The ridge separating the two paths is shown by the black curve with triangles. The ground state is located at $q_2 \approx 0.5$ (not shown) with energy E_{gs} (horizontal dot-dashed line).

Chapter 5

Fission dynamics

Although many attributes of the fission process can be understood by studying the potential-energy landscape of the fissioning nucleus, nuclear fission is the result of a complicated dynamical evolution of a small many-body system. Much progress has been made within microscopic self-consistent approaches, though such calculations are computationally rather heavy (see e.g. Ref. [44] for a review).

The Metropolis random-walk approach employed in the present studies offers an efficient method to simulate the fission process, avoiding the complications of dealing with the time-dependence explicitly. It is based on the classical Langevin formalism, which is a stochastic differential equation describing the time evolution of the macroscopic degrees of freedom of a system. It is suitable when the time scale of the macroscopic degrees of freedom is much larger than the microscopic degrees of freedom.

5.1 Stochastic dynamics formalism

5.1.1 The Langevin equation

The Langevin description of fission is based on the assumption that the system exhibits two different time scales; one being associated with the slow motion of the collective shape degrees of freedom and the other with the rapid motion of the intrinsic degrees of freedom. Let the N -dimensional variable $\chi = \{\chi_i\}$ specify a particular nuclear shape ($N = 5$ in the present studies). We then

want to determine how $\boldsymbol{\chi}$ evolves from a near-spherical shape of the fissioning nucleus towards two separated fragments. The local gradient of the potential energy $U(\boldsymbol{\chi})$ provides a driving force, $\mathbf{F}(\boldsymbol{\chi}) = -\partial U(\boldsymbol{\chi})/\partial \boldsymbol{\chi}$, that will seek to change the shape so that the potential energy is minimized. A shape change is also associated with a rearrangement of the nucleons inside the nucleus. The associated kinetic energy is assumed to be of normal form, $K = \frac{1}{2} \sum_{ij}^N M_{ij} \dot{\chi}_i \dot{\chi}_j$, where $M_{ij}(\boldsymbol{\chi})$ is the $N \times N$ inertial-mass tensor.

If there were no coupling between the shape variables $\boldsymbol{\chi}$ and the internal degrees of freedom, then the shape dynamics would be conservative. The time evolution of the collective shape then follows from the Lagrangian function,

$$\mathcal{L}(\boldsymbol{\chi}, \dot{\boldsymbol{\chi}}) = \frac{1}{2} \sum_{ij} M_{ij}(\boldsymbol{\chi}) \dot{\chi}_i \dot{\chi}_j - U(\boldsymbol{\chi}), \quad (5.1)$$

and the associated collective momentum is given by

$$p_i(\boldsymbol{\chi}, \dot{\boldsymbol{\chi}}) = \frac{\partial}{\partial \dot{\chi}_i} \mathcal{L}(\boldsymbol{\chi}, \dot{\boldsymbol{\chi}}). \quad (5.2)$$

However, the interaction between the macroscopic and the microscopic degrees of freedom causes the shape variables to experience a dissipative force characterized by the $N \times N$ dissipation tensor $\boldsymbol{\gamma}(\boldsymbol{\chi})$. It consists of a friction force $-\sum_j \gamma_{ij} \dot{\chi}_j(t)$ and a stochastic term $\xi_i(\boldsymbol{\chi}, \dot{\boldsymbol{\chi}}, t)$.

The equation of motion for the time evolution of the nuclear shape is then obtained by equating the rate of momentum change with the forces acting,

$$\dot{p}_i = -\frac{\partial}{\partial \chi_i} U(\boldsymbol{\chi}) + \frac{1}{2} \sum_{jk} \dot{\chi}_j \dot{\chi}_k \frac{\partial}{\partial \chi_i} M_{jk}(\boldsymbol{\chi}) - \sum_j \gamma_{ij} \dot{\chi}_j(t) + \xi_i(\boldsymbol{\chi}, \dot{\boldsymbol{\chi}}, t). \quad (5.3)$$

The calculation of the time evolution of the nuclear shape parameters $\boldsymbol{\chi}(t)$ then requires knowledge of three distinct quantities: $U(\boldsymbol{\chi})$, $\mathbf{M}(\boldsymbol{\chi})$ and $\boldsymbol{\gamma}(\boldsymbol{\chi})$. The Langevin equation in Eq. (5.3) can be solved directly by starting from the specified initial state and generating a large number of shape evolutions (see e.g. Refs. [58, 59]).

5.1.2 Collective inertia

The mass tensor M_{ij} describes the inertia of a nucleus with respect to changes of its deformation. A microscopic method for calculating the mass tensor is the Generator coordinate method [44].

For a fission path described by a parameter s , the collective inertia is given by

$$M(s) = \sum_{ij} M_{ij}(s) \frac{d\chi_i}{ds} \frac{d\chi_j}{ds}. \quad (5.4)$$

A common approximation of the mass tensor is to simply assume that the flow is incompressible and irrotational. A semi-empirical formula for the inertial mass in the elongation direction for calculating SF half-lives was derived in Ref. [60]

$$M(r) = \mu \left(1 + k \frac{17}{15} \exp \left[-a \left(r - \frac{3}{4} \right) \right] \right), \quad (5.5)$$

where r is the center-of-mass distance (in terms of the radius for the spherical nucleus $R_0 = 1.2A^{1/3}$) between the two halves. This expression decreases with increasing values of r and approaches the reduced mass $\mu = M_{f1} M_{f2} / (M_{f1} + M_{f2})$ appropriate to separated fragments at large distances. For small values of r , the inertia is expected to be higher than the hydrodynamical irrotational-flow result due to microscopic effects associated with single-particle level crossings. The asymptotic value at small r is then taken into account by relating the inertia $M(r)$ to the inertia M^{irr} corresponding to irrotational flow. The parameter k accounts for the increase of the inertia above the hydrodynamical value, while the constant a determines how fast the inertia approaches the asymptotic value.

Nuclei near ^{258}Fm that fission in the SS mode reach scission at a much smaller center-of-mass distance r than the nuclei considered for Eq. (5.5). Correspondingly, the reduced mass should be reached at a smaller r . A modified expression was therefore used in Ref. [61] to account for this effect

$$M(r) = \mu \left(1 + f(r, r_{\text{sc}}) k \frac{17}{15} \exp \left[-a \left(r - \frac{3}{4} \right) \right] \right), \quad (5.6)$$

where

$$f(r, r_{\text{sc}}) = \begin{cases} \left(\frac{r_{\text{sc}} - r}{r_{\text{sc}} - 0.75} \right)^2 & r \leq r_{\text{sc}}, \\ 0 & r \geq r_{\text{sc}}, \end{cases}$$

and where $r_{\text{sc}} = 1.59$ correspond to the center-of-mass distance for two touching spheres at scission.

The expressions for the inertial masses in Eqs. (5.5) and (5.6) are used in calculations of tunneling probabilities as described in Sec. 5.2.1, where the values $k = 16$ and $a = \frac{128}{51}$ are employed [61].

5.1.3 Brownian shape dynamics

Since the dissipation associated with the nuclear shape dynamics is relatively strong, the shape changes will be relatively slow. It might then be reasonable to ignore inertial forces altogether by putting the inertias to zero. This assumption of overdamped motion is supported by recent time-dependent density functional calculations of the whole fission process [62–64], while other calculations describe a fading away of the dissipation in the last stages of fission, when a thin neck develops towards scission [65]. The equation of motion is then reduced to

$$0 = -\partial U(\boldsymbol{\chi})/\partial \boldsymbol{\chi} - \boldsymbol{\gamma}(\boldsymbol{\chi}) \cdot \dot{\boldsymbol{\chi}} + \boldsymbol{\xi}(\dot{\boldsymbol{\chi}}, \boldsymbol{\chi}, t). \quad (5.7)$$

This is the Smoluchowski limit describing Brownian motion. It is however more complicated than the usual Brownian motion; it occurs in N dimensions, the medium is anisotropic ($\boldsymbol{\gamma}$ is not diagonal) and non-uniform ($\boldsymbol{\gamma}$ depends on $\boldsymbol{\chi}$), and the body is situated in an external potential, $U(\boldsymbol{\chi})$.

5.2 Metropolis walk method

Studies [66] suggest that the fission-fragment charge yield is rather insensitive to anisotropies in $\boldsymbol{\gamma}$, presumably because a large degree of equilibration takes place in the course of the strongly damped evolution. If one assumes that the dissipation tensor is isotropic, i.e. proportional to the unit tensor for any shape $\boldsymbol{\gamma}(\boldsymbol{\chi}) = \gamma(\boldsymbol{\chi})\mathbf{I}$, then the shape evolution can be simulated by a Metropolis walk on the potential energy lattice [22].

For a system with total energy E_{tot} , all of the local excitation energy $E^*(\boldsymbol{\chi}) = E_{\text{tot}} - U(\boldsymbol{\chi})$ is assumed to go to the intrinsic degrees of freedom described by the level density $\rho(E^*)$. The steps in the random walk are determined by the Metropolis algorithm. From the current shape i a neighbouring candidate shape j is selected at random. The probability $P_{i \rightarrow j}$ to accept a step is given by

$$P_{i \rightarrow j} = \min [1, \rho_j(E^*(\boldsymbol{\chi}_j))/\rho_i(E^*(\boldsymbol{\chi}_i))], \quad (5.8)$$

where $\rho_{i(j)}(E^*)$ is the level density for the shape $\boldsymbol{\chi}_{i(j)}$.

The Metropolis walks are performed on the five-dimensional potential-energy surfaces described in Sec. 4.2. The walks are usually started in the ground state or the isomer minimum. The asymmetry α is assumed to be frozen in when the neck radius has shrunk to $c_{\text{neck}} = 2.5$ fm [66]. Subsequently, the system reaches a scission configuration at $c_{\text{neck}} = c_{\text{sc}} = 1.5$ fm where the value of the

potential energy at this shape $U(\boldsymbol{\chi})$, the mass asymmetry coordinate α , the elongation q_2 , and the two fragment deformations ε_{f1} and ε_{f2} are registered. The choice of $c_{sc} = 1.5$ fm is discussed in Sec. 7.2. The proton and neutron numbers, Z and N , are determined by requiring the same Z/N ratio as for the fissioning nucleus. In the present studies, only fragments with even Z and N are considered. The random walks are then repeated to obtain the fission-fragment distributions. Typically 10^5 number of walks are performed to obtain convergence of the results.

The probabilities determining the steps in Eq. (5.8) are evaluated with the microscopic combinatorial level densities in Sec. 3.2 for $^{235}\text{U}(n, f)$, while other calculations are evaluated with the effective level densities in Sec. 3.1.2. (A comparison between the two methods can be found in Ref. [23].)

The random walk will usually tend to stay inside the fission barrier for many steps before eventually passing it. To speed up the calculations in studies of large number of nuclei, the potential energy is augmented by a bias term, $V_{\text{bias}} = V_0 Q_0^2 / Q_2^2$ [22], where Q_2 is the quadrupole moment of the fissioning nucleus and Q_0 is the average ground-state quadrupole moment of deformed actinide nuclei. For small Q_2 , V_{bias} will encourage increases of Q_2 , while it will have less effect for more deformed shapes closer to scission. The resulting yields are generally not sensitive to variations in the bias strength (an exception is the special case ^{258}Fm where there is a subtle competition between two fission modes). An alternative formulation of the Metropolis random-walk method was recently introduced in Ref. [67], which does not require a bias potential to speed up calculations.

5.2.1 Spontaneous-fission simulation

For spontaneous fission (SF) one finds forbidden regions of the elongation q_2 , where the total energy is below the potential energy. This problem of forbidden regions is approached in the studies by performing the Metropolis random walks with the addition of a small amount of energy ΔE , so that the walks may pass over the forbidden region. On the outer side of the forbidden region, this energy is given back, and the dynamics continues to scission. In this way, the random-walk algorithm effectively selects different shape configurations as starting points after the barrier in the SF simulation.

Most nuclei exhibit a single dominating mode for both SF and for low excitation energies. The fission paths are then similar in both cases. However, if there are two competing modes, as in ^{258}Fm , the fission path is very sensitive to small changes in energy (see Fig. 4.5(b)). A simple estimate of the tunneling

ratio comparing the two fission paths is obtained by performing one-dimensional WKB tunneling calculations from the isomeric minimum into the different valleys. The penetration probability P through the fission barrier is calculated within the WKB formalism [68] as

$$P = \frac{1}{1 + e^{S(L)}}, \quad (5.9)$$

where $S(L)$ denotes the action integral along the one-dimensional trajectory L ,

$$S(L) = \frac{2}{\hbar} \int_a^b \sqrt{2M(q_2)[U(q_2) - E_{\text{gs}}]} dq_2, \quad (5.10)$$

with a and b the entrance and exit point for the tunneling region. The quantities $U(q_2)$ and E_{gs} denote the potential energy and the ground-state energy, respectively. The inertial mass $M(q_2)$ for the St and SS paths are calculated with Eqs. (5.5) and (5.6), respectively, where it is expressed in terms of q_2 by a linear fit between r and q_2 . This yields that about 75% of the flux in ^{258}Fm tunnels to the SS valley and 25% to the St valley. The strong favouring of tunneling to the SS valley is due to the low mass parameter along this tunneling path.

Chapter 6

Scission quantities

6.1 Mass distributions

Figure 6.1 shows calculated mass yields for neutron-induced fission of ^{235}U for different incident-neutron energies E_n . For fission of actinides, such as uranium and plutonium, the yield distribution has two peaks showing that the split where one of the fragments is heavier is the most common, according to the St mode. When the energy of the incoming neutron is increased, these peaks decrease while the amount of symmetric yield increases. This is because the influence of the shell structure, associated with the asymmetric St mode, decreases with increasing excitation energy. The yield eventually acquires a Gaussian shape corresponding to a LDM behaviour.

The random-walk model was in Paper IV used to perform systematic yield calculations of 896 even-even nuclei between the drip lines from $Z = 74$ to $Z = 126$. Initial excitation energies E_0^* , with respect to the ground state of the fissioning nucleus (Z_0, N_0) , were chosen just sufficiently above the barrier to obtain reasonable computing times. Figure 6.2 shows the ratio between the calculated mass yield at symmetry and the maximum on the yield curve; red squares correspond to asymmetric yields while blue squares correspond to symmetric yields. Four regions of nuclei fissioning asymmetrically are identified: neutron-deficient ($74 \leq Z_0 \leq 86$, $92 \leq N_0 \leq 126$), actinide ($74 \leq Z_0 \leq 96$, $132 \leq N_0 \leq 186$), superheavy ($106 \leq Z_0 \leq 114$, $156 \leq N_0 \leq 178$) and neutron-rich ($82 \leq Z_0 \leq 110$, $188 \leq N_0 \leq 218$).

There are no experimental studies of the whole region shown in Fig. 6.2 but studies of 70 nuclei from $Z_0 = 85$ to $Z_0 = 94$ were presented in Ref. [74]. It

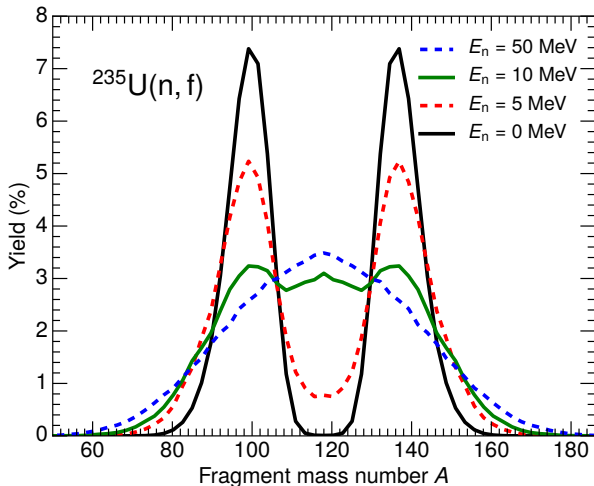


Figure 6.1: Calculated fission-fragment mass yields in $^{235}\text{U}(n, f)$ for incident-neutron energies $E_n = 0, 5, 10,$ and 50 MeV.

was suggested there that the transition between symmetric fission in the lighter actinide region and asymmetric for heavier actinides is at $A_0 \approx 226$. It is further stated that this is somewhat surprising since one would expect both protons and neutrons to affect what regions fission symmetrically or asymmetrically. However, in Ref. [74] fission mass distributions across the line $A_0 \approx 226$ are obtained for only a few proton numbers, namely $Z_0 = 89, 90$ and 91 . Here, and in Ref. [75], which covers a larger, contiguous region of nuclei than the experimental work, the results show that both protons and neutrons affect asymmetry. Particularly interesting is that above $Z_0 \approx 88$ ($N_0 \approx 132$) the calculated transition line is clearly not a constant mass number A_0 , but approximately a constant $N_0 - Z_0$ for a range of about eight proton numbers. This prediction has yet to be tested experimentally.

The result in Fig. 6.2 is illustrated in a complementary way in Fig. 6.3 where heavy and light fragment mass pairs are plotted as coloured symbols for nuclei that fission asymmetrically. Few experimental data exist in the neutron-deficient Pb-region, but asymmetric fission of $^{180}\text{Hg}_{100}$ was reported in Ref. [76]. Figure 6.3 shows that asymmetric fission of actinides with mass number from $A_0 \approx 220$ to $A_0 \approx 246$ correspond to divisions in the St mode with a heavy-fragment mass number that stays relatively constant around $A_H \approx 140$. Consequently, the light mass increases so the heavy/light fragment mass difference decreases as the fissioning system becomes heavier. This is also seen in measurements (see e.g. Fig. 4 in Ref. [70]).

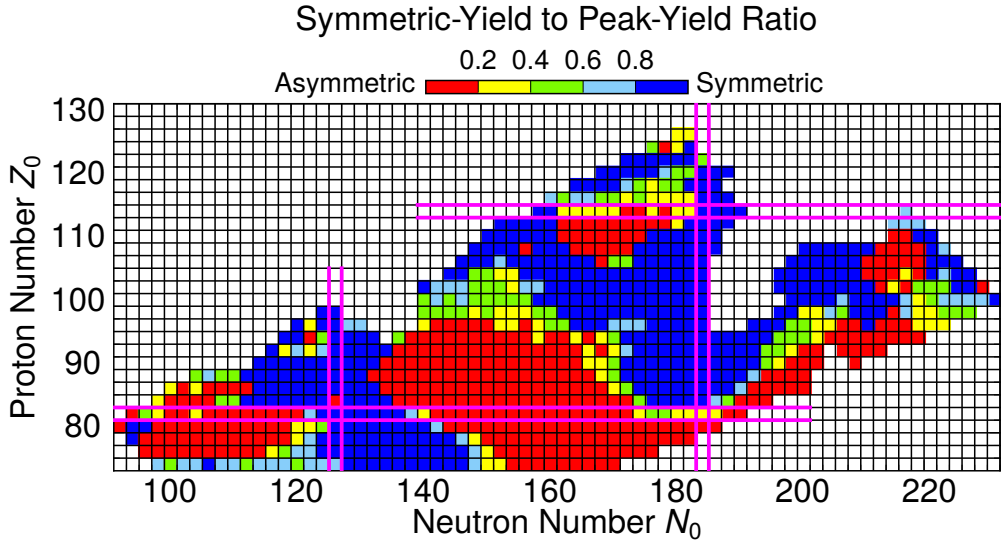


Figure 6.2: Calculated symmetric-yield to peak-yield ratios versus N_0 and Z_0 for fissioning nuclei between the proton and neutron drip lines and $74 \leq Z_0 \leq 126$, for even-even nuclei. Nuclei with barriers calculated to be lower than 3 MeV are not included (cf. Fig. 4.2). Pairs of magenta parallel lines indicate magic neutron and proton numbers in the model ($N = 126, 184$ and $Z = 82, 114$). The figure is taken from Paper IV.

Striking in Fig. 6.3 is the abrupt transition to a small region (corresponding to $Z_0 \approx 110, N_0 \approx 166$ in Fig. 6.2) of very large differences between the heavy and light fragment masses. This corresponds to the SA mode with a division into a ^{208}Pb -like heavy fragment and the corresponding partner. Mass yields of nuclei $^{274}_{108}\text{Hs}_{166}$, $^{278}_{112}\text{Cn}_{166}$, $^{284}_{110}\text{Ds}_{174}$ in this region are shown as solid lines in Fig. 6.4, where it is seen that the heavy-fragment peak stays constant, while the light-fragment peak changes depending on the mass of the fissioning nucleus. Secondary peaks are also observed around $A_L:A_H = 108:170$ for $^{278}_{112}\text{Cn}_{166}$. A ^{208}Pb -like fission fragment in the superheavy region is compatible with results based on density functional theory [77–79], whereas calculations using a pre-scission point model predicts divisions into a ^{132}Sn -like light fragment and the corresponding partner [80]. The competition between these two fission modes was further analysed recently within the Langevin approach in Ref. [81]. For excitation energy $E_0^* = 10$ MeV, strongly asymmetric peaks due to ^{208}Pb were obtained in the region $Z_0 = 120 - 122$, while the influence of ^{208}Pb was found to be negligible for lighter nuclei and with symmetric yields dominating. The SA mode is however fragile as can be seen in the potential-energy paths in Fig. 4.6; increasing the energy to $E_0^* \gtrsim 8$ MeV makes it possible to cross the ridge to the symmetric valley and, correspondingly, to a larger amount of symmetric yield. This is shown Fig. 6.4, where fission of $^{274}_{108}\text{Hs}_{166}$ with $E_0^* = 10$ MeV results in a symmetric mass yield (black dashed line).

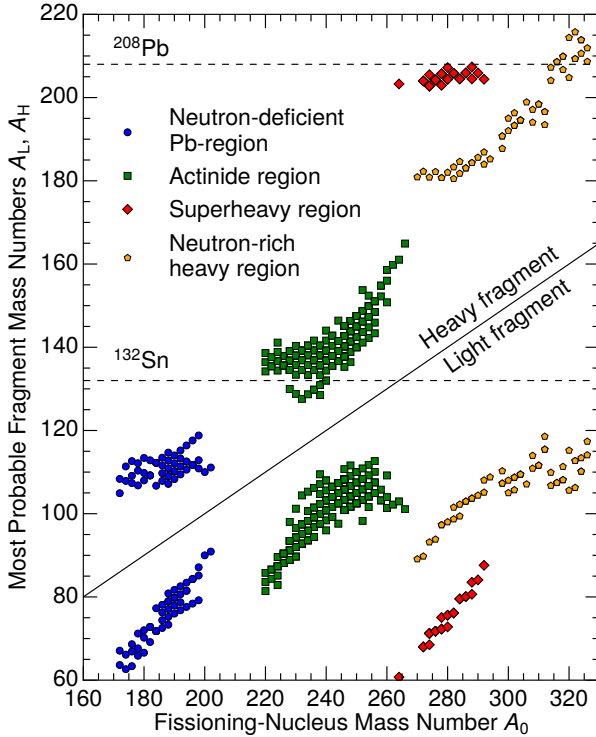


Figure 6.3: Calculated fission-fragment mass numbers following fission of nuclei in neutron-deficient Pb-region ($74 \leq Z_0 \leq 86$, $92 \leq N_0 \leq 126$), actinide ($74 \leq Z_0 \leq 96$, $132 \leq N_0 \leq 186$), superheavy ($106 \leq Z_0 \leq 114$, $156 \leq N_0 \leq 178$) and neutron-rich ($82 \leq Z_0 \leq 110$, $188 \leq N_0 \leq 218$). Only nuclei with asymmetric fission and with a symmetric-yield to peak-yield ratio less than 0.2 are included (red squares in Fig. 6.2). The figure is taken from Paper IV.

Figure 6.5 shows the calculated mass yields (solid red curves) of $^{256,258,260}\text{Fm}$, for SF ($E_0^* = 0$ MeV) (left panel), and for excitation energies E_0^* corresponding to thermal-neutron induced fission ($E_0^* \approx S_n$) (right panel). For these nuclei, a transition from asymmetric to symmetric mass yield is obtained corresponding to the north-east part of the actinide region in Fig. 6.2. For ^{256}Fm ($Z_0 = 100$, $N_0 = 156$) the St mode is the dominating mode corresponding to asymmetric yield distribution, where calculations yield a slightly broader distribution than data. The yield does not change much when the energy is increased, though the amount of symmetric yield increases slightly. In SF of ^{258}Fm there is a mixture of the symmetric SS mode and the asymmetric St mode, with fractions 55% and 45%, respectively. Although the mass yield is symmetric, it is not as narrow as in ^{260}Fm where the SS mode completely dominates for SF. When the energy is increased, the strong shell effects associated with the SS mode decreases, and the amount of asymmetric yield increases in ^{258}Fm and ^{260}Fm . For thermal fission, the SS mode has fully disappeared for ^{258}Fm in the calculations. The

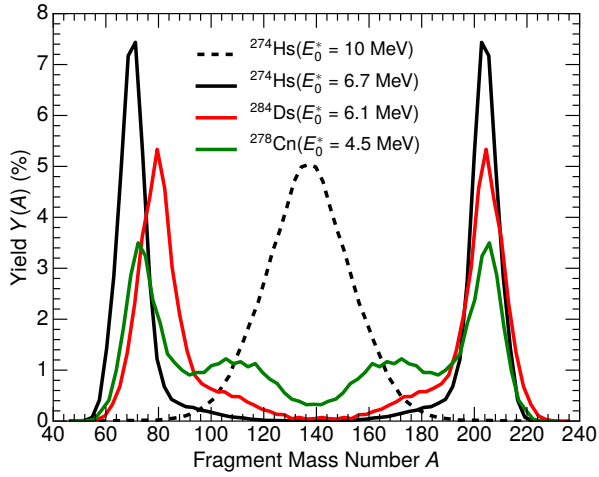


Figure 6.4: Calculated fission-fragment mass yields in ^{274}Hs , ^{278}Cn , ^{284}Ds for excitation energies $E_0^* = 6.7$ MeV, 4.5 MeV, 6.1 MeV (solid lines), respectively. Also shown is the calculated yield for ^{274}Hs with $E_0^* = 10$ MeV (black dashed line).

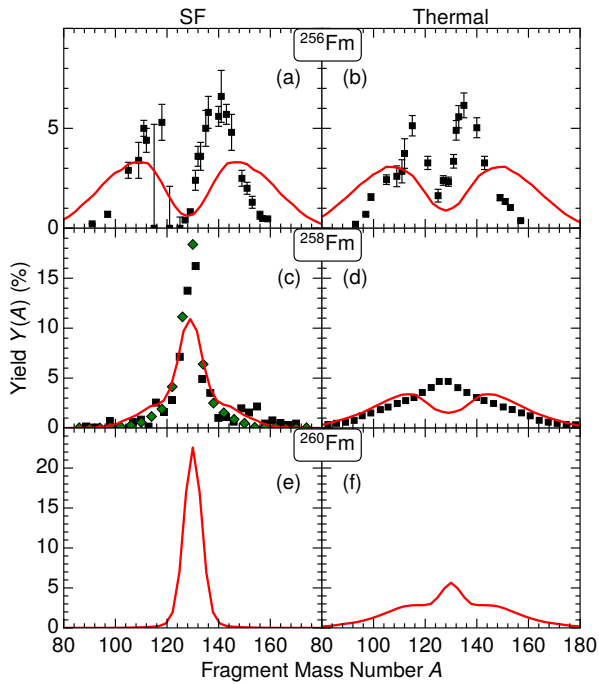


Figure 6.5: Calculated fission-fragment mass yields for SF (left panel) and thermal energies (right panel) for ^{256}Fm (a,b), ^{258}Fm (c,d) and ^{260}Fm (e,f). Results from calculations are shown by solid red lines and results from data are shown by black squares and green diamonds taken from Refs. [56, 69–73]. The experimental data all represent post-neutron evaporation mass yields.

broad symmetric yield in the data indicates however that there is some fraction of the SS mode left for ^{258}Fm , similar to calculations for thermal fission in ^{260}Fm in which 25% of the SS mode is still present.

Further results of mass and charge yields calculated within the random-walk model can be found in Refs. [22, 23, 42, 66, 75, 82–86].

6.2 Shapes of scission fragments

In addition to the mass asymmetry coordinate α , which determines fragment mass numbers A_L and A_H , the scission configurations are also characterized by the elongation q_2 of the fissioning nucleus and the spheroidal deformations ε_L and ε_H of the fragments. These deformation parameters affects the subsequent kinetic energy and excitation energy of the fragments, discussed in Ch. 7.

Figure 6.6 shows a contour plot of the location of the endpoints projected onto fragment deformation ε and fragment mass number A in $^{235}\text{U}(n, f)$ for different incident-neutron energies E_n . Both the calculated average fragment deformations at scission (solid black curves) and the ground-state deformations (black crosses) display a saw-tooth behaviour as a function of fragment mass for $E_n = 0$. However, the scission deformations tend to be below the values of the ground-states deformations, towards more oblate shapes. The St mode is dominating for this energy with mass peaks $A_L:A_H \approx 100:136$ and deformations $\varepsilon_L:\varepsilon_H \approx 0.25:-0.1$. The SL mode with two prolate fragments are obtained to some degree for the most symmetric mass splits. At higher energies, the SL mode spreads to more asymmetric mass divisions. This results in a bimodal distribution in the heavy-fragment deformation ε_H for $A_H \approx 132$, with one peak at $\varepsilon_H \approx -0.1$ due to the St mode and one peak at $\varepsilon_H \approx 0.3$ due to the SL mode.

Figure 6.7 shows the average light and heavy-fragment deformations at scission, ε_L (thin blue dashed curves) and ε_H (thick red curves), as a function of elongation q_2 for eight mass-splits in $^{235}\text{U}(n, f)$ for neutron energy $E_n = 0$ MeV. The orange histograms show the obtained q_2 distributions, $P(q_2)$, with fitted Gaussian distributions identified as the St (black curve) and SL (green curve) modes. Similar behaviour is obtained for all mass-splits with deformations $\varepsilon_L:\varepsilon_H \approx 0.3:-0.1$ for small q_2 values and $\varepsilon_L:\varepsilon_H \approx 0.3:0.3$ for larger q_2 values. The St mode is seen to be dominating except for the most symmetric mass splits $A_L = A_H = 118$. Figure 6.8 is similar to Fig. 6.7, but for $E_n = 5.55$ MeV. The average fragment deformations are very similar to those for $E_n = 0$ MeV, but the fractions of the q_2 -distributions changes, where the SL mode is

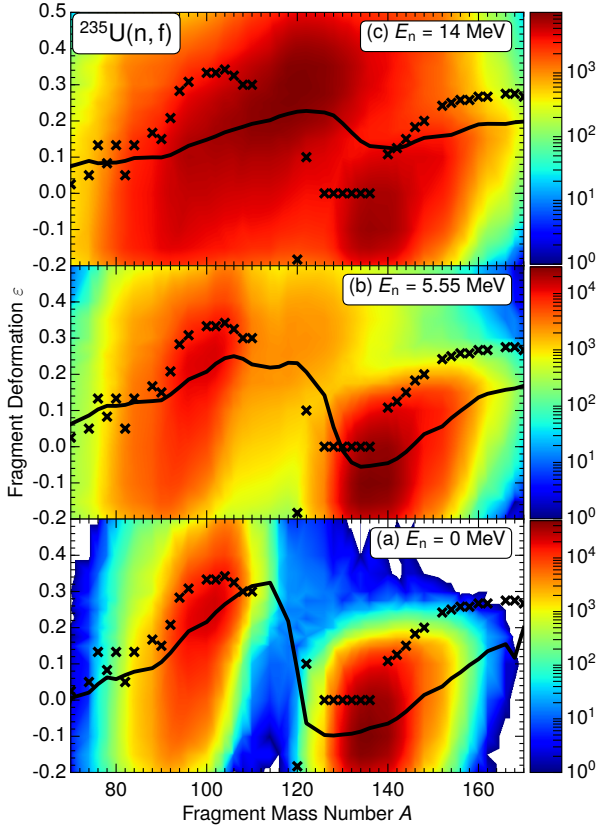


Figure 6.6: Contour plots (on a logarithmic scale) in the plane of the fragment mass number A and fragment deformation ε in $^{235}\text{U}(n, f)$ for incident-neutron energies: (a) $E_n = 0$ MeV, (b) $E_n = 5.55$ MeV, and (c) $E_n = 14$ MeV. Average deformations are shown as solid black curves and ground-state deformations are shown as black crosses.

seen to spread to more asymmetric splits. This corresponds to the bimodal distribution also seen in 6.6(b) for $A_H \approx 132$.

Figure 6.9 shows a contour plot of the location of the endpoints projected onto fragment deformation ε and fragment mass number A in ^{260}Fm for different excitation energies E_0^* . For $E_0^* = 0$ MeV, most of the events correspond to the SS mode with symmetric mass-split and two spherical fragments. At $E_0^* = 6.13$ MeV (thermal fission), the amount of asymmetric events increases due to the St mode and show a similar saw-tooth behaviour as for $^{235}\text{U}(n_{\text{th}}, f)$ in 6.6(c). When the excitation is increased further, the shell effects will eventually disappear and the most probable split correspond two prolate fragments.

The fraction of the SS mode is shown in Fig. 6.10 for even fermium isotopes

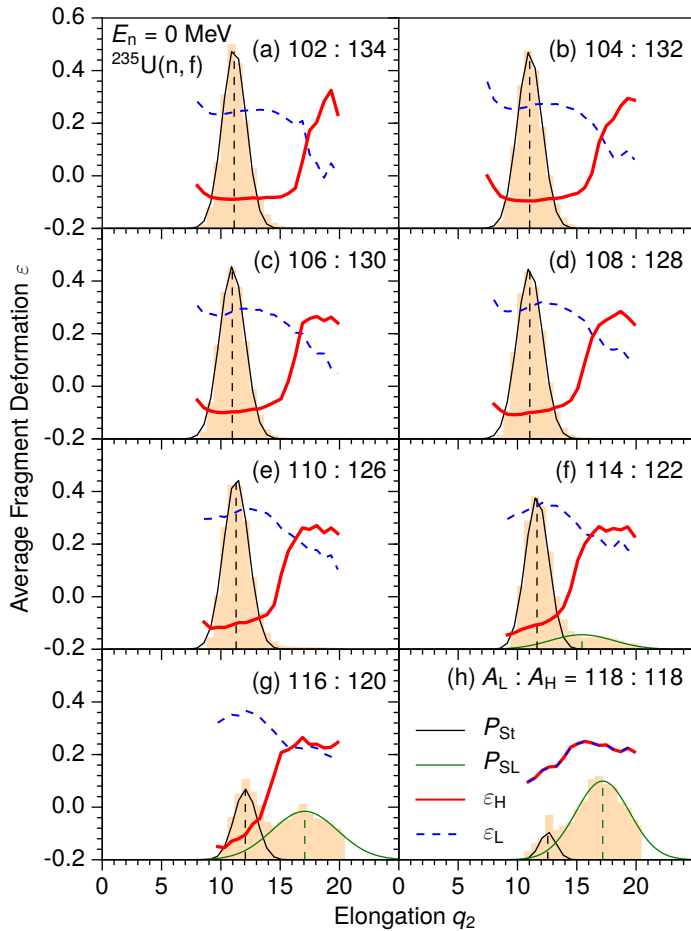


Figure 6.7: Average light and heavy-fragment deformations at scission, ε_L (thin blue dashed curves) and ε_H (thick red curves), versus elongation q_2 for selected mass-splits in $^{235}\text{U}(n, f)$. The orange histograms show the calculated q_2 distributions, $P(q_2)$, with fitted Gaussian distributions corresponding to the St (black curve) and SL (green curve) fission modes.

$^{254-268}\text{Fm}$ undergoing fission at different excitation energies. It is seen how the SS mode dominates at $E_0^* = 0$ MeV for $^{258-268}\text{Fm}$ (and probably disappears for $N_0 > 172$). But the mode is fragile and quickly disappears in ^{258}Fm as the excitation energy is increased. For ^{260}Fm the transition from a dominance of the SS mode to a dominance of the St mode appears at a slightly higher energy, about 5 MeV. For ^{264}Fm the SS mode survives to highest excitation energy, as is expected since the symmetric fission in this case corresponds to two doubly-magic ^{132}Sn nuclei.

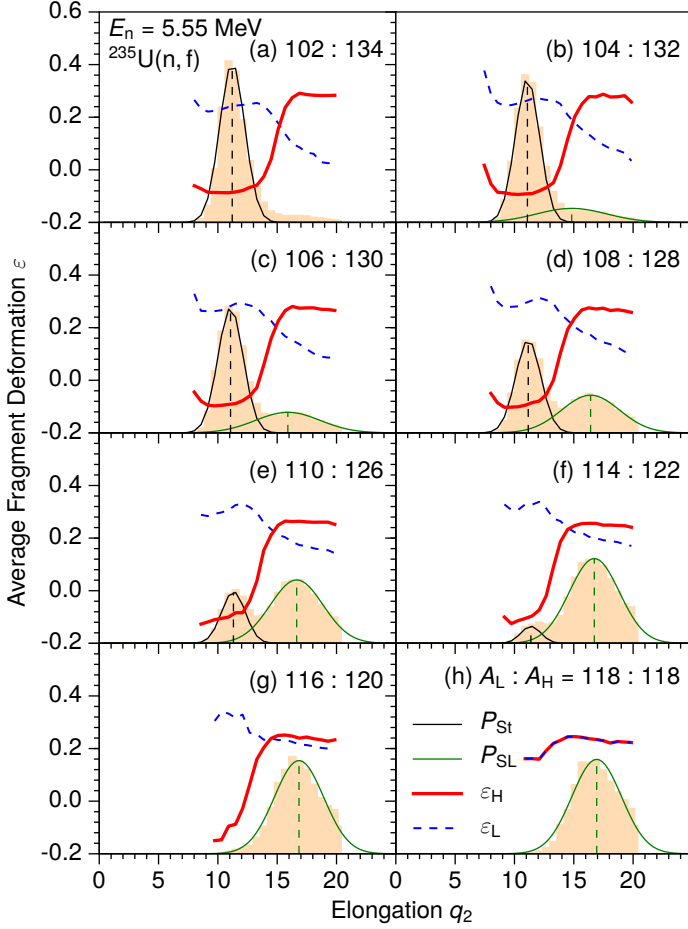


Figure 6.8: Same as Fig. 6.7 but for $E_n = 5.55$ MeV.

The calculated variation in the stability of the SS mode with increasing excitation energy can be understood from the potential-energy structure in Fig. 4.5 in Sec. 4.2. At low energies the walks are restricted to the SS valley, while the ridge towards the asymmetric St valley may be crossed at higher energies. The small slope of the energy along the SS valley between $q_2 \approx 4$ and $q_2 \approx 6$, seen for $^{258,260,262}\text{Fm}$, leads to an almost diffusive dynamics, implying several possibilities to cross the ridge. Once a transition to the St valley is made, the probability to return to the SS valley is very small, since the dynamics along the St valley is strongly driven towards scission by the large energy slope. The potential energy along the SS valley decreases with increasing neutron number and reaches its smallest values for $N_0 = 164$. Because the energy of the ridge is

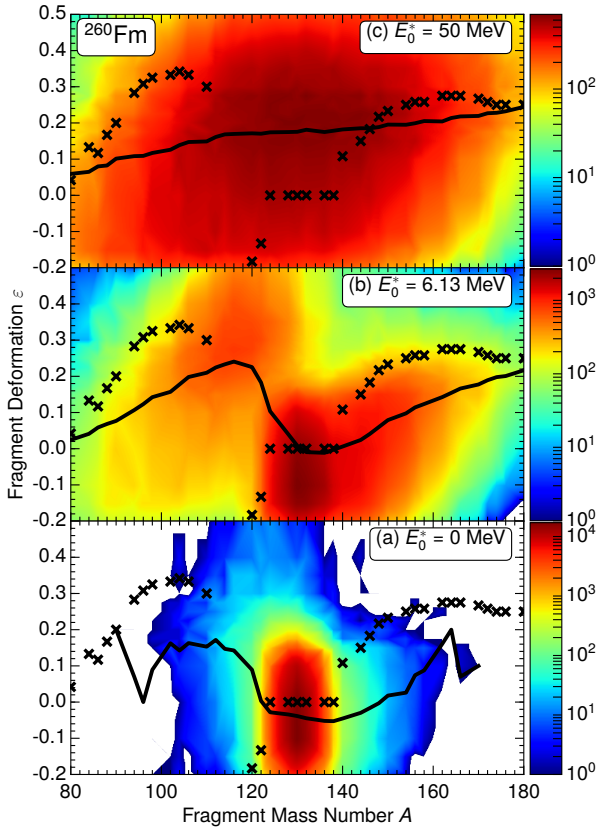


Figure 6.9: Contour plots (on a logarithmic scale) in the plane of the fragment mass number A and fragment deformation ε in fission of ^{260}Fm for initial excitation energies: (a) $E_0^* = 0$ MeV, (b) 6.13 MeV, (c) and 50 MeV. Average deformations are shown as solid black curves and ground-state deformations are shown as black crosses.

rather independent of N_0 , transitions from the SS valley to the St valley require higher energies with increasing neutron number, with a maximum for $N_0 = 164$, thus making the SS mode in those isotopes correspondingly more resilient.

Figure 6.11 shows the fragment deformations in fission of ^{274}Hs for energies $E_0^* = 6.7$ MeV (a) and $E_0^* = 10$ MeV (b). Both energies yield similar average values, whereas the majority of events are changed from asymmetric to symmetric mass-splits when the energy is increased. The heavy fragment near ^{208}Pb obtains a slightly oblate shape $\varepsilon_{\text{H}} \approx -0.1$, while the light fragment becomes prolate $\varepsilon_{\text{L}} \approx 0.3$, identified as the SA mode. This is similar to the results obtained within the Langevin approach in Ref. [81], where the fragment generally obtain a prolate shape, except near ^{208}Pb where a spherical shape is the most probable.

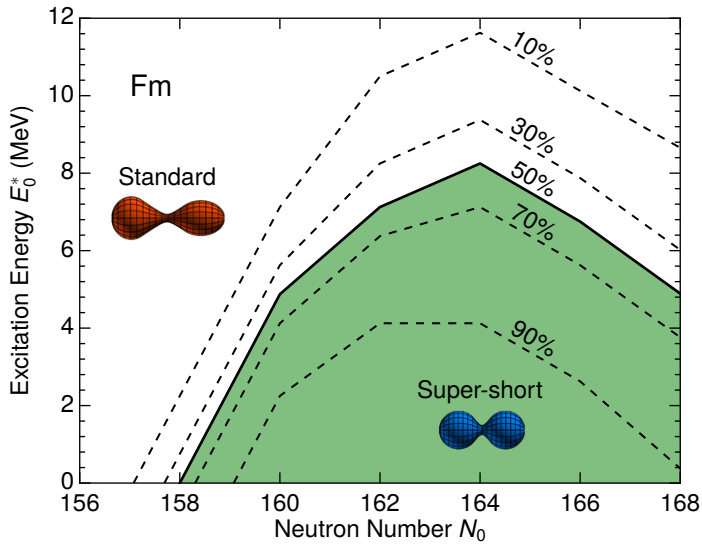


Figure 6.10: The calculated relative contribution by the SS fission mode in fermium isotopes, as a function of the neutron number N_0 and the initial excitation energy E_0^* , presented in the form of a contour plot, on which the solid line marks the 50% contour where the SS mode and the St mode contribute equally. Typical scission shapes for the two modes are also shown. The figure is taken from Paper VI.

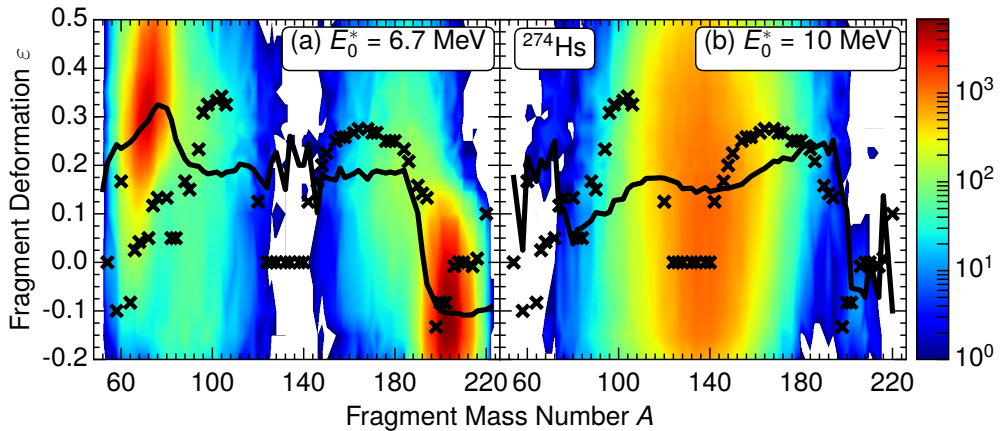


Figure 6.11: Contour plots (on a logarithmic scale) in the plane of the fragment mass number A and fragment deformation ε in fission of ^{274}Hs for initial excitation energies $E_0^* = 6.7$ MeV (a) and $E_0^* = 10$ MeV (b). Average deformations are shown as solid black curves and ground-state deformations are shown as black crosses.

Chapter 7

Energy release

Large amount of energy is released in fission due to the mass-energy relation $E = mc^2$. The majority of the energy is released in terms of kinetic energy of the two fragments, while some of the energy goes into excitation energy in the fragments. The excitation energy is subsequently dissipated through emission of particles.

7.1 Energies in the fission process

The energies involved in the fission process is schematically illustrated in Fig. 7.1. The energy curve (thick solid line) describes a path through the five-dimensional potential-energy surface that is ended at the scission point. After scission, the potential energy drops drastically mainly due to the Coulomb repulsion between the two fission fragments.

The nucleus is initially excited by the energy E_0^* , where in neutron induced fission, (n, f), this corresponds to

$$E_0^* = S_n + E_n, \quad (7.1)$$

where S_n is the neutron separation energy of the fissioning nucleus and E_n the kinetic energy of the incoming neutron. For thermal fission, (n_{th}, f), in which $E_n \approx 0$ MeV, the initial excitation energy is $E_0^* = S_n$. Together with the Q -value, this is the totally available energy in the fission process,

$$Q^* = E_0^* + M(Z_0, N_0) - M(Z_L, N_L) - M(Z_H, N_H), \quad (7.2)$$

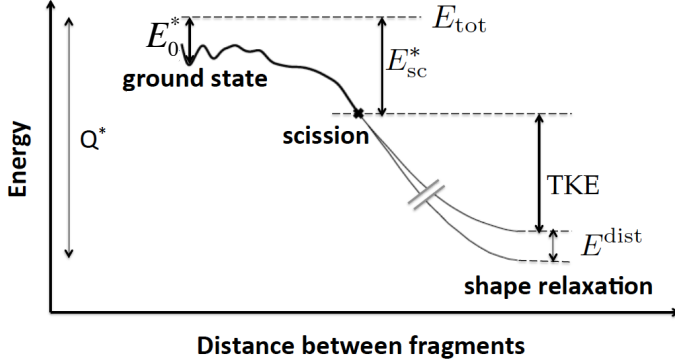


Figure 7.1: Illustration of the energies in the fission process. The thick curve shows the minimal energy of the fissioning nucleus along a typical diffusive path on the structured potential-energy landscape, until scission is reached, marked by the cross on the figure. At scission, the intrinsic energy, E_{sc}^* , is shared between the fragments. Beyond scission, the process is not explicitly calculated, and only energy conservation is applied (schematically denoted by thin lines). Beyond scission, the fragments are subject to Coulomb repulsion, which is subsequently converted to kinetic energy, and the distortion energy in each fragment is relaxed within the fragment. The totally available energy, Q^* , is composed of the initial excitation energy E_0^* and the Q -value for the considered fission process. This energy is converted into TKE of the fragments and intrinsic excitation energy in the fragments. The intrinsic excitation energy has two contributions, (a) the excitation energy at scission E_{sc}^* , and (b) the distortion energy E^{dist} .

where $M(Z_0, N_0)$ is the ground-state mass of the parent nucleus, and $M(Z_L, N_L)$ and $M(Z_H, N_H)$ are the ground-state masses of the light- and heavy fragments, respectively.

In the random-walk model, the collective kinetic energy associated with the shape evolution is assumed to be negligible prior to scission. The excitation energy at the scission point, E_{sc}^* , is then the energy difference between the total energy E_{tot} and the potential energy $U(\chi_{sc})$ at the scission configuration,

$$E_{sc}^* = E_{tot} - U(\chi_{sc}). \quad (7.3)$$

This excitation energy at scission is to be shared between the two fragments,

$$E_{sc}^* = E_L^{intr} + E_H^{intr}, \quad (7.4)$$

and is discussed in Sec. 7.3.

After time to equilibrate, the accelerated fission fragments relax their respective shapes to ground-state deformations and thereby gain a distortion energy, which is calculated as the energy difference between the fragment mass at scission and the ground-state mass,

$$E_i^{dist} = M_i(\varepsilon_i^{sc}) - M_i(\varepsilon_i^{gs}), \quad (7.5)$$

where $i = \text{L}$ or H . The total excitation energy E_i^* of a fragment is then composed by the two parts, intrinsic excitation energy and distortion energy,

$$E_i^* = E_i^{\text{intr}} + E_i^{\text{dist}}. \quad (7.6)$$

The sum of the excitation energy of the light- and heavy fragment makes up the the total excitation energy (TXE),

$$\text{TXE} = E_{\text{L}}^* + E_{\text{H}}^*. \quad (7.7)$$

In total, the available energy is thus shared between the TKE and the TXE of the fragments, i.e.,

$$Q^* = \text{TKE} + \text{TXE}. \quad (7.8)$$

The Q^* -value is calculated from Eq. (7.2) and the TXE-value from Eq. (7.7). The TKE-value is then obtained from Eq. (7.8), which corresponds to TKE of the fragments before neutron emission. After neutron emission, the fragment masses decrease somewhat, and consequently, the TKE decreases slightly (if the fragment speed is assumed to be unchanged). Calculated results in the thesis represent TKE before neutron emission.

7.2 Fragment kinetic energy

The dependence of the average TKE on the heavy-fragment mass number is shown in Fig. 7.2(a) for $^{235}\text{U}(n_{\text{th}}, f)$. Two different scission scenarios are considered. The first scenario uses $c_{\text{sc}} = 2.5$ fm, the neck radius at which the mass division is assumed to freeze out. The corresponding scission configurations are relatively compact and the resulting TKE values exceed the experimental data significantly for all divisions. This suggests that the fragments maintain contact for a while after their masses have been determined. Therefore we assume that the effective loss of contact occurs later or when the neck radius has shrunk further to $c_{\text{sc}} = 1.5$ fm. The corresponding shapes are then more elongated and, consequently, the resulting TKE values are lowered. Furthermore, the internal excitation energies are higher and the emerging fragments have larger quadrupole moments.

In the region beyond $A_{\text{H}} \geq 132$, where the average TKE exhibits a steady decrease with A_{H} , the experimental data are very well reproduced by the calculations. However, in the more symmetric region, the extracted TKE values exceed the measured values considerably, by up to 20 MeV. This discrepancy may be due to the extraordinary elongation of the associated scission shapes

which may not be adequately described within the 3QS shape family in terms of which the potential-energy surface has been calculated. An insufficient elongation leads to an over-prediction of TKE and an underestimate of the intrinsic excitation energy.

As seen in Fig. 7.2(c), the width of the TKE distribution for a given A_H is underestimated in the calculations for both scission conditions, but the agreement with data is generally better for the adopted value, $c_{sc} = 1.5$ fm, than for $c_{sc} = 2.5$ fm. For the employed value, the underestimation is about 50% in the region of symmetric fission and decreases with increasing fission-fragment asymmetry. The underestimation may (at least in part) be due to the fact that the calculations include only even-even fragment pairs having (approximately) equal N/Z ratios, namely, that of ^{236}U . As a consequence of this restriction, there is only one (N, Z) combination for a given A , whereas the actual fission process populates several combinations and thus leads to a broader TKE distribution.

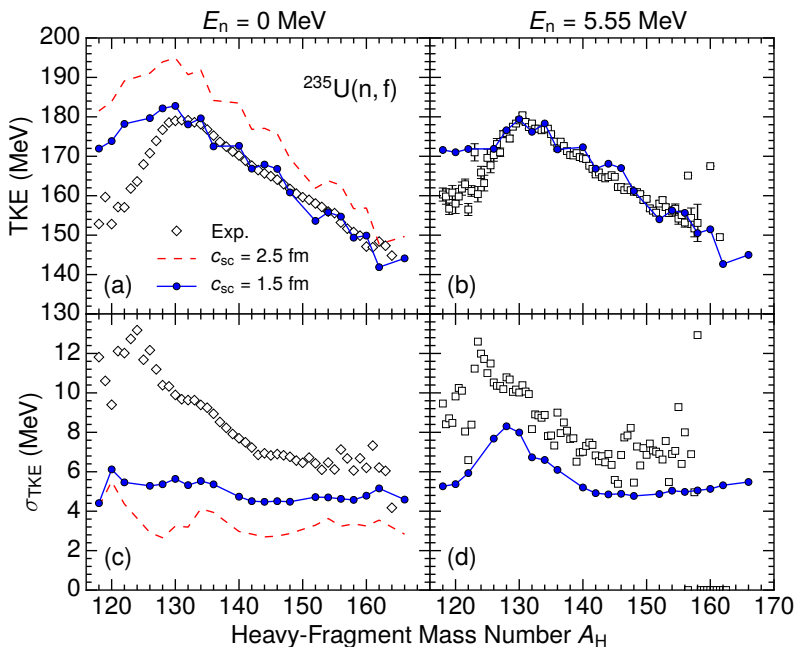


Figure 7.2: Panel (a) shows the average pre-neutron TKE versus the heavy-fragment mass number A_H for $^{235}\text{U}(n_{th}, f)$ for two values of the scission neck radius, $c_{sc} = 1.5$ fm (filled circles connected by solid blue lines) and $c_{sc} = 2.5$ fm (dashed red line). In (c) the calculated width of the TKE distribution, σ_{TKE} , is shown for the same two values of c_{sc} . Panels (b) and (d) are similar to (a) and (c), but are for a higher incident-neutron energy, $E_n = 5.55$ MeV, and only results for the adopted scission radius, $c_{sc} = 1.5$ fm, are shown. Measured values of TKE are shown for thermal fission [87] (open diamonds) and for $E_n = 5.55$ MeV [88] (open squares). The figure is taken from Paper V.

Figures 7.2(b) and 7.2(d) show the average TKE and the width σ_{TKE} , respectively, versus the heavy-fragment mass number for incoming neutron of energy $E_n = 5.55$ MeV. The measured TKE values are very well reproduced not only for $A_H \geq 132$, as was the case for thermal fission [see Fig. 7.2(a)], but even down to $A_H = 126$, leaving only a rather narrow region around symmetry with a significant overestimate, by up to 10 MeV. Also the calculated widths agree better with data for energetic than for thermal neutrons [Fig. 7.2(d)], though the calculated values generally are too small. Furthermore, the data exhibits a maximum in σ_{TKE} at small A_H values and the calculations yield a similar feature. This maximum is related to the bimodal structure in the heavy-fragment deformation around $A_H \approx 130$, discussed in Sec. 6.2.

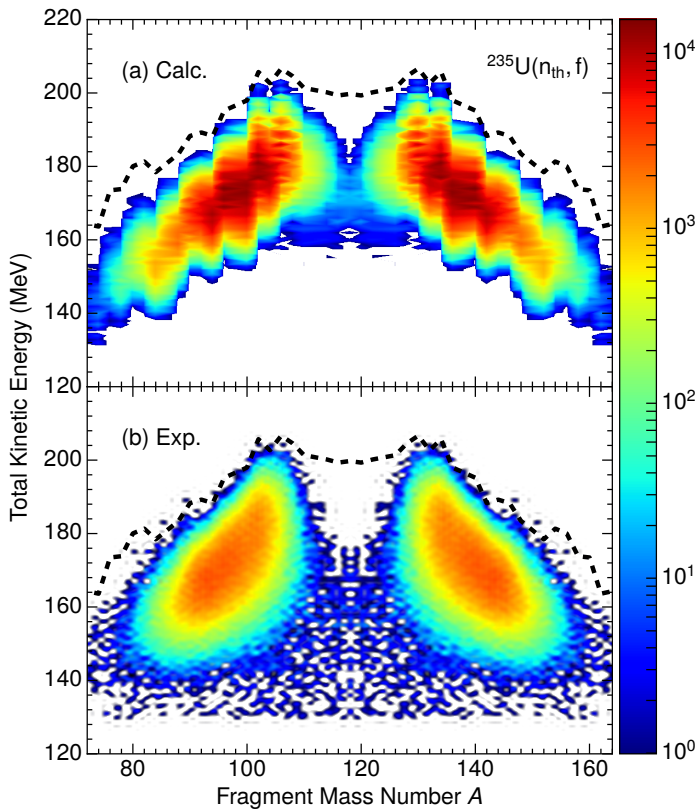


Figure 7.3: Number of scission events in log scale versus fission-fragment mass number A and pre-neutron TKE for $^{235}\text{U}(n_{\text{th}}, f)$. (a) Calculated results with $c_{\text{sc}} = 1.5$ fm. (b) Experimental data from Ref. [87]. The dashed curve shows Q^* values for different fragment masses. The experimental number of events is scaled to the same number of events as calculated. The jaggedness of the calculated contour plot is due to the selection of even-even mass numbers, and the finiteness of the calculational grid in TKE. The experimental results contain a certain degree of smearing due to uncertainty in measured mass numbers. The figure is taken from Paper V.

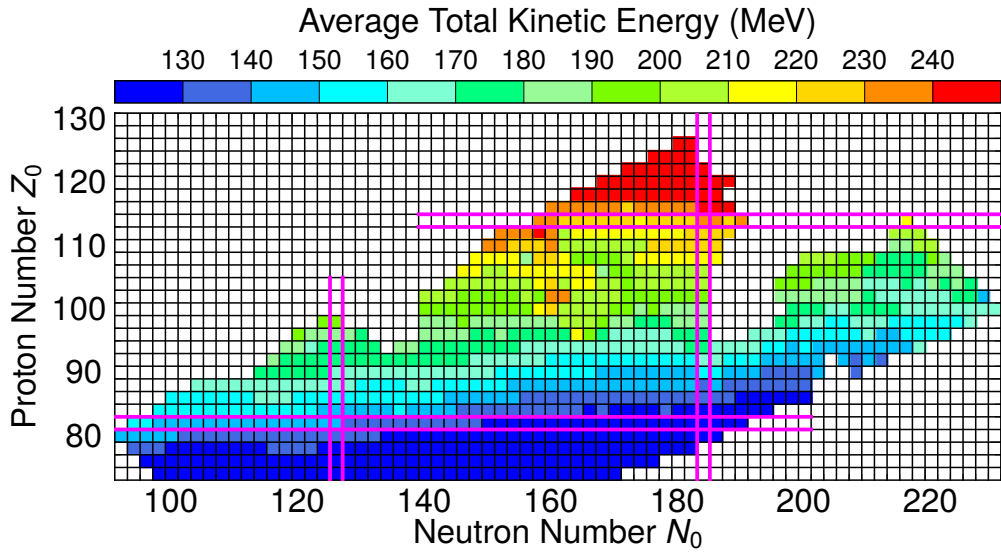


Figure 7.4: Calculated average fission-fragment TKE following fission of heavy nuclei. The figure is taken from Paper IV.

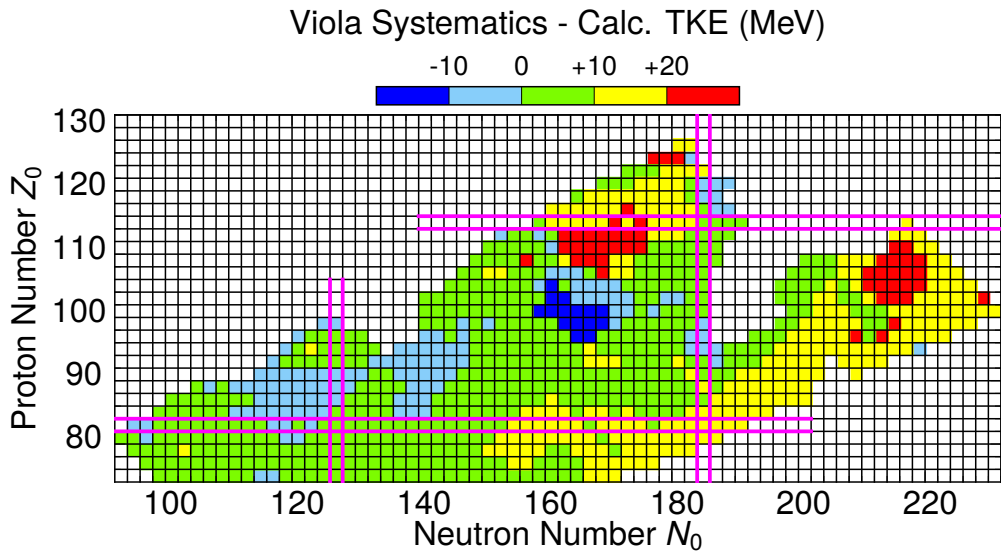


Figure 7.5: Viola TKE systematics minus calculated average TKE. The figure is taken from Paper IV.

Figure 7.3 shows contour plots of the calculated (a) and measured (b) number of fission events with respect to fragment mass number A and TKE for $^{235}\text{U}(n_{\text{th}}, f)$.

The restriction of fixed N/Z ratio implies that there is a definite Q^* value for each mass division, $Q^*(A)$, which represents the maximum possible TKE value attainable in the calculations. It is shown by the dashed curve in both panels of Fig. 7.3 and it can be seen that the bulk of the events lie well below this boundary, both theoretically and experimentally. In reality a particular mass division can lead to fragments with a variety of N/Z ratios, leading to a corresponding range of Q^* values for each A .

The calculated average TKE values for the entire region of study in Fig. 6.2 are shown in Fig. 7.4, where the TKE values are seen to generally increase for heavier nuclei. More easily interpretable is the difference between the Viola

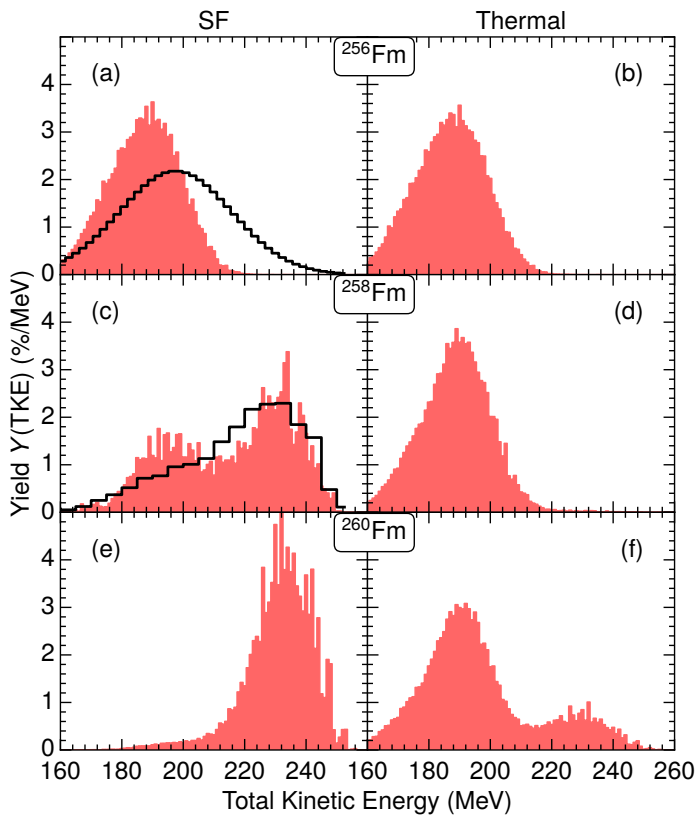


Figure 7.6: TKE yields for SF (left panel) and thermal energies (right panel) for ^{256}Fm (a,b), ^{258}Fm (c,d), and ^{260}Fm (e,f). Results from calculations are shown by red histograms and results from data is shown by black histograms taken from Ref. [72] (^{256}Fm , unspecified if before or after neutron emission) and Ref. [56] (^{258}Fm , post-neutron emission).

TKE systematics [95]

$$\text{TKE}^{(\text{Viola})} = 0.1189Z_0^2/A_0^{1/3} + 7.3 \text{ MeV}, \quad (7.9)$$

and the actually calculated average TKE. This is illustrated in Fig. 7.5. In their main features, the Viola TKE systematics are well reproduced in the calculations. In the region of very asymmetric fission below $Z_0 = 114$ ($N_0 \approx 162\text{--}174$) the TKE is lower than the systematics. Also in the heavy neutron-rich region ($N_0 \approx 210\text{--}220$), where we obtain asymmetric fission yields, the average TKE is lower than given by the Viola systematics.

254–268 Fm

Large values of the TKE are seen near ^{258}Fm due to the presence of the SS mode and are also seen experimentally [56, 72, 93, 96, 97]. Figure 7.6 shows calculated TKE distributions (red histograms) compared to data (black curves) for the isotopes ^{256}Fm , ^{258}Fm , and ^{260}Fm for SF (left panel) and thermal fission (right panel). Fission of ^{256}Fm exhibits a single Gaussian distribution peaked at $\text{TKE} \approx 190$ MeV, corresponding to fission in the St mode for both energies. The mixture of the St mode and SS mode for SF in ^{258}Fm results in a bimodal distribution, which is also seen in the data. In ^{260}Fm , the SS mode is dominating for SF and this yields a single-humped distribution peaked at the higher value $\text{TKE} \approx 230$ MeV. For thermal fission, there is a mixture of the two modes also in ^{260}Fm and a bimodal distribution is obtained.

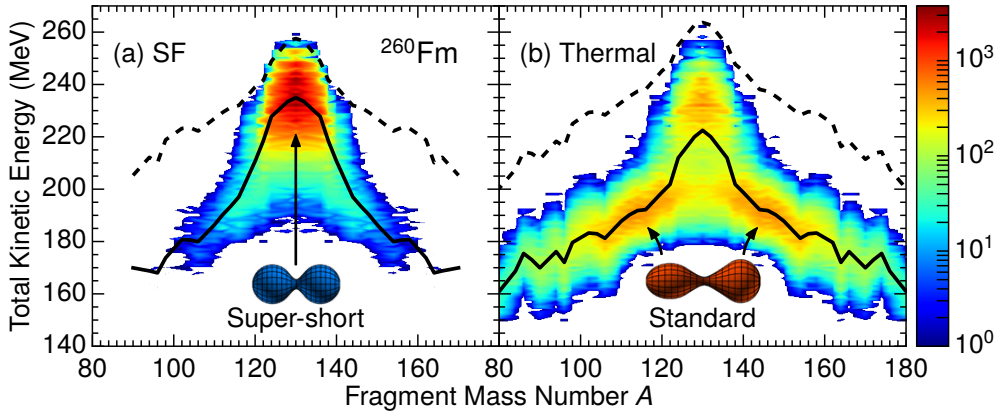


Figure 7.7: Contour plots (on a logarithmic scale) for ^{260}Fm in the plane of the fragment mass number A and TKE based on SF (a) or thermal (b) fission events. Also shown are Q^* (dashed lines) and the average TKE (solid lines) for each A . Typical scission shapes are shown for the compact, symmetric SS and the elongated, asymmetric St modes. The figure is taken from Paper VI.

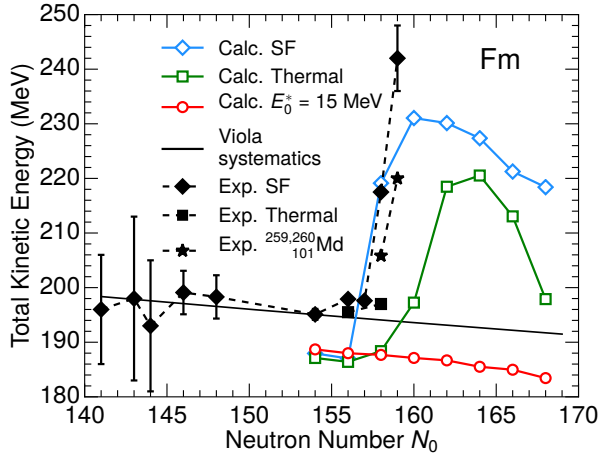


Figure 7.8: Average TKE from fission of fermium isotopes versus neutron number N_0 . For even $^{254-268}\text{Fm}$, theoretical results (before neutrons emission from fragments) are shown as open symbols for SF (blue diamonds), thermal fission (green squares) and $E_0^* = 15$ MeV (red circles). Experimental data are shown as filled black diamonds (SF) [56, 69, 89–93] and filled black squares (thermal fission) [73, 94]. Data for ^{259}Fm show most probable TKE value. Some of the data correspond to TKE of fragments before neutrons emission and some to after neutron emission (for $^{246,248}\text{Fm}$ the difference is about 3 MeV, which is within the error bars [90]). The solid line shows Viola systematics [95] given by Eq. (7.9). The black stars show SF data for neighbouring nuclei $^{259,260}_{101}\text{Md}$ [56]. The figure is taken from Paper VI.

Figure 7.7 shows the number of scission events for ^{260}Fm versus fragment mass number and TKE for (a) SF and (b) $E_0^* = 6.13$ MeV (thermal fission). For SF most events are seen to occur in the SS mode with symmetric fragment masses with large TKE values. Increasing the excitation energy to $E_0^* = 6.13$ MeV gives a very different distribution of TKE-values. Compared to SF the number of events in the SS mode has decreased, and many events now occur in the St mode at low TKE with an asymmetric division of fragment masses. Projecting the scission events shown in Fig. 7.7 on the TKE-axis yields the two TKE distributions shown in 7.6(e) and (f). Typical shapes of the two modes are shown in Fig. 7.7(a) and (b).

Figure 7.8 shows the average TKE for even $^{254-268}\text{Fm}$ versus the neutron number N_0 of the fissioning nucleus for three different excitation energies, and provides an experimental correspondence to the phase diagram in Fig. 6.10. Experimental data for the lighter isotopes $N_0 < 158$ are reasonably described by the linear behaviour of the Viola systematics. For SF the SS mode starts playing a role at $N_0 = 158$, where TKE is seen to increase suddenly, both in data and calculations. A similar increase is also seen in data for neighbouring nuclei $^{259,260}\text{Md}$ (black stars). For thermal fission ($E_0^* \approx 6$ MeV) the SS mode dominates for $^{260-268}\text{Fm}$ resulting in large TKE-values. And finally, for 15 MeV all nuclei are found to

fission in the St mode, and the TKE-values are small for all isotopes with similar linear behaviour as the Viola systematics.

^{274}Hs

Figure 7.9 shows calculated scission events for ^{274}Hs versus fragment mass number and TKE for (a) $E_0^* = 6.7$ MeV and (b) $E_0^* = 10$ MeV. The average TKE values are shown as solid black lines, while the total available energy Q^* are shown as dashed black lines. The compact scission shapes around $A_L:A_H \approx 66:208$, associated with the SA mode, result in large TKE values that are close to the maximum possible value Q^* . The corresponding average TXE of the fragments, given by the difference between the curves for Q^* and TKE, is only about 20 MeV for the SA mode. Conversely, the TXE value for the symmetric mass-splits in Fig. 7.9(b) is about 80 MeV. The change from asymmetric to symmetric fission when the energy is increased then leads to an increase in average TXE of about 60 MeV. As will be discussed in Ch. 8, this in turn results in a large difference in the number of neutrons emitted from the fragments.

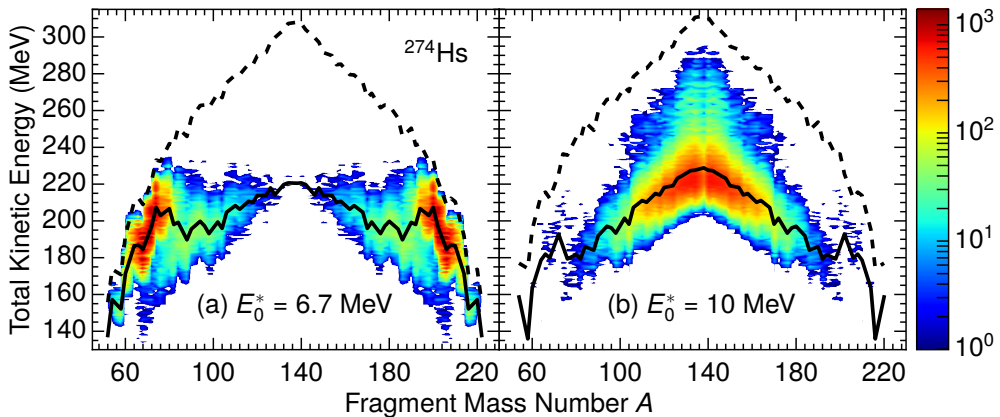


Figure 7.9: Contour plots (on a logarithmic scale) for ^{274}Hs in the plane of the fragment mass number A and TKE for excitation energies $E_0^* = 6.7$ MeV (a) and 10 MeV (b). Also shown are Q^* (dashed lines) and the average TKE (solid lines) for each A .

7.3 Fragment excitation energy

After the fissioning nucleus has split, the resulting fission fragments relax back to their ground-state deformations. The associated distortion energies are then

converted into statistical fragment excitations after scission, and it is only the intrinsic excitation energy E_{sc}^* in the fissioning nucleus that is shared between the nascent fragments. The distortion energy, obtained with Eq. (7.5), and the intrinsic excitation energy then makes up the total excitation in the fragment which subsequently goes to evaporation of neutrons.

It has long been puzzling that the heavy fragment emits fewer neutrons than the light fragment in low-energy fission of actinides (see Ch. 8). This indicates that the heavy fragment obtains a smaller amount of excitation energy than the light fragment, which appears to differ from simple statistical expectations. If the two nascent fragments are assumed to be in thermal equilibrium at scission, the excitation energy is divided between the two fragments according to their level densities. Employment of the simplified FG level density $\rho_{\text{FG}}(E^*) \sim \exp(2\sqrt{aE^*})$ as in previous studies [98–100], results in an energy division in proportion of the mass ratio of the fragments, $E_{\text{L}}^{\text{intr}}/E_{\text{H}}^{\text{intr}} = A_{\text{L}}/A_{\text{H}}$. However, as was recently pointed out by Schmidt and Jurado [101], the simplified FG level density may be misleading at low energies where structure effects tend to be significant. They instead used the constant-temperature level density $\rho(E^*) \sim \exp(E^*/T)$ [102], where the initial temperature T of a fragment was

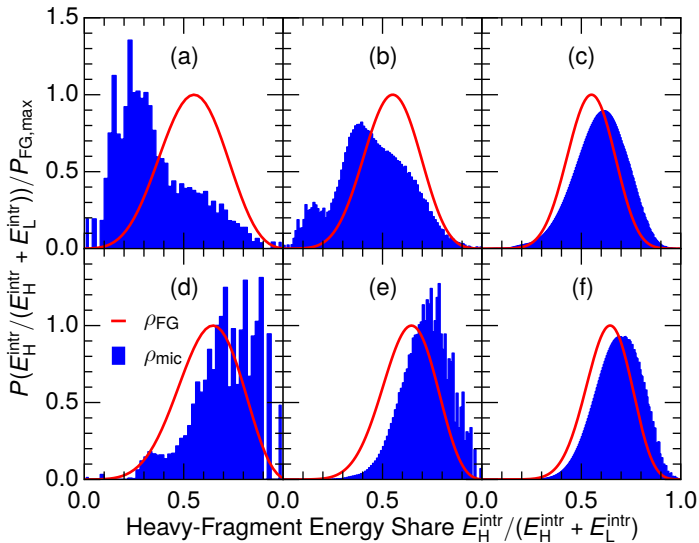


Figure 7.10: The distribution function $P(E_{\text{H}}^{\text{intr}}; E_{\text{sc}}^*)$ for the total excitation of the heavy fragment in $^{235}\text{U}(\text{n}, \text{f})$ for two different divisions, either $(N, Z, \varepsilon)_{\text{H}} = (80, 50, -0.1)$ and $(N, Z, \varepsilon)_{\text{L}} = (64, 42, 0.3)$ (top panels) or $(N, Z, \varepsilon)_{\text{H}} = (92, 60, 0.1)$ and $(N, Z, \varepsilon)_{\text{L}} = (52, 32, 0.1)$ (bottom panels), and three different values of the available energy at scission $E_{\text{sc}}^* = 10$ (left column), 20 (center column), 40 (right column) MeV. The distributions obtained from microscopic (blue histograms) and FG (solid red curves) level densities are normalized to the maximum value of the FG result. The figure is taken from Paper I.

parametrized with an expression containing a shell-effect term. This leads to an “energy-sorting mechanism”, in which energy flows from the hot to the cold fragment, and all intrinsic excitation energy is found in the fragment with the lower initial temperature T . When the heavy fragment is close to the ^{132}Sn , its temperature is increased due to strong shell effects, and the excitation energy then goes to the light fragment.

In the present studies, we also assume that thermal equilibrium is obtained at scission, but divide the the total intrinsic excitation energy available at scission E_{sc}^* based on microscopically calculated level densities of the fragments at their scission shapes. The intrinsic excitation energy of the heavy fragment, $E_{\text{H}}^{\text{intr}}$, is then governed by the following micro-canonical distribution,

$$P(E_{\text{H}}^{\text{intr}}; E_{\text{sc}}^*) \sim \tilde{\rho}_{\text{H}}(E_{\text{H}}^{\text{intr}}; \varepsilon_{\text{H}}^{\text{sc}}) \cdot \tilde{\rho}_{\text{L}}(E_{\text{sc}}^* - E_{\text{H}}^{\text{intr}}; \varepsilon_{\text{L}}^{\text{sc}}), \quad (7.10)$$

where $E_{\text{L}}^{\text{intr}} = E_{\text{sc}}^* - E_{\text{H}}^{\text{intr}}$ due to energy conservation, and where $\tilde{\rho}_i(E_i^*; \varepsilon_i^{\text{sc}}) = \tilde{\rho}(N_i, Z_i, E_i^*; \varepsilon_i^{\text{sc}})$ is the effective density of states (defined below) of a nucleus with neutron and proton numbers N_i and Z_i , spheroidal deformation ε_i , and an excitation energy of E_i^* , with $i = \text{H}, \text{L}$.

The fragment level densities $\rho_i(E_i^*, I_i; \varepsilon_i^{\text{sc}})$ at the corresponding fragment shapes at scission are calculated by employing the combinatorial method described in Sec. 3.2. Since we are interested in the energy distribution only, we sum over

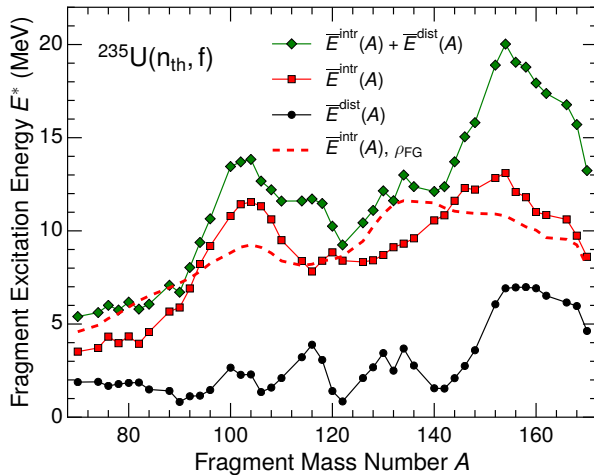


Figure 7.11: The mean fragment distortion energy $\overline{E}^{\text{dist}}(A)$ (black circles), the mean intrinsic excitation energy $\overline{E}^{\text{intr}}(A)$ (red squares), and the sum, $\overline{E}^{\text{dist}}(A) + \overline{E}^{\text{intr}}(A)$ (green diamonds) are shown as functions of the fragment mass number A for $^{235}\text{U}(n_{\text{th}}, f)$. The red dashed curve show $\overline{E}^{\text{intr}}(A)$ with the simple FG level density (red dashed curve). The figure is taken from Paper I.

the fragment angular momentum, I_i , to obtain the effective density of states entering in Eq. (7.10),

$$\tilde{\rho}_i(E_i^*; \varepsilon_i^{\text{sc}}) = \sum_{I_i} (2I_i + 1) \rho_i(E_i^*, I_i; \varepsilon_i^{\text{sc}}). \quad (7.11)$$

Figure 7.10 shows the energy distribution $P(E_{\text{H}}^{\text{intr}}; E_{\text{sc}}^*)$ at three different values of the total available energy E_{sc}^* for two different mass divisions of ^{236}U having $(A_{\text{H}}:A_{\text{L}}) = (130:106)$ and $(152:84)$. The energy distribution is calculated with both the microscopic level density discussed above and the simple macroscopic FG level density, $\rho_{\text{FG}}(E^*) \sim \exp(2\sqrt{aE^*})$ with $a = A/(8 \text{ MeV})$. Both yield rather broad distributions due to the smallness of the nuclear system. The macroscopic form yields smooth Gaussian-like distributions peaked at $E_{\text{H}}^{\text{intr}}/E_{\text{L}}^{\text{intr}} = A_{\text{H}}/A_{\text{L}}$, whereas the microscopic form yields irregular distributions that may have qualitatively different appearances, especially at lower values of E_{sc}^* where quantal structure effects are most significant. In particular, it is possible that one fragment receives all the available energy with the partner fragment being left without excitation. Although the probability for this decreases quite rapidly with increasing E_{sc}^* , this feature is in dramatic contrast to the macroscopic result.

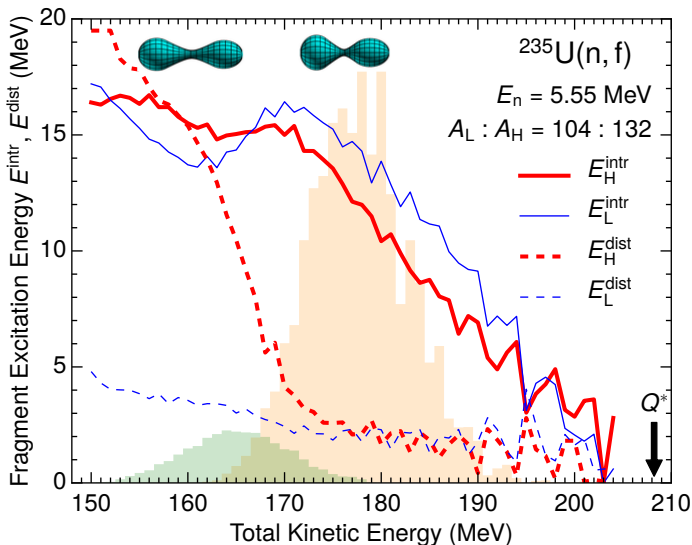


Figure 7.12: Fragment excitation energy as a function of TKE in $^{235}\text{U}(n, f)$ for incident-neutron energy $E_n = 5.55 \text{ MeV}$ and mass split $A_{\text{L}}:A_{\text{H}} = 104:132$. Probability densities are shown for the two modes: SL (green area), and St (orange area). Typical scission shapes of the SL and St modes are also shown. The figure is taken from Paper V.

For each scission configuration obtained at the end of the Metropolis walk, the excitation energies of the nascent fragments are sampled from the appropriate microscopic partition distribution. For $^{235}\text{U}(n_{\text{th}}, f)$, the resulting mean intrinsic excitation energy $\overline{E}^{\text{intr}}(A)$ is shown in Fig. 7.11 as a function of the fragment mass number A , together with the mean fragment distortion energy $\overline{E}^{\text{dist}}(A)$, as well as the sum of these two quantities which represents the total excitation energy of the fragment. The figure also shows the mean excitation energy obtained with the simple FG level density to illustrate the effect of the microscopic level densities.

Figure 7.12 shows the separate contributions to the final fragment excitation energy from their intrinsic and distortion energies at scission, displayed versus the resulting TKE for $A_L:A_H=104:132$ in $^{235}\text{U}(n, f)$ with $E_n = 5.55$ MeV. The black arrow indicates the maximum possible kinetic energy allowed by the Q^* -value. For such an event to take place the fragments have to be emitted in their ground-state deformations and with no intrinsic excitation energy; all available energy would then be transferred into kinetic energy of the fragments. The majority of the events correspond to fission in the St mode (orange histogram) centered at $\text{TKE} \approx 178$ MeV, while the SL mode (green histogram) also is present in this case for lower values at $\text{TKE} \approx 164$ MeV.

The results in Fig. 7.12 can be understood by comparing with Fig. 6.8(b), where the fragment deformations vs. q_2 are shown for the same mass split. The elongation q_2 roughly corresponds to the TKE of the fragments, while the fragment deformation, relative its ground-state shape, corresponds to the distortion energy. Since the heavy fragment $A_H = 132$ is spherical in the ground state, the small deformations at small q_2 (large TKE) results in low distortion energy, while the large deformation $\varepsilon_H \approx 0.3$ at large q_2 (low TKE) results in large amounts of distortion energy.

Chapter 8

Neutron evaporation from fragments

The majority of the excitation energy in the fragments is dissipated by emission of neutrons. The relaxation of the fragments from their scission shapes to their ground-state shapes is assumed to occur at a shorter time scale than the subsequent neutron evaporation [103]. The neutrons are therefore evaporated from fragments in their ground-state deformations. The fragments may also release the excitation energy through other decay channels, such as photon emission, but neutron emission is typically the fastest decay. When all of the excitation energy for neutron emission has been exhausted, the remaining excitation energy is used to emit photons. Only neutron emission is considered in the present studies.

8.1 Formalism

The random-walk calculations give rise to a set of fission fragments having different proton and neutron numbers. Associated with each fragment is a probability function that describes how common it is to find the fragment with a specific excitation energy. Considering a single fragment in its ground state with a certain excitation energy we assume that it cools by evaporating neutrons. Several neutrons may be evaporated in sequence until the energy of the remaining nucleus falls below the neutron separation energy threshold. Concerning the energy available for neutron emission, we assume that the rotational energy E_{rot} of the initial fission fragment can not be used for neutron emission.

How many neutrons that evaporates will also depend on how much kinetic energy each neutron flies away with. The amount of kinetic energy taken away by a neutron follows a statistical distribution. This distribution is obtained by considering the probability per unit time of a mother nucleus emitting a neutron with kinetic energy between ϵ_n and $\epsilon_n + d\epsilon_n$ [104]:

$$N\sigma(E_A^*, \epsilon_n)\epsilon_n\rho_{A-1}(E_{A-1}^*)d\epsilon_n. \quad (8.1)$$

For our purpose N can be considered a constant since it is independent of ϵ_n . ρ_{A-1} is the level density of the daughter nucleus after neutron evaporation evaluated at energy $E_{A-1}^* = E_A^* - S_n - \epsilon_n$, where E_A^* is the initial excitation energy and S_n denotes the neutron separation energy of the evaporating nucleus. In this formula, the emission probability is expressed in terms of the cross section $\sigma(E_A^*, \epsilon_n)$ for the inverse problem of compound nucleus formation through neutron capture. The energy dependence of this process can be taken into account using optical-model potentials [98]. However, in the present approach we adopt the original estimate [104] of an energy independent cross section. The resulting formula can then be expressed as

$$\tilde{N}\epsilon_n\rho_{A-1}(E_A^* - S_n - \epsilon_n)d\epsilon_n. \quad (8.2)$$

This gives the relative probabilities for neutrons evaporating with different kinetic energies. We assume that $E_{A-1}^* > E_{\text{rot}}$, i.e. that the rotational energy of the initial fission fragment is not converted into neutrons. This gives the possible range of neutron kinetic energies as $0 < \epsilon_n < E_A^* - S_n - E_{\text{rot}}$.

A neutron kinetic energy can then be drawn from a random ensemble having Eq. (8.2) as a probability distribution function [105]. Fig. 8.1 shows the probability distribution function for nucleus ${}^{140}_{54}\text{Xe}_{86}$, which is a typical fragment in fission of ${}^{236}\text{U}$. The peak in the distribution is located at $\epsilon_n \approx 1$ MeV for the lowest energy. Irregularities in the distribution are seen due to structure effects in the level density at low energies. For higher excitation energies, the distributions become wider and the location of the peak increases slightly.

If the resulting energy of the daughter nucleus is sufficient, the evaporation process is repeated until neutron emission is no longer energetically possible. New neutron energies are drawn from the corresponding ensemble and the process is restarted and repeated through the chain until a converged value for the average number of emitted neutrons is obtained. Since the initial fission fragment nucleus has a distribution of excitation energy, the event-by-event simulation must be performed for several initial energies and the resulting number of emitted neutrons are then weighted together accordingly. Summing the number of emit-

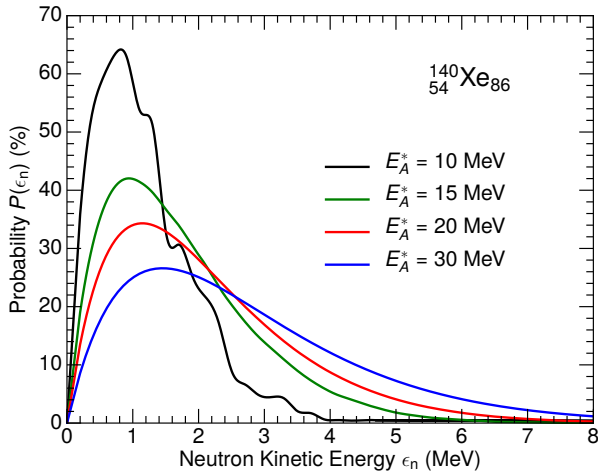


Figure 8.1: Probability density distribution $P(\epsilon_n)$ for the kinetic energy of evaporated neutron from nucleus ${}^{140}_{54}\text{Xe}_{86}$. Results are shown for different initial excitation energies E_A^* . Irregularities in the distribution are seen due to structure effects in the level density at low energies.

ted neutrons from all fission fragments and weighting with their fission yields gives the total neutron multiplicity of the nucleus.

8.2 Neutron multiplicities

Figure 8.2 shows the calculated mean neutron multiplicity $\bar{\nu}(A)$ in ${}^{235}\text{U}(\text{n}_{\text{th}}, \text{f})$ together with experimental data from a variety of experiments. The jaggedness in the calculations arise due to the restriction of even Z and N in the fragments, which leads to jumps in the neutron separation energy between neighbouring fragments. The observed sawtooth behavior (minima at $A \approx 76, 126$ and maxima at $A \approx 110, 156$) is reasonably well reproduced by the calculation and arises from a combined effect of the behavior of the neutron separation energy $S_n(A)$, which displays a jump near $A = 132$ due to the closed shells at $Z = 50$ and $N = 82$, and the behavior of the total fragment energy (see Fig. 7.11). The shortfall of $\bar{\nu}(A)$ in the region around $A = 110$ arises from the fact that the calculations lead to too large TKE values for mass divisions near symmetry (see Fig. 7.2(a)), and thus too low excitation energy. Figure 8.3 shows the total neutron multiplicity distribution for incident neutron with thermal energy. The calculated distribution capture the overall behaviour, though the experimental data shows a slightly broader distribution.

The energy dependence of the neutron multiplicity is illustrated in Fig. 8.4 which

shows $\bar{\nu}(A)$ resulting from fission at three different incident neutron energies. In the region around $A \approx 130$, the low neutron multiplicity occurring for thermal fission grows rather rapidly with increasing neutron energy, causing the sawtooth feature of $\bar{\nu}(A)$ to weaken. One reason for this behavior is due to the decrease of the strong negative shell correction at higher excitation energy for fragments in this mass region, increasing the level density and thus the share of the excitation energy taken up by the heavy fragment at scission. Another reason is the SL

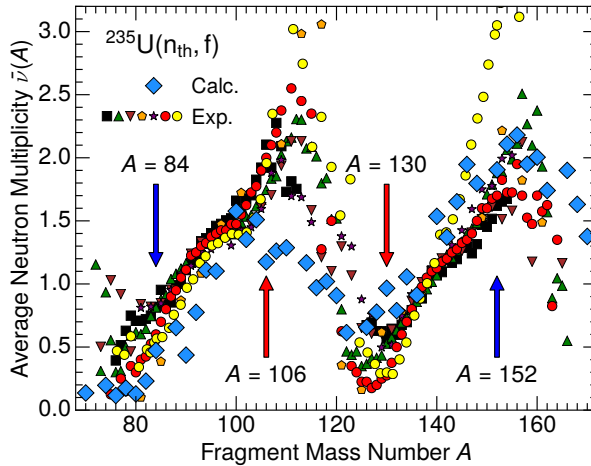


Figure 8.2: Calculated mean neutron multiplicity $\bar{\nu}(A)$ (blue diamonds) for $^{235}\text{U}(n_{\text{th}}, f)$ as a function of the mass number A of the primary fission fragment, which is compared to a variety of experimental data [106–111]. The red/blue arrows point to the mass divisions selected in Fig. 7.10. The figure is taken from Paper I.

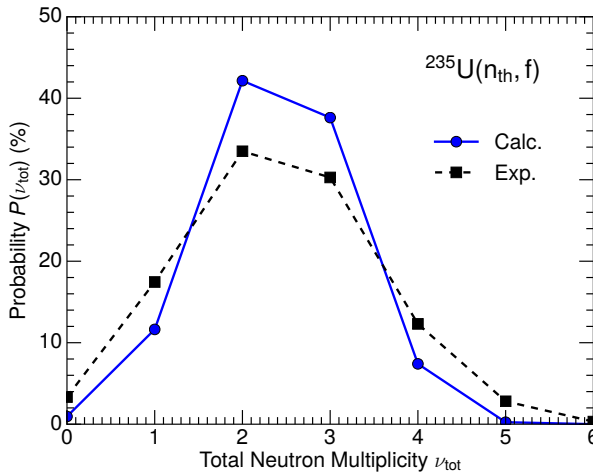


Figure 8.3: Calculated multiplicity distribution for total emitted neutrons ν_{tot} (solid line, blue circles) compared to experimental data [112] (dashed line, black squares) in $^{235}\text{U}(n_{\text{th}}, f)$. The figure is taken from Paper II.

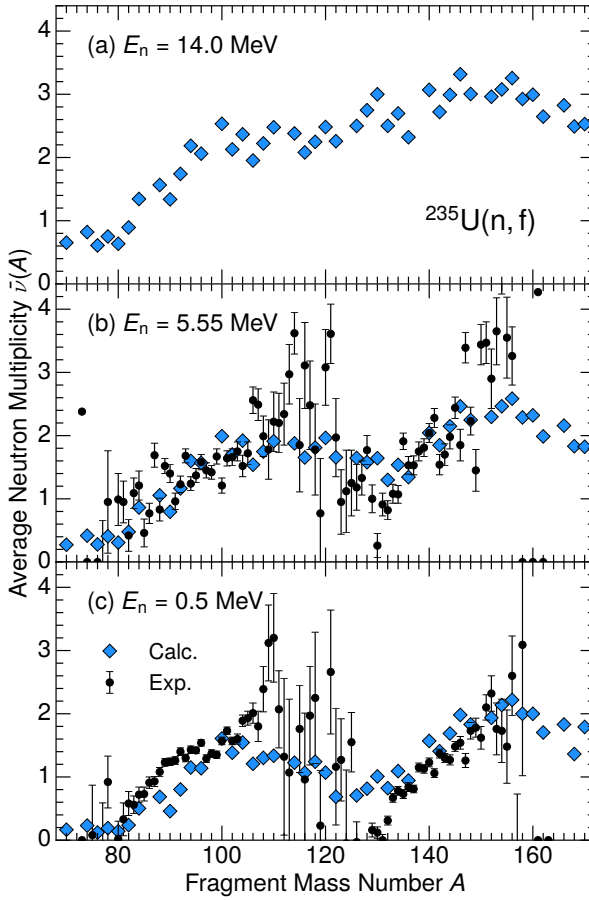


Figure 8.4: For $^{235}\text{U}(n, f)$ is shown the calculated mean neutron multiplicity as a function of the mass number of the primary fission fragment, $\bar{\nu}(A)$, for three different incident neutron energies E_n : 0.5 MeV (c), 5.55 MeV (b), 14 MeV (a). The experimental data from Ref. [88] are also shown. The figure is taken from Paper I.

mode entering the mass-asymmetric division at higher energies, resulting in large distortion energies for fragments $A \approx 130$, as seen in Fig. 7.12. On the contrary, the neutron multiplicity from the light fragments is affected less by the increase in energy.

Figure 8.5(a) shows average neutron multiplicity $\bar{\nu}(A)$ as a function of fragment mass number A in fission of ^{260}Fm for excitation energies $E_0^* = 0$ MeV, 6.13 MeV, and 15 MeV. For SF, low neutron multiplicity is obtained in the symmetric region because of the SS mode. When the energy is increased, the largest change is seen in the symmetric region where the decrease of the SS mode result in an increase in the excitation energy, and thus the number of neutrons emitted. There are no experimental data available for ^{260}Fm , but measurements have

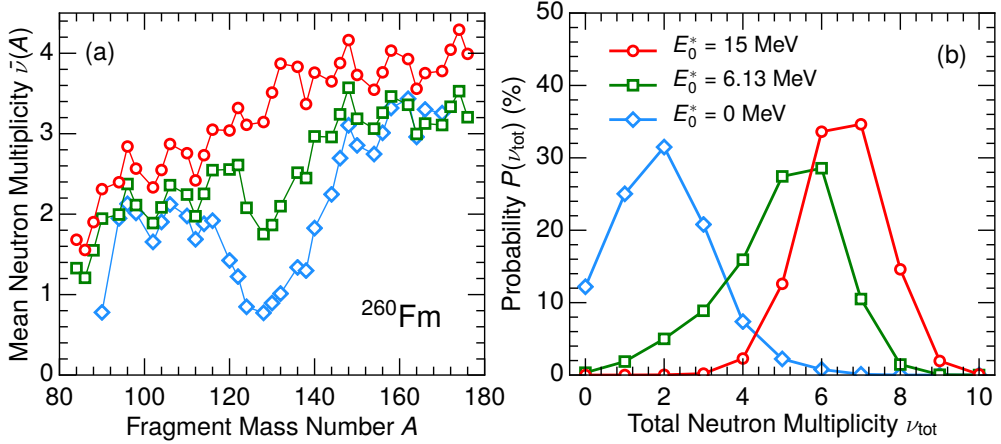


Figure 8.5: Calculated mean neutron multiplicity $\bar{\nu}(A)$ (a) and total neutron multiplicity distribution $P(\nu_{\text{tot}})$ (b) in fission of ^{260}Fm for initial excitation energies $E_0^* = 0$ (blue diamonds), 6.13 (green squares), 15 MeV (red circles).

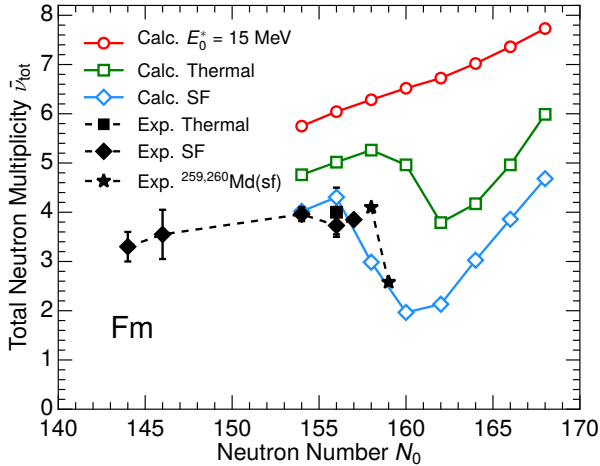


Figure 8.6: Average total neutron multiplicity $\bar{\nu}_{\text{tot}}$ from fission of fermium isotopes versus neutron number N_0 . For even $^{254-268}\text{Fm}$ theoretical results are shown as open symbols for SF (blue diamonds), thermal fission (green squares) and $E_0^* = 15$ MeV (red circles). Experimental data are shown as black diamonds (SF) [113–116] and black squares (thermal fission) [117]. The black stars show SF data for neighbouring nuclei $^{259,260}\text{Md}$ ($Z_0 = 101$, $N_0 = 158, 159$) taken from Refs. [97, 118]. The figure is taken from Paper VI.

been performed for SF of $^{260}_{101}\text{Md}_{159}$ in Ref. [97]. This nucleus fission primarily in the SS mode and differ only in one proton and neutron compared to $^{260}_{100}\text{Fm}_{160}$. The measured values of $\bar{\nu}(A)$ show large similarities with calculated results for $^{260}\text{Fm}(\text{SF})$ (see Fig. 10 in Ref. [97]).

Figure 8.5(b) shows the total neutron multiplicity distribution for ^{260}Fm for

excitation energies $E_0^* = 0$ MeV, 6.13 MeV, and 15 MeV. The calculated results for $E_0^* = 0$ MeV also agree well with the SF results in $^{260}_{101}\text{Md}$ (see Fig. 5 in Ref. [97]), where the average neutron multiplicity is measured to 2.58. It is also obtained in the calculations that there is a substantial probability for both fragments in $^{260}\text{Fm}(\text{SF})$ to emit no neutrons. This is referred to as cold fission since it correspond to fragments with very low excitation energy [119]. The calculated probability of zero neutrons for ^{260}Fm is 12%, while the corresponding measured probability in $^{260}_{101}\text{Md}_{159}(\text{SF})$ is about 9%.

The average total neutron multiplicity $\bar{\nu}_{\text{tot}}$ are shown in Fig. 8.6 for even $^{254-268}\text{Fm}$ versus the neutron number N_0 of the fissioning nucleus for three different excitation energies. Similarly to the calculated TKE values in Fig. 7.8, it also provides an experimental correspondence to the phase diagram in Fig. 6.10. Since the available energy either goes to TKE or excitation energy, the behaviour of the TKE as a function of N_0 in Fig. 7.8 is mirrored in the neutron multiplicities in Fig. 8.6. The SS mode with the compact scission shape of two spherical ^{132}Sn yields both low distortion energy as well as low intrinsic excitation energy, thus also low neutron multiplicity. Increasing the energy leads to a an increase of the St mode with a higher neutron multiplicity. The monotonic increase in neutron multiplicity versus N_0 comes mainly from the fact that higher neutron number of the fissioning nucleus results in more neutron-rich fragments with lower neutron-separation energies; each neutron therefore costs less to emit.

Figure 8.7(a) shows average neutron multiplicity $\bar{\nu}(A)$ as a function of fragment mass number A in ^{274}Hs for excitation energies $E_0^* = 0, 6.7,$ and 10 MeV.

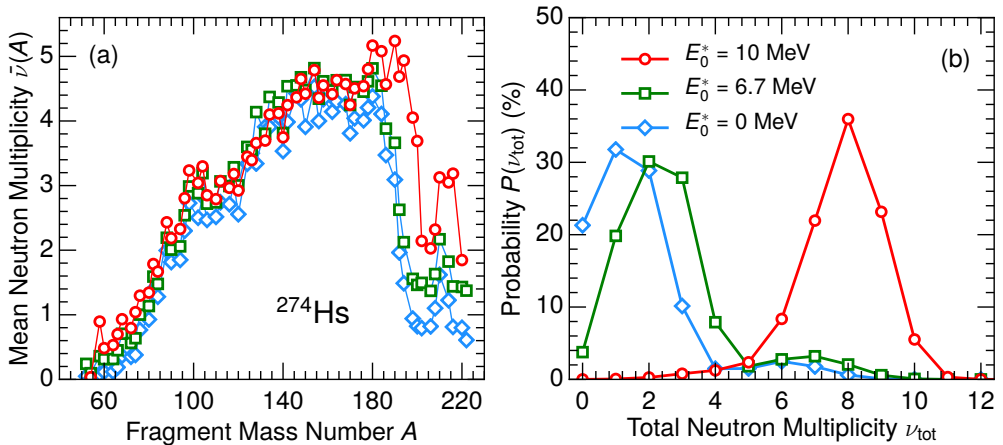


Figure 8.7: Calculated mean neutron multiplicity $\bar{\nu}(A)$ (a) and total neutron multiplicity distribution $P(\nu_{\text{tot}})$ (b) in fission of ^{274}Hs for initial excitation energies $E_0^* = 0$ (blue diamonds), 6.7 (green squares), 15 MeV (red circles).

All three curves show similar behaviour with low neutron multiplicities around $A_H \approx 208$. Results for the two lower energies, $E_0^* = 0$ MeV and $E_0^* = 6.7$, both exhibit the very asymmetric yield of the SA mode. The increase in energy from $E_0^* = 0$ MeV to $E_0^* = 6.7$ leads to an increase of number of neutrons from fragments $A_L \approx 66$ and $A_H \approx 208$ of about 0.3 and 0.7 neutrons, respectively. The total neutron multiplicity thus increases with roughly one neutron, as is also seen in the probability distribution in 8.7(b). On the other hand, for $E_0^* = 10$ MeV the most probable mass-split is symmetric, $A_L:A_H \approx 137:137$, with neutron multiplicities $\nu_L \approx \nu_H \approx 4$. The increase in energy of only 3.3 MeV thus results in a drastic change in the total neutron multiplicity from about 2.5 to 8. This is similar to the change of mode in the fermium isotopes. In this case however, increase in energy leads to a change from asymmetric to symmetric fission.

The general increase in $\bar{\nu}_{\text{tot}}$ with mass number A_0 comes mainly from the increase of the Q value as the mass of the fissioning nucleus increases. A simple estimate of the Q value can be obtained with the LDM formula in Eq. (2.7). The difference in binding energy only involves the surface and Coulomb terms, and if one assumes a symmetric mass-split, $A_L = A_H = A_0/2$, the following expression is obtained

$$Q = 0.37E_C - 0.26E_S \text{ MeV}, \quad (8.3)$$

where $E_C = 0.7103Z_0^2/A_0^{1/3}$ and $E_S = 17.80A_0^{2/3}$ are used for the Coulomb energy and surface energy of a spherical shape (in units of MeV), respectively [120]. If the nucleus is initially excited by the energy E_0^* , the total available energy is $Q^* = E_0^* + Q$. Subtracting Q^* by the TKE Viola systematics in Eq. (7.9) gives the following estimate of the TXE in the fragments

$$\text{TXE} = E_0^* + 0.1439 \cdot Z_0^2/A_0^{1/3} - 4.628 \cdot A_0^{2/3} - 7.3 \text{ MeV}. \quad (8.4)$$

This expression decreases for more neutron-rich nuclei, corresponding to less energy available for neutron emission. However, a more neutron-rich fissioning nucleus will have more neutron-rich fragments; each neutron will cost less to emit. Assuming simply a constant proton-to-mass ratio of $Z_0/A_0 = 0.39$ (corresponding to ^{236}U) and that each neutron costs 8 MeV to emit, one obtains the following simple expression for the average total neutron multiplicity

$$\bar{\nu}_{\text{tot}}(A_0, E_0^*) = E_0^*/8 + 0.00274 \cdot A_0^{5/3} - 0.5785 \cdot A_0^{2/3} - 0.9125. \quad (8.5)$$

Fig. 8.8 shows average total neutron multiplicity $\bar{\nu}_{\text{tot}}$ versus the mass number A_0 of the fissioning nucleus, where filled symbols correspond to experimental data for SF (diamonds) and thermal fission (squares). Calculations are shown as open symbols for SF (diamonds), thermal fission (squares), and $E_0^* = 15$

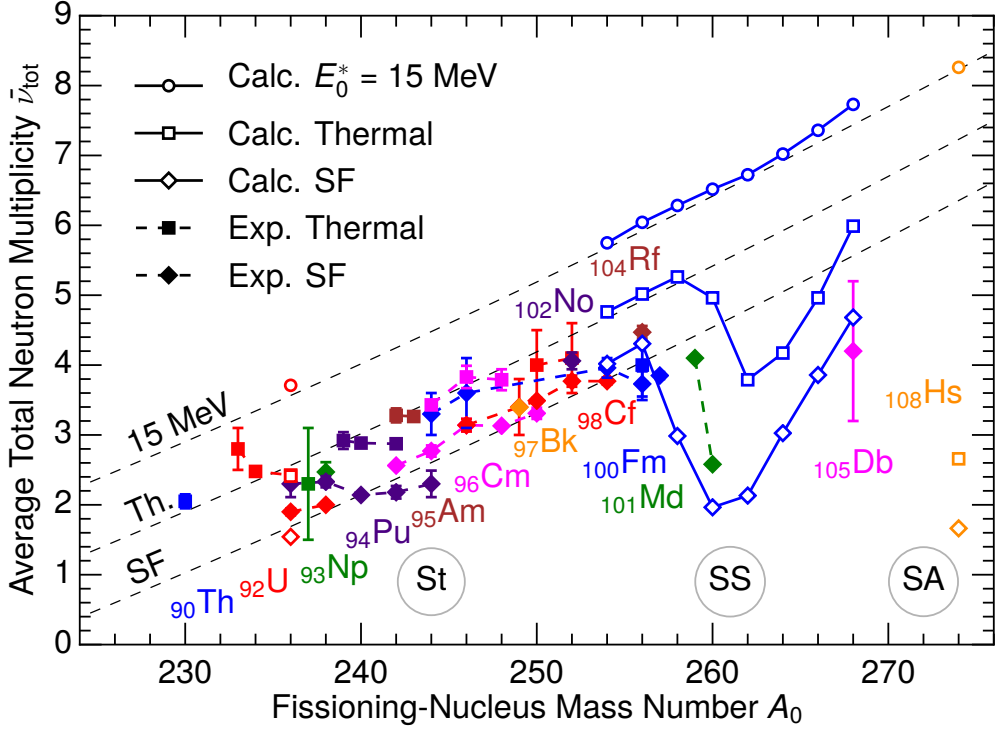


Figure 8.8: Total neutron multiplicity $\bar{\nu}_{\text{tot}}$ as function of the mass number A_0 of the fissioning nucleus. Filled symbols correspond to experimental data for SF (diamonds) and thermal fission (squares) from Refs. [97, 113–116, 118, 121–135]. Calculations are shown as open symbols for SF (diamonds), thermal fission (squares), and $E_0^* = 15$ MeV (circles) for fissioning nuclei ^{236}U , even $^{254-268}\text{Fm}$, and ^{274}Hs . Black dashed lines show the systematics with Eq. (8.5) for energies $E_0^* = 0, 7$ and 15 MeV. Regions where the St, SS and SA modes are present in calculations of low-energy fission are also indicated.

MeV (circles) for fissioning nuclei ^{236}U , even $^{254-268}\text{Fm}$, and ^{274}Hs . The three black dashed lines show the systematics with Eq. (8.5) for energies $E_0^* = 0, 7$ and 15 MeV. For SF, both data and calculations are described reasonably well by the $\bar{\nu}_{\text{tot}}$ -systematics curve up to $A_0 \approx 258$, where the appearance of the SS mode result in lower neutron multiplicities. Calculations for ^{274}Hs with low excitation energies also result in large deviations due to the compact SA mode. For a fissioning nucleus with an initial excitation energy E_0^* , the extra energy compared to SF generally goes to excitation energy of the fragments. The neutron multiplicity for thermal fission is then increased by about one neutron, corresponding to the black dashed curve in the middle. For $E_0^* = 15$ MeV, when the influences of both the SS mode and the SA mode have disappeared, calculations agree well with the systematic behaviour. This is reasonable since the simple expression was based on the LDM, which is assumed to be valid at higher energies when shell effects are negligible.

8.3 Correlations between neutron multiplicities and TKE

Since the Metropolis random-walk method is an event-by-event model, it can describe correlations between various quantities. One example is the correlation between number of neutrons emitted and the TKE of the fragments. This was recently measured by Gök et al. [136] and was studied in Paper V. A phenomenological deterministic model of prompt neutron emission was also recently applied to the same problem, yielding very good agreement with data [137].

Figure 8.9 shows the calculated average neutron multiplicity from the light and

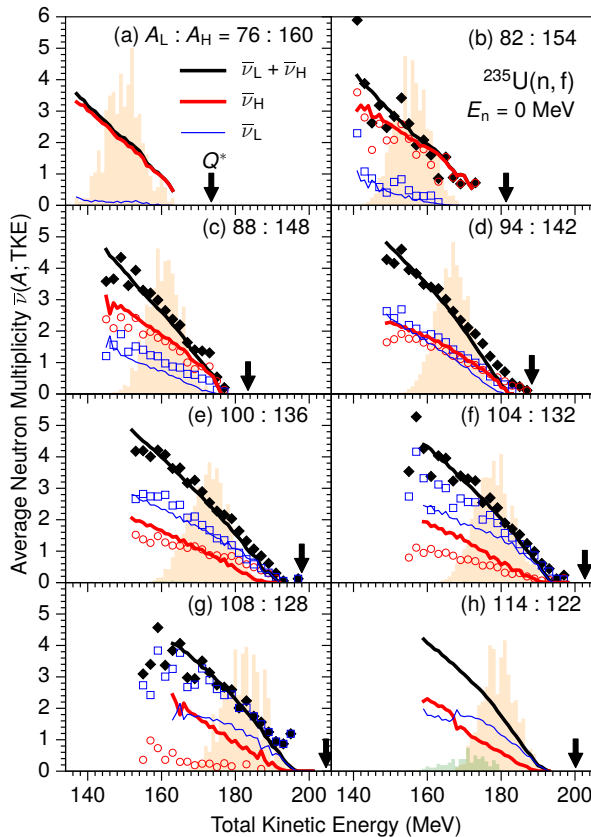


Figure 8.9: Average multiplicity of neutrons evaporated from the light or heavy fragment in $^{235}\text{U}(n_{\text{th}}, f)$ as a function of TKE, $\bar{\nu}_L(A, \text{TKE})$, and $\bar{\nu}_H(A, \text{TKE})$, for eight mass divisions. Calculated: $\bar{\nu}_L$ (thin blue lines), $\bar{\nu}_H$ (thick red lines), $\bar{\nu}_L + \bar{\nu}_H$ (black lines). Measured [136]: $\bar{\nu}_L$ (open blue squares), $\bar{\nu}_H$ (open red circles), $\bar{\nu}_L + \bar{\nu}_H$ (black squares). The histograms show the calculated TKE distributions, $P(\text{TKE})$, for the St mode (orange) and the SL mode (green). The arrows point to the Q^* values. The figure is taken from Paper V.

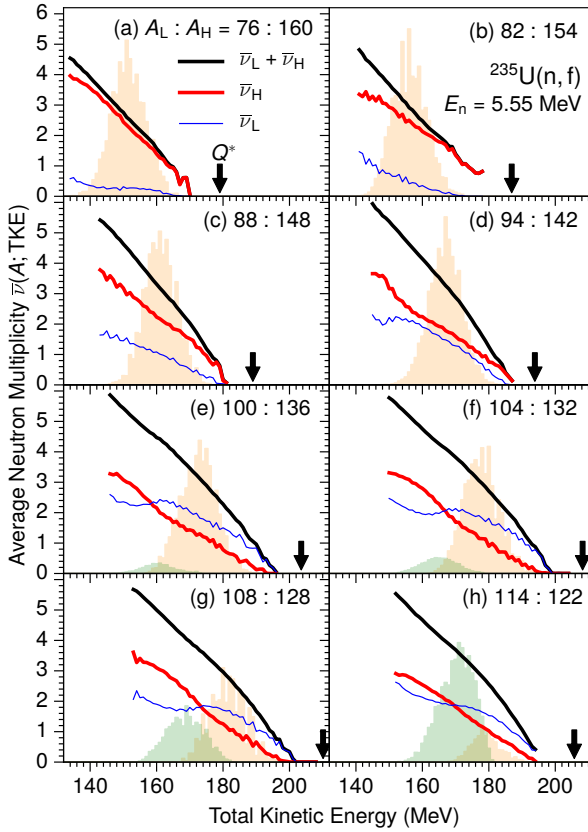


Figure 8.10: Same as Fig. 8.9 but for $E_n = 5.55$ MeV. The figure is taken from Paper V.

the heavy fragments for specified TKE, $\nu(A_L; \text{TKE})$ and $\nu(A_H; \text{TKE})$, as well as their sum, for eight mass divisions in $^{235}\text{U}(n_{\text{th}}, f)$. Also shown are the experimental results [136]. The calculated TKE distributions, $P(\text{TKE})$, are also shown for the St mode (orange) and the SL mode (green). The calculated multiplicities, $\bar{\nu}_L(\text{TKE})$ and $\bar{\nu}_H(\text{TKE})$, agree well with the measured values for asymmetric divisions, $A_H \geq 136$. For the more symmetric mass splits the calculations substantially overestimate the number of neutrons emitted from the heavy fragment, most severely for the mass split 108:128. This interval in fragment mass number coincides with that of the discrepancy found for the average TKE (see discussion in Sec. 7.2). For very asymmetric divisions the heavy fragment receives most of the excitation energy and, as a result, it contributes almost all of the neutrons. Closer to symmetry however, more neutrons are instead emitted from the light fragment.

Figure 8.10 shows the TKE-gated mean neutron multiplicity $\bar{\nu}(A; \text{TKE})$ for the same eight mass divisions as in Fig. 8.9, but for incident neutron energy $E_n = 5.55$ MeV. When the energy of the incoming neutron increases, the Q^* -value increases correspondingly by the same amount. We find that the average TKE changes very little and most of the additional energy goes to TXE. The four most asymmetric division, Figs. 8.10(a)-(c), is similar to the thermal result for both $\bar{\nu}_L$ and $\bar{\nu}_H$, except for an overall increase due to the increased excitation of the primary fission fragment. This smooth evolution with E_n may be contrasted with the behavior for the four least asymmetric divisions in Figs. 8.10(d)-(h), where qualitative changes are apparent. It is especially noticeable that $\bar{\nu}(A_L; \text{TKE})$ and $\bar{\nu}(A_H; \text{TKE})$ cross so the heavy fragment becomes dominant at low TKE, and the light fragment emits most neutrons at higher TKE. This is due to the appearance of the SL mode (green histograms) for more asymmetric mass splits at low TKE, as seen in Fig. 7.12. This prediction has yet to be tested experimentally.

Chapter 9

Fusion-quasifission dynamics

9.1 Introduction

The heaviest element occurring in Nature is plutonium with 94 protons. Heavier elements have however been synthesized in various reactions (see e.g. [138, 139]). The primary method for producing superheavy elements (SHE) with $Z \geq 104$ has been through heavy-ion fusion reactions. For relatively light colliding nuclei, reaching the Coulomb barrier means the shape configuration is inside the fission saddle point and leads automatically to the formation of the compound nucleus. However, for heavier nuclei at the Coulomb barrier the nucleus will find itself outside the fission saddle point, so for colliding energies close to the Coulomb barrier a compound nucleus is rarely formed [140, 141]. The composite nucleus can then diffuse over the inner saddle to the ground state, but also undergo a re-separation process, referred to as quasifission (QF). This results in a decrease in the production rate of SHE.

The production of a SHE in a fusion reaction therefore proceeds in three steps (see Fig. 9.1): (1) contact of the surfaces of the colliding nuclei, (2) formation of the fused nucleus by evolving to a compact shape, in competition with QF, (3) survival of the fused nucleus after cooling by neutron evaporation. The total cross section for the resulting evaporation residue is then given by the product of the three steps.

At present, both cold and hot fusion reactions have been used to produce SHE. In cold fusion with a ^{208}Pb target, the compound nucleus is formed with relatively low excitation energy so that the survival probability of the compound nucleus against fission in step (3) is maximized. On the other hand, in hot fusion with

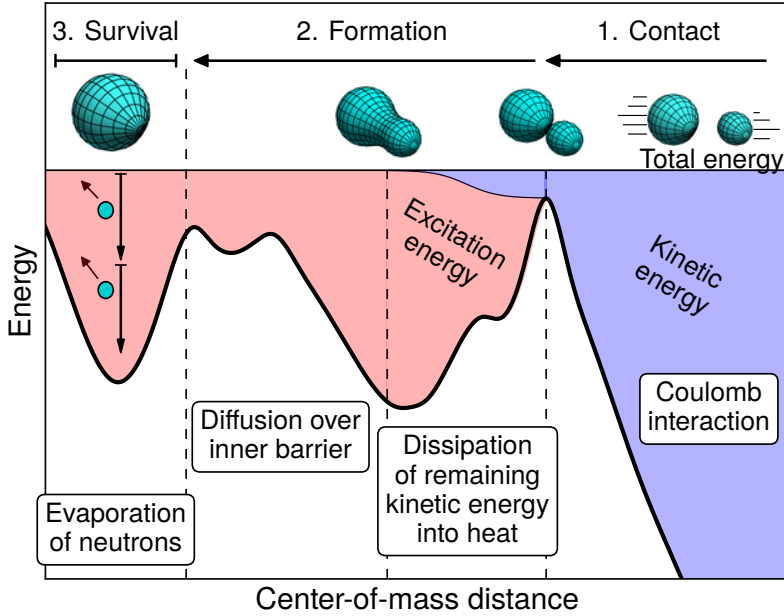


Figure 9.1: The three steps in the fusion process: (1) contact of the surfaces of the colliding nuclei, (2) formation of a compact compound nucleus, (3) survival of the compound nucleus against fission by neutron evaporation.

a ^{48}Ca target, the formation probability of the compound nucleus in step (2) is maximized instead.

In the present studies we only consider the compound-nucleus formation in step (2). The considered systems correspond to different projectiles on a ^{208}Pb -target typical in cold-fusion reactions, with main focus on the reaction $^{50}\text{Ti}+^{208}\text{Pb}$ resulting in compound nucleus ^{258}Rf .

9.2 Method

In the fusion-by-diffusion (FBD) model by Swiatecki et al. [142, 143], it is assumed that the composite system slips into a fission valley after reaching a contact configuration in step (1). It can then diffuse over the saddle to form a compound nucleus, which is described by solving the one-dimensional Smoluchowski equation. It accounts for experimental cross sections reasonably well, but it does not give any information regarding the shape evolution or the events leading to QF. As discussed in Ch. 5, the Smoluchowski equation emerges from the general Langevin description in the highly dissipative limit and can be approxim-

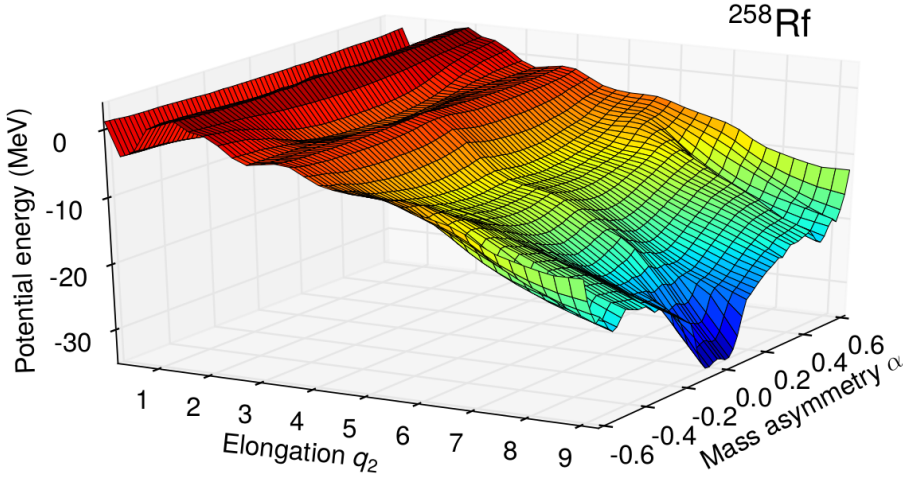


Figure 9.2: Potential energy for compound nucleus ^{258}Rf projected on the mass asymmetry α and elongation q_2 obtained by minimization with respect to the other shape coordinates. A valley in q_2 -direction is seen around the mass asymmetry $\alpha = 0.6$, corresponding to fusion with projectile ^{50}Ti and target ^{208}Pb .

ately simulated by means of a random walk on the associated multidimensional potential-energy surface $U(\chi)$.

Figure 9.2 shows the potential energy projected on the mass asymmetry α and elongation q_2 obtained by minimization with respect to the other shape coordinates for ^{258}Rf . A valley in the potential energy along q_2 is seen around the mass asymmetry $\alpha = 0.6$, corresponding to fusion with projectile ^{50}Ti and target ^{208}Pb .

It can however be misleading to simply minimize the potential energy, since the shape coordinates must also change gradually, and it is more suitable to analyze the potential energy using the immersion method discussed in Sec. 4.2. This method is used to obtain the curves in Fig. 9.3, which shows potential energy as a function of the quadrupole-moment parameter q_2 for compound nuclei ^{256}No (a), ^{258}Rf (b), ^{262}Sg (c), and ^{266}Hs (d) corresponding to reactions with a ^{208}Pb -target and projectiles ^{48}Ca , ^{50}Ti , ^{54}Cr , and ^{58}Fe , respectively. In addition to the mainly symmetric fission valley, there is an asymmetric valley which bears a strong resemblance to the target and projectile shapes, thus denoted as fusion valley. The well separated nuclei only interact via the Coulomb potential, giving rise to the smooth behaviour of the asymmetric valley for large q_2 (though in the 3QS parametrization the target and projectile are always connected with a non-zero neck). This smooth behaviour is extrapolated to smaller q_2 values by fixing the four other coordinates (red dashed line). However, when the nuclei

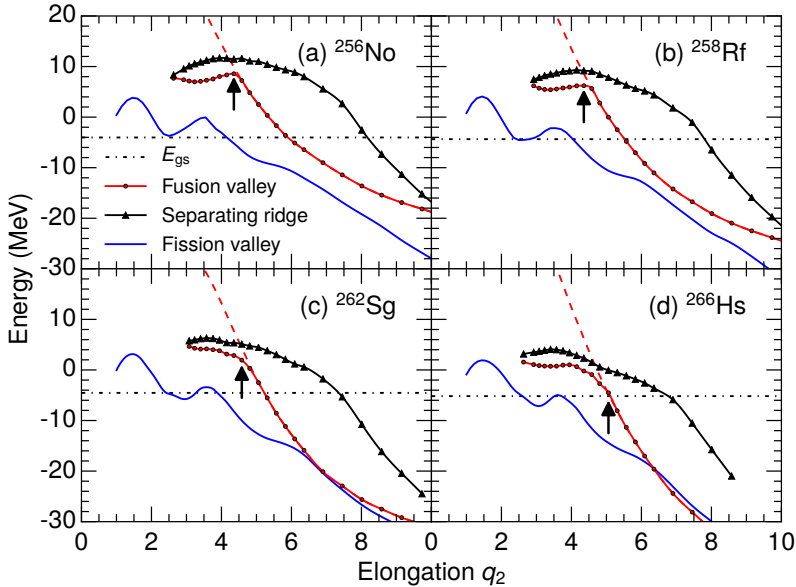


Figure 9.3: Potential energy as a function of elongation q_2 for compound nuclei (a) ^{256}No , (b) ^{258}Rf , (c) ^{262}Sg , (d) ^{266}Hs . The blue curves correspond to the minimum potential energy for the mainly symmetric fission valleys, while the red curves correspond to the asymmetric valleys. The Coulomb energies are shown as red dashed lines. The ridge between the two valleys is shown as a black curve with triangles. The arrows indicate the contact points $q_2^{(\text{cont})}$. The figure is taken from Paper VII.

come close to each other the nuclear interaction will start to have effect, and it will be more energetically favourable to develop a neck. This is called the contact point $q_2^{(\text{cont})}$ and is shown as black arrows in Fig. 9.3. While the ^{208}Pb -target is near spherical for all q_2 values in the asymmetric valley, the projectile changes from small deformation to about $\varepsilon_P \approx 0.4$ inside the contact point.

We assume that the colliding nuclei will slip into the asymmetric valley after overcoming the Coulomb barrier. The kinetic energy remaining at contact will quickly be dissipated into intrinsic excitation energy due to strong friction when the neck develops. The friction force is proportional to the velocity, $\vec{F}_{\text{fric}} = -\gamma\vec{v}$, where the friction coefficient can be estimated with the window friction formula [144]

$$\gamma \approx 16\pi c_{\text{neck}}^2 \text{ MeV/fm} \cdot c, \quad (9.1)$$

where c_{neck} is the neck radius of the compound nucleus. Figure 9.4(a) shows the value of the neck radius along the asymmetric valley for ^{258}Rf , where it is seen how the neck changes from a practically zero neck to a value around $c_{\text{neck}} \approx 3$ fm, corresponding to the contact point $q_2^{(\text{cont})}$. This rapid increase in neck radius is also in agreement with the “neck zip” discussed in the FBD model [142, 143]. The nuclear interaction implies a substantial lowering of the

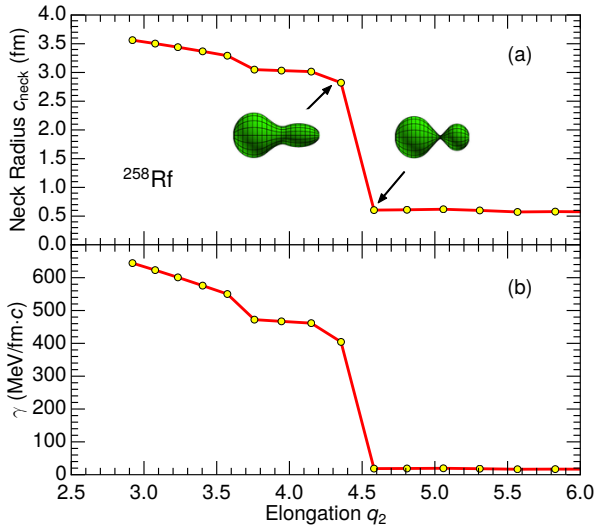


Figure 9.4: Neck radius c_{neck} (a) and the friction coefficient γ (b) as a function of elongation q_2 along the asymmetric valley for ^{258}Rf . Shapes of the system before and after contact are also shown. The figure is taken from Paper VII.

energy. The shapes before and after the contact are also shown in Fig. 9.4(a), where it is seen how the neck zip is associated with a dramatic shape change of the projectile from near spherical to a very large prolate deformation due to the onset of the short-range nuclear attraction.

The corresponding friction coefficient γ along the asymmetric valley is shown in Fig. 9.4(b). It is negligible before contact, whereas it increases to about $\gamma \approx 500$ MeV/fm \cdot c after the contact point, due to the neck zip.

Figure 9.5 shows the neck radius along the asymmetric fusion valley for all the four nuclei considered. The systems correspond to different projectiles, whereas the target is ^{208}Pb in all cases. The center-of-mass distance for the contact configuration of the target and projectile therefore increases for reactions with heavier projectiles. Correspondingly, the contact point where the neck develops corresponds to a larger q_2 for heavier systems.

The starting configuration for the diffusion over the inner saddle is expected to begin at a more compact shape when the kinetic energy of the colliding nuclei is increased. In a recent study [145] it was estimated that the starting elongation should be proportional to the velocity $\sqrt{E_{\text{cm}} - B_{\text{cont}}}$, where E_{cm} the kinetic energy of the colliding nuclei in the center-of-mass frame, and B_{cont} is the Coulomb barrier for reaching a contact configuration. This is in accordance

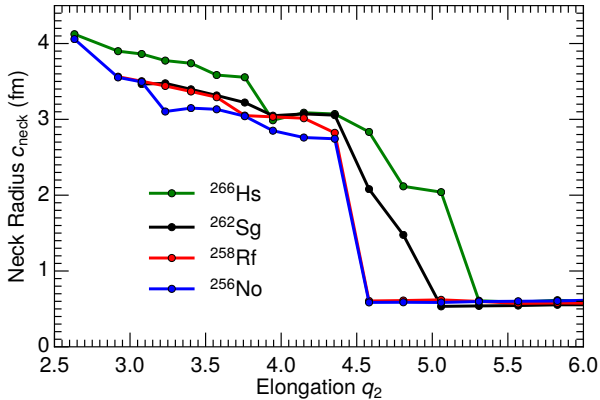


Figure 9.5: Neck radius c_{neck} as a function of elongation q_2 along the asymmetric fusion valley for compound nuclei ^{256}No , ^{258}Rf , ^{262}Sg , and ^{266}Hs . The figure is taken from Paper VII.

with the assumption of a strong, constant friction. Here, we employ a simple expression for the starting value of $q_2^{(\text{st})}$ based on a similar energy dependence,

$$q_2^{(\text{st})}(E_{\text{CN}}^*) = q_2^{(\text{cont})} - d\sqrt{E_{\text{CN}}^* - E_0}, \quad (9.2)$$

where $E_0 = U(\chi^{(\text{cont})}) - E_{\text{gs}}$, and where we adopt the value $d = 0.27 \text{ MeV}^{-1/2}$. The other four shape coordinates are then determined by the asymmetric valley to form the starting point $\chi^{(\text{st})}$.

From the starting point $\chi^{(\text{st})}$, the system can diffuse across the inner saddle to form a compound nucleus. The shape changes are selected by the Metropolis method using the effective level density described in Sec. 3.1.2. The excitation energy E_{CN}^* of the compound nucleus is given by

$$E_{\text{CN}}^* = E_{\text{cm}} + Q, \quad (9.3)$$

where

$$Q = (M_{\text{P}} + M_{\text{T}} - M_{\text{CN}})c^2, \quad (9.4)$$

and where M_{CN} , M_{P} , and M_{T} are the masses of the compound nucleus, the projectile nucleus, and the target nucleus, respectively. The masses are calculated within the same macroscopic-microscopic model that is used to obtain the potential-energy surfaces.

The walks are stopped and binned as a fusion event if it evolves inside the inner saddle point (located at $q_2 \approx 1.5$, see Fig. 9.3). This defines a formation of the compound nucleus in our model. The walks can also lead to QF, which in the model is defined when the neck radius becomes smaller than $c_{\text{sc}} = 1.5 \text{ fm}$, as in

the fission calculations. Then the walk is stopped and binned as a QF event. The fusion probability P_{form} is then obtained as the number of fusion events divided by the total number of events, i.e.

$$P_{\text{form}} = \frac{\text{Number of fusion events}}{\text{Total number of events}}, \quad (9.5)$$

where the total number of events correspond to the 10^5 walks performed.

The QF mass yield $Y_{\text{QF}}(A)$ is defined as the percentage of QF events resulting in fragment-mass number A . The yield is normalized to 200% because each QF event results in two fragments. The proton and neutron numbers, Z and N , are determined by requiring the same Z/N ratio as for the compound nucleus. In the present study only fragments with even Z and N are considered. Calculation of the total kinetic energy (TKE_{QF}) of QF fragments is performed as specified for fission in Sec. 7.1. In this case however, the total available energy is given by the initial kinetic energy E_{cm} of the projectile and the target nuclei, which in QF is shared between the TKE_{QF} and the total excitation energy (TXE_{QF}) of the QF fragments

$$E_{\text{cm}} = \text{TKE}_{\text{QF}} + \text{TXE}_{\text{QF}}. \quad (9.6)$$

9.3 Simulations

Figure 9.6 shows for ^{258}Rf with energy $E_{\text{CN}}^* = 12$ MeV, the total number of visits to sites with a given combination of asymmetry α and elongation q_2 for walks leading to fusion (a) and to QF (b). The calculated probabilities of fusion and QF for this energy are 8% and 92%, respectively. The starting point for the walks is determined from Eq. (9.2) and is marked as a black circle. For this energy, it is not possible to pass the ridge to the fission valley until $q_2 \approx 3$. The majority of the walks leading to QF therefore keep the mass asymmetry as the initial projectile-target system. A large number of visits are spent around $q_2 \approx 3.5$ due to a minor local minimum in the asymmetric valley as seen in Fig. 9.3(b). Once the walk passes this minimum, the ridge to the fission valley disappears. The fusion walks then approach smaller values of the mass asymmetry towards the fission valley as seen in Fig. 9.6(a), until the inner saddle is crossed ($q_2 \approx 1.5$). However, a few walks that pass this point go out again corresponding to more symmetric QF mass splits.

Figures 9.6(c) and (d) is similar to Fig. 9.6(a) and (b), but for excitation energy $E_{\text{CN}}^* = 30$ MeV. The calculated probabilities of fusion and QF in this case are 25% and 75%, respectively. The increase in fusion probability comes primarily

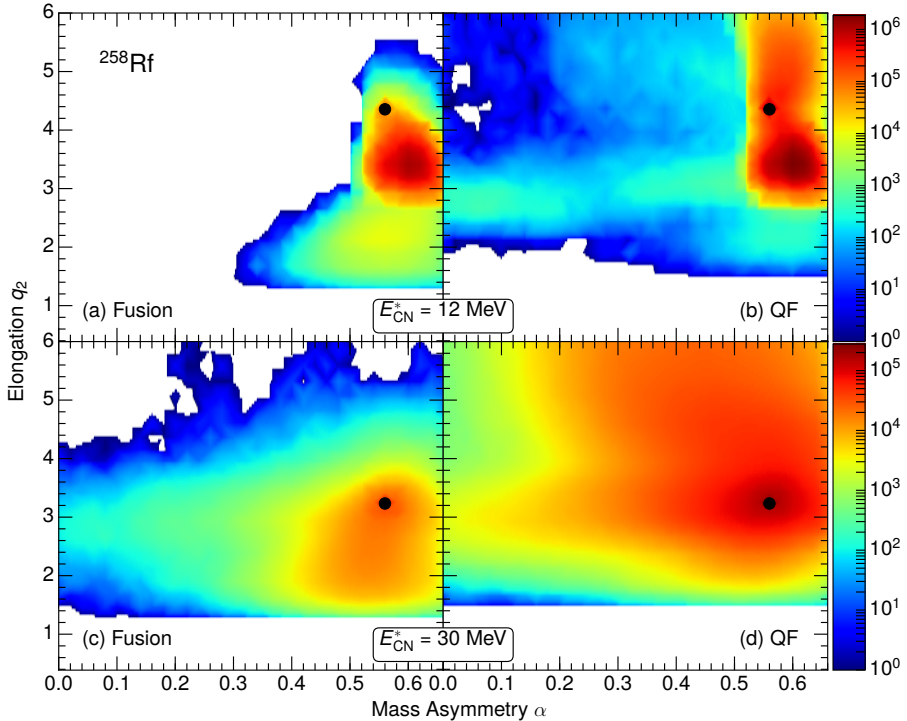


Figure 9.6: Number of visits to grid points with a given combination of asymmetry α and elongation q_2 for ^{258}Rf . For $E_{\text{CN}}^* = 12$ MeV, tracks are shown resulting in: (a) fusion (8 %) and (b) QF (92 %). For $E_{\text{CN}}^* = 30$ MeV, tracks are shown resulting in: (c) fusion (25 %). (d) QF (75 %). Circles mark the starting point. The inner saddle point is located at $q_2 \approx 1.5$. The figure is taken from Paper VII.

from the more compact starting point, and thus fewer steps are needed to pass the inner saddle. For this energy it is possible to cross the ridge to the fission valley already at the starting point. Trajectories leading to fusion, as well as QF, can therefore explore a wider range of shapes.

The formation probabilities of 8% and 25% for the energies $E_{\text{CN}}^* = 12$ MeV and 30 MeV compare reasonably well with the data for the reaction $^{50}\text{Ti} + ^{208}\text{Pb}$ presented in Ref. [146], where the values 2% and 19% were reported for energies $E_{\text{CN}}^* = 14.2$ MeV and $E_{\text{CN}}^* = 32.7$ MeV, respectively.

Figure 9.7 shows contour plots of the number of QF events in $^{50}\text{Ti} + ^{208}\text{Pb}$ with respect to fragment mass number A and TKE_{QF} for the two energies $E_{\text{CN}}^* = 12$ MeV (a) and $E_{\text{CN}}^* = 30$ MeV (b). For the lower energy it is seen that the majority of the events correspond to mass numbers in a rather small region around projectile and target mass numbers, whereas the values of TKE_{QF} varies quite a lot from around 120 MeV to 200 MeV. The mass peak obtained in the calculations is located at $A_{\text{H}} \approx 204$ with an average value of $\text{TKE}_{\text{QF}} \approx 166$ MeV.

Measurements for this reaction with energy near the Coulomb barrier show that the majority of the QF correspond to asymmetric mass-splits $A_L:A_H \approx 50:208$, but with an average TKE_{QF} -value of roughly 200 MeV (Fig. 23(a) in Ref. [147]). This difference in TKE_{QF} indicates that the QF fragments should be somewhat more compact than what is obtained in the calculations. It might be that the strong shell effects of ^{208}Pb in the SA fission mode is not as present as for other SHE, e.g. in fission of ^{274}Hs where higher TKE is obtained in the SA mode (see Fig. 7.9). Compared to ^{258}Rf , the N/Z ratio of ^{274}Hs is somewhat closer to the ratio of ^{208}Pb . The N/Z degree of freedom of fragments may then play a role.

As discussed earlier, the amount of symmetric QF events increases when the energy is increased, which is also seen in Fig. 9.7(b). It is in Ref. [148] discussed that the average TKE_{QF} of excited nuclei ($E_{\text{CN}}^* > 40$ MeV) has a parabolic dependence on the fragment mass and independent of the excitation energy. This correspond to when the shell effects have disappeared and is well described by the LDM with symmetric Gaussian-like shape mass and energy distributions.

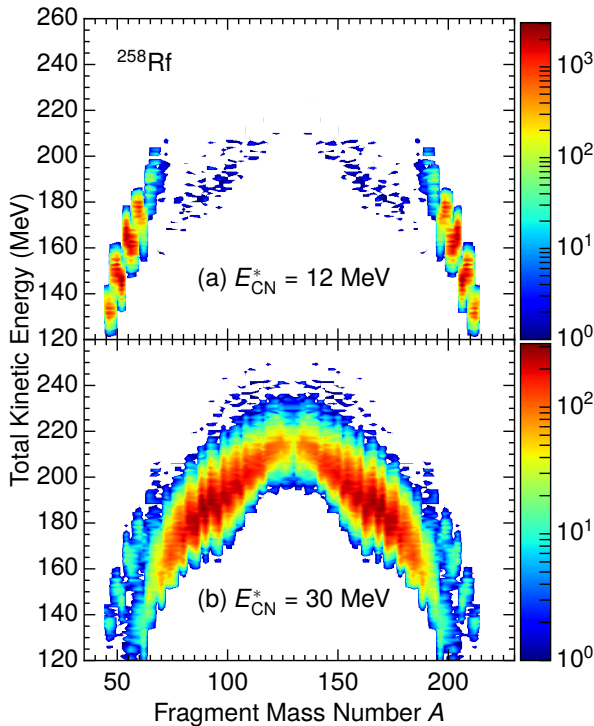


Figure 9.7: Calculated number of QF events vs. $(A, \text{TKE}_{\text{QF}})$ (log-scale) in the reaction $^{50}\text{Ti} + ^{208}\text{Pb} \rightarrow ^{258}\text{Rf}$ for compound-nucleus excitation energy $E_{\text{CN}}^* = 12$ MeV (a) and $E_{\text{CN}}^* = 30$ MeV (b). The figure is taken from Paper VII.

This parabolic behaviour is also similar to the calculated results in Fig. 9.7(b).

The obtained results in this first study compare reasonably well with the data for the reaction with projectile ^{50}Ti and target ^{208}Pb . It would be interesting to apply the method to other ^{208}Pb -reactions, as well as to hot-fusion reactions with a ^{40}Ca -target. These investigations might give new insights into the dynamics of formation process in fusion, as well as a way to further test the model for the description of fusion.

Chapter 10

Outlook

The fission process seems to be reasonably well described in the Metropolis random-walk model, which is based on the assumption of overdamped shape evolution. This assumption is also supported by recent time-dependent density functional calculations [62–64].

The event-by-event nature of the random-walk model allows for correlation studies, where correlations between TKE and neutron multiplicity were calculated in the present studies. Another example of a correlation study would be to investigate the energy spectrum of evaporated neutrons from fragments with specified mass number and TKE. For cases with TKE close to the maximum possible values, corresponding to very low excitation energy, there are few energy levels to decay to in the resulting daughter nucleus, and microscopic structure effects are more prominent. While this is possible to study theoretically, this can however be more challenging to perform experimentally.

The results in the symmetric fission region for $^{235}\text{U}(n, f)$ are less accurate in our present calculations because the scission configurations encountered for near-symmetric divisions are insufficiently elongated and hence lead to too large TKE values. This may be due to limitations in the employed 3QS shape parametrization. Other models of the fission process, such as those employed in Refs. [62, 63, 149, 150] suggest larger distortions of the fragments than what is obtained in the present treatment. In particular octupole deformations of the fragments have been argued to be important [149].

For an excited nucleus it is energetically possible to emit one or more neutrons before fissioning or gamma-deexcite to the ground state. After emitting one or more neutrons, it might still be energetically possible for a resulting daughter

nucleus to undergo fission. This is called 2nd-chance fission and becomes increasingly more probable with excitation energy. This can be included in the present model. The competition between fission and neutron emission is in the transition-state theory [151] determined by the level density at the fission saddle point and the level density in the daughter nucleus after neutron emission. The 2nd-chance fission probabilities, as well as higher n -chance probabilities, can be calculated with the microscopic combinatorial level density method. Fission-fragment distributions for an arbitrary energy would then be obtained by performing random-walks for the initial nucleus (Z_0, N_0) (1st-chance fission) and the daughter nuclei; $(Z_0, N_0 - 1)$ (2nd-chance fission), $(Z_0, N_0 - 2)$ (3rd-chance fission) etc. The total fragment distributions are then obtained by averaging the n -chance distributions with the associated probabilities. Multi-chance fission calculations with the random-walk model was performed in Ref. [84], using another method for obtaining the probabilities. The method was shown to yield good agreement with data for charge yields.

Since the random-walk model is based on the classical Langevin formalism, it cannot describe tunneling phenomena. The introduced ΔE -method for simulating SF seems to give reasonable results, except for ^{258}Fm where a WKB tunneling calculation is needed. A more proper description would include dynamical aspects of the simulation, which is challenging.

In the present studies, only even-even fragments with the same proton-to-neutron ratio Z/N as the fissioning nucleus is considered. An extension of the random-walk model including a proton-neutron asymmetry degree of freedom was developed in Ref. [85]. This allows for descriptions of odd-even staggering seen in fragment charge yields. It also allows for calculations of isotopic fragment distributions, which was studied in Ref. [86]. Another method for calculating charge yields was introduced in Ref. [67], using particle number projection. Inclusion of the Z/N degree of freedom of fragments in the calculations of TKE and neutron emission might give new insights into the properties of fission fragments.

About half of the elements heavier than iron is believed to have been produced in a reaction called the r -process [152], which is a succession of rapid neutron captures, eventually ending in fission. Thus, fragment distributions and the number of emitted neutrons from these fragments influence calculations of the final abundances. Since most nuclei relevant in the r -process are very exotic and neutron-rich, where experimental data is scarce, the estimated abundance distribution remains rather uncertain. The random-walk model appears to be suitable for such calculations since it has shown predictive power regarding mass yields, and give reasonable agreement with data for TKE and neutron multiplicities.

The obtained fusion results in this first study compare reasonably well the data for the reaction with projectile ^{50}Ti and target ^{208}Pb . However, the high TKE value in QF for the very asymmetric split seen in measurement is not obtained in the calculations. This indicates that the scission configurations are too elongated. The N/Z degree of freedom of fragments may play a role for this. It would also be interesting to apply the method to other ^{208}Pb -reactions, as well as to hot-fusion reactions with a ^{40}Ca -target. These investigations might give new insights into the dynamics of formation process in fusion, as well as a way to further test the model for the description of fusion. The survival probability in the last step in the fusion process corresponds to evaporation of neutrons in competition with fission. These types of calculations are identical with those regarding multi-chance fission, and could similarly be calculated with the microscopic combinatorial level densities.

References

- [1] B. Russell, *History of western philosophy*, Routledge, London (2004).
- [2] H. Becquerel, C.R. Acad. Sci. **122**, 1086 (1896).
- [3] J.J. Thomson, Phil. Mag. **44**, 293 (1897); Nature **55**, 453 (1897).
- [4] E. Rutherford, Phil. Mag. **21**, 669 (1911).
- [5] J. Chadwick, Nature **129**, 312 (1932).
- [6] E. Fermi, Nature **133**, 483 (1934).
- [7] I. Noddack, Angew. Chem. **47**, 653 (1934).
- [8] O. Hahn and F. Strassmann, Naturwiss. **27**, 11 (1939).
- [9] L. Meitner and O. R. Frisch, Nature **143**, 239 (1939).
- [10] O.R. Frisch, Nature **143**, 276 (1939).
- [11] R. Rhodes, *The making of the atomic bomb*, Simon & Schuster, N.Y. (1986).
- [12] H. Yukawa, Proc. Phys.-Math. Soc. Jpn. **17**, 48 (1935).
- [13] M. Gell-Mann, Phys. Lett. **8**, 214 (1964).
- [14] G. Zweig, Report No. CERN-TH-401 (1964).
- [15] H. Hergert, Frontiers in Physics **8**, 379 (2020).
- [16] M. Mayer, Phys. Rev. **75**, 1969 (1949).
- [17] M. Goppert Mayer and H. Jensen, *Elementary theory of nuclear shell structure*, (New York: Wiley, 1955).

- [18] S. G. Nilsson, Kgl. Danske Videnskab. Selskab. Mat.-Fys. Medd. **29**:No. 16 (1955).
- [19] P. Ring and P. Schuck, *The Nuclear Many-Body Problem*, Springer-Verlag, New York (1980).
- [20] M. Wang, G. Audi, F.G. Kondev, W.J. Huang, S. Naimi, X. Xu, Chin. Phys. C **41**, 030003 (2017).
- [21] G. Audi, F.G. Kondev, M. Wang, W.J. Huang, and S. Naimi, Chin. Phys. C **41**, 030001 (2017).
- [22] J. Randrup and P. Möller, Phys. Rev. Lett. **106**, 132503 (2011).
- [23] D.E. Ward, B.G. Carlsson, T. Døssing, P. Möller, J. Randrup, and S. Åberg, Phys. Rev. C **95**, 024618 (2017).
- [24] J.R. Nix, Nucl. Phys. A **130**, 241 (1969).
- [25] P. Möller and J. R. Nix, Nucl. Phys. A **361**, 117 (1981).
- [26] P. Möller and J. R. Nix, Atomic Data Nucl. Data Tables **26**, 165 (1981).
- [27] P. Möller, A.J. Sierk, T. Ichikawa, and H. Sagawa, ATOMIC DATA AND NUCLEAR DATA TABLES **109–110**, 1 (2016).
- [28] C.F. von Weizsäcker, Z. Phys. **96**, 431 (1935).
- [29] H. A. Bethe and R. F. Bacher, Rev. Mod. Phys. **8**, 82 (1936).
- [30] N. Bohr and J. A. Wheeler, Phys. Rev. **56**, 426 (1939).
- [31] M. Wang, G. Audi, A. H. Wapstra, F. G. Kondev, M. MacCormick, X. Xu, and B. Pfeiffer, Chin. Phys. C **36**, 1603 (2012).
- [32] V.M. Strutinsky, Nucl. Phys. A **95**, 420 (1967).
- [33] V.M. Strutinsky, Nucl. Phys. A **122**, 1 (1968).
- [34] H.J. Lipkin, Ann. Phys. (N.Y.) **9**, 272 (1960).
- [35] Y. Nogami, Phys. Rev. **134**, B313 (1964).
- [36] H.C. Pradhan, Y. Nogami, and J. Law, Nucl. Phys. A **201**, 357 (1973).
- [37] P. Möller and J. R. Nix, Nucl. Phys. A **536**, 20 (1992).
- [38] H.A. Bethe, Phys. Rev. **50**, 332 (1936).

- [39] A. Bohr and B.R. Mottelson, *Nuclear Structure, volume I*, Benjamin, Reading, MA, 1969, Appendix 2B.
- [40] H. Uhrenholt, S. Åberg, A. Dobrowolski, Th. Døssing, T. Ichikawa, and P. Möller, *Nucl. Phys. A* **913**, 127 (2013).
- [41] A. V. Ignatyuk, K. K. Istekov, and G. N. Smirenkin, *Yad. Fiz.* **29**, 875 (1979) [*Sov. J. Nucl. Phys.* **29**, 450 (1979)].
- [42] J. Randrup and P. Möller, *Phys. Rev. C* **88**, 064606 (2013).
- [43] R. Bengtsson and S. Åberg, *Phys. Lett. B* **172**, 277 (1986).
- [44] N. Schunck and L.M. Robledo, *Rep. Prog. Phys.* **79**, 116301 (2016).
- [45] P. Möller, A.J. Sierk, T. Ichikawa, A. Iwamoto, and M. Mumpower, *Phys. Rev. C* **91**, 024310 (2015).
- [46] P. Möller and J. R. Nix, *Proc. Third IAEA Symp. on the physics and chemistry of fission, Rochester, 1973, vol. I (IAEA, Vienna, 1974)* p. 103.
- [47] P. Möller, D.G. Madland, A.J. Sierk, and A. Iwamoto, *Nature* **409**, 785 (2001).
- [48] P. Möller, A.J. Sierk, and A. Iwamoto, *Phys. Rev. Lett.* **92**, 072501 (2004).
- [49] T. Ichikawa, A. Iwamoto, and P. Möller, *Phys. Rev. C* **79**, 014305 (2009).
- [50] P. Möller, A.J. Sierk, T. Ichikawa, A. Iwamoto, R. Bengtsson, H. Uhrenholt, and S. Åberg, *Phys. Rev. C* **79**, 064304 (2009).
- [51] T. Ichikawa, A. Iwamoto, P. Möller, and A.J. Sierk, *Phys. Rev. C*, **86**, 024610 (2012).
- [52] T. Ichikawa and P. Möller, *Phys. Lett. B* **789**, 679 (2019).
- [53] A. Turkevich and J.B. Niday, *Phys. Rev.* **84**, 52 (1951).
- [54] U. Brosa, S. Grossman, and A. Müller, *Phys. Rep.* **197**, 167 (1990).
- [55] B.D. Wilkins, E.P. Steinberg, and R.R. Chasman, *Phys. Rev. C* **14**, 1832 (1976).
- [56] E.K. Hulet, J.F. Wild, J. Dougan, R.W. Lougheed, J.H. Landrum, A.D. Dougan, P.A. Baisden, C.M. Henderson, R.J. Dupzyk, R.L. Hahn, M. Schädel, K. Sümmerer, G.R. Bethune, *Phys. Rev. C* **40**, 770 (1989).

- [57] T. Ichikawa, A. Iwamoto, P. Möller, and A.J. Sierk, *Phys. Rev. C* **71**, 044608 (2005).
- [58] A.J. Sierk, *Phys. Rev. C* **96**, 034603 (2017).
- [59] M.D. Usang, F.A. Ivanyuk, C. Ishizuka, and S. Chiba, *Sci. Rep.* **9**, 1525 (2019).
- [60] J. Randrup, S.E. Larsson, P. Möller, S.G. Nilsson, K. Pomorski, and A. Sobiczewski, *Phys. Rev. C* **13**, 229 (1976).
- [61] P. Möller and J.R. Nix, *J. Phys. G* **20**, 1681 (1994).
- [62] A. Bulgac, P. Magierski, K. J. Roche, and I. Stetcu, *Phys. Rev. Lett.* **116**, 122504 (2016).
- [63] A. Bulgac, S. Jin, and I. Stetcu, *Phys. Rev. C* **100**, 014615 (2019).
- [64] A. Bulgac, S. Jin, K.J. Roche, N. Schunk, and I. Stetcu, *Phys. Rev. C* **100**, 034615 (2019).
- [65] Y. Tanimura, D. Lacroix, and G. Scamps, *Phys. Rev. C* **92**, 034601 (2015).
- [66] J. Randrup, P. Möller, and A.J. Sierk, *Phys. Rev. C* **84**, 034613 (2011).
- [67] M. Verriere and M.R. Mumpower, *Phys. Rev. C* **103**, 034617 (2021).
- [68] N. Fröman and P. O. Fröman, *JWKB Approximation* (North-Holland, Amsterdam, 1965) chap. 9, sect. 1, pp. 92–97.
- [69] J.E. Gindler, and K.F. Flynn, and L.E. Glendenin, and R.K. Sjoblom, *Phys. Rev. C* **16**, 1483 (1977).
- [70] K.F. Flynn, E.P. Horwitz, C.A.A. Bloomquist, R.F. Barnes, R.K. Sjoblom, P.R. Fields, and L.E. Glendenin, *Phys. Rev. C* **5**, 1725 (1972).
- [71] K.F. Flynn, J.E. Gindler, and L.E. Glendenin, *Phys. Rev. C* **12**, 1478 (1975).
- [72] D.C. Hoffman, J.B. Wilhelmy, J. Weber, W.R. Daniels, E.K. Hulet, R.W. Loughheed, J.H. Landrum, J.F. Wild, and R.J. Dupzyk, *Phys. Rev. C* **21**, 972 (1980).
- [73] W. John, E.K. Hulet, R.W. Loughheed, and J.J. Wesolowski, *Phys. Rev. Lett.* **27**, 45 (1971).

- [74] K.-H. Schmidt, S. Steinhäuser, C. Böckstiegel, A. Grewe, A. Heinz, A.R. Junghans, J. Benlliure, H.-G. Clerc, M. de Jong, J. Müller, M. Pfützner, and B. Voss, Nucl. Phys. A **665**, 221 (2000).
- [75] P. Möller and J. Randrup, Phys. Rev. C **91**, 044316 (2015).
- [76] A.N. Andreyev, J. Elseviers, M. Huyse, P. Van Duppen, S. Antalic, A. Barzakh, N. Bree, T.E. Cocolios, V.F. Comas, J. Diriken, D. Fedorov, V. Fedosseev, S. Franchoo, J.A. Heredia, O. Ivanov, U. Köster, B.A. Marsh, K. Nishio, R.D. Page, N. Patronis, M. Seliverstov, I. Tsekhanovich, P. Van den Bergh, J. Van De Walle, M. Venhart, S. Vermote, M. Veselsky, C. Wagemans, T. Ichikawa, A. Iwamoto, P. Möller, and A.J. Sierk, Phys. Rev. Lett. **105**, 252502 (2010).
- [77] M. Warda, A. Zdeb and L.M. Robledo, Phys. Rev. C **98**, 041602 (R) (2018).
- [78] Z. Matheson, S.A. Giuliani, W. Nazarewicz, J. Sadhukhan, and N. Schunck, Phys. Rev. C **99**, 041304 (2019).
- [79] G. Scamps and C. Simenel, arXiv:1904.01275v2 (2019).
- [80] N. Carjan, F.A. Ivanyuk, and Yu.Ts. Oganessian, Phys. Rev. C **99**, 064606 (2019).
- [81] C. Ishizuka, X. Zhang, M. D. Usang, F. A. Ivanyuk, and S. Chiba, Phys. Rev. C **101**, 011601(R) (2020).
- [82] P. Möller, J. Randrup, and A.J. Sierk, Phys. Rev. C **85** (2012) 024306.
- [83] P. Möller, J. Randrup, A. Iwamoto, and T. Ichikawa, Phys. Rev. C **90** (2014) 014601.
- [84] P. Möller and C. Schmitt, Eur. Phys. J. A **53**, 7 (2017).
- [85] P. Möller and T. Ichikawa, Eur. Phys. J. A **51**, 173 (2015).
- [86] C. Schmitt and P. Möller, Phys. Lett. B **812**, 136017 (2021).
- [87] A. Al-Adili, Ph.D. thesis, Uppsala University, 2013, p. 51; A. Oberstedt (private communication).
- [88] R. Müller, A.A. Naqvi, F. Käppeler, and F. Dickmann, Phys. Rev. C **29**, 885 (1984).

- [89] J. Khuyagbaatar, S. Hofmann, F.P. Heßberger, D. Ackermann, H.G. Burkhard, S. Heinz, B. Kindler, I. Kojouharov, B. Lommel, R. Mann, J. Maurer, K. Nishio, and Yu. Novikov, *Eur. Phys. J. A* **37**, 177 (2008).
- [90] D.C. Hoffman, and D. Lee, and A. Ghiorso, and M. Nurmia, and K. Aleklett, *Phys. Rev. C* **22**, 1581 (1980).
- [91] J. P. Unik, J. E. Gindler, L. E. Glendenin, K. F. Flynn, A. Gorski, R.K. Sjoblom, *Proc. Third IAEA Symp. on the physics and chemistry of fission, Rochester, 1973*, vol. II (IAEA, Vienna, 1974) p. 19.
- [92] J. P. Balagna, G. P. Ford, D. C. Hoffman, and J. D. Knight, *Phys. Rev. Lett.* **26**, 145 (1971).
- [93] E.K. Hulet, R.W. Lougheed, J.H. Landrum, J.F. Wild, D.C. Hoffman, J. Weber, and J.B. Wilhelmy, *Phys. Rev. C* **21**, 966 (1980).
- [94] H. C. Ragaini, E. K. Hulet, R. W. Lougheed, and J. Wild, *Phys. Rev. C* **9**, 399 (1974).
- [95] V.E. Viola, K. Kwiatkowski, and M. Walker, *Phys. Rev. C* **31**, 1550 (1985).
- [96] E.K. Hulet, J.F. Wild, R.J. Dougan, R.W. Lougheed, J.H. Landrum, A.D. Dougan, M. Schädel, R.L. Hahn, P.A. Baisden, C.M. Henderson, R.J. Dupzyk, K. Sümmerer, and G.R. Bethune, *Phys. Rev. Lett.* **56**, 313 (1986).
- [97] J.F. Wild, and J. van Aarle, and W. Westmeier, and R.W. Lougheed, and E.K. Hulet, and K.J. Moody, and R.J. Dougan, and E.-A. Koop, and R.E. Glaser, and R. Brandt, and P. Patzelt, *Phys. Rev. C* **41**, 640 (1990).
- [98] D.G. Madland and J.R. Nix, *Nucl. Sci. Eng.* **81**, 213 (1982).
- [99] S. Lemaire, P. Talou, T. Kawano, M.B. Chadwick, and D.G. Madland, *Phys. Rev. C* **72**, 024601 (2005).
- [100] N.V. Kornilov, F.-J. Hamsch, and A.S. Vorobyev, *Nucl. Phys. A* **789**, 55 (2007).
- [101] K.-H. Schmidt and B. Jurado, *Phys. Rev. Lett.* **104**, 212501 (2010).
- [102] A. Gilbert and A.G.W. Cameron, *Can. J. Phys.* **43**, 1446 (1965).
- [103] R. Vandenbosch and J.R. Huizenga, *Nuclear fission*, Academic Press, New York (1973).

- [104] V. Weisskopf, Phys. Rev. **52**, 295 (1937).
- [105] J. Randrup and R. Vogt, Phys. Rev. C **80**, 024601 (2009).
- [106] K. Nishio, Y. Nakagome, H. Yamamoto, and I. Kimura, Nucl. Phys. A **632**, 540 (1998).
- [107] V.F. Apalin, Y.N. Gritsyuk, I.E. Kutikov, V.I. Lebedev, and L.A. Miskaelian, Nucl. Phys. A **71**, 553 (1965).
- [108] A.S. Vorobyev, O.A. Shcherbakov, A.M. Gagarski, G.V. Val'ski and G.A. Petrov, EPJ Web of Conferences **8**, 03004 (2010).
- [109] O.I. Batenkov, V.P. Eismont, M.J. Majorov, A.N. Smirnov, K. Aleklett, W. Loveland, J. Blomgren, H. Condé, M. Duijvestijn, and A. Koning, AIP Conf. Proc. **769**, 625 (2005).
- [110] E.E. Maslin, A.L. Rodgers, and W.G.F. Core, Phys. Rev. **164**, 1520 (1967).
- [111] A. Göök, F.J. Hamsch, and S. Oberstedt, EPJ Web of Conferences **169**, 00004 (2018).
- [112] J.W. Boldeman and M.G. Hines, Nucl. Sci. Eng. **91**, 114 (1985).
- [113] A.I. Svirikhin, V.N. Dushin, M.L. Chelnokov, V.I. Chepigin, I.N. Izosimov, D.E. Katrasev, O.N. Malyshev, A. Minkova, A.G. Popeko, E.A. Sokol, and A.V. Yeremin, Eur. Phys. J. A **44**, 393 (2010).
- [114] A.I. Svirikhin, A.V. Andreev, V.N. Dushin, M.L. Chelnokov, V.I. Chepigin, M. Gupta, A.V. Isaev, I.N. Izosimov, D.E. Katrasev, A.N. Kuznetsov, O.N. Malyshev, S. Mullins, A.G. Popeko, E.A. Sokol, and A.V. Yeremin, Eur. Phys. J. A **48**, 121 (2012).
- [115] Yu. A. Lazarev, At. Energy Rev **15**, 75 (1977).
- [116] D.C. Hoffman, and G.P. Ford, and J.P. Balagna, and L.R. Veaser, Phys. Rev. C **21**, 637 (1980).
- [117] K.F. Flynn, and J.E. Gindler, and R.K. Sjoblom, and L.E. Glendenin, Phys. Rev. C **11**, 1676 (1975).
- [118] A.I. Svirikhin, M. Gupta, A.V. Yeremin, I.N. Izosimov, A.V. Isaev, A.N. Kuznetsov, O.N. Malyshev, S. Mullins, A.G. Popeko, E.A. Sokol, M.L. Chelnokov, and V.I. Chepigin, Bulletin of the Russian Academy of Sciences: Physics **79**, 442 (2015).

- [119] F. Gönnerwein, *Cold Fission*, Frontier Topics in Nuclear Physics (Eds. W. Scheid and A. Sandulescu), Springer US, Boston, MA, p. 113 (1994).
- [120] A.E.S Green, *Phys. Rev.* **95**, 1006 (1954).
- [121] H. Condo and M. Holmberg, *J. of Nuclear Energy* **25**, 331 (1971).
- [122] H.Thierens, E. Jacobs, P.D'hondt, D. De Frenne, A. De Clercq, P. De Gelder, A.J. Deruytter, J. Blachot, and P. Perrin, *Nucl. Phys. A* **342**, 229 (1980).
- [123] D.A. Hicks, J. Ise, and R.V. Pyle, *Phys. Rev.* **101**, 1016 (1956).
- [124] Z. Huanqiao, L. Zuhua, D. Shengyue, L. Shaoming, *Nuclear Science and Engineering* **86**, 315 (1984).
- [125] C.J. Orth, *Nuclear Science and Engineering* **43**, 54 (1971).
- [126] N.I. Kroshkin and Y.S. Zamyatnin, *At. Energy* **29**, 790 (1970).
- [127] A.S. Vorobyev, V.N. Dushin, F.-J. Hambsch, V.A. Jakovlev, V.A. Kalinin, A.B. Laptev, B.F. Petrov, and O.A. Shcherbakov, *AIP Conference Proceedings* **798**, 255 (2005).
- [128] V.N. Kosyakov, V.G. Nesterov, B. Nurpeisov, L.I. Prokhorova, G.N. Smirenkin, and I.K. Shvetsov, *At. Energy* **33**, 903 (1972).
- [129] A.I. Svirikhin, A.V. Yeremin, I.N. Izosimov, A.V. Isaev, A.N. Kuznetsov, O.N. Malyshev, A.G. Popeko, Yu.A. Popov, E.A. Sokol, M.L. Chelnokov, V.I. Chepigin, B. Andel, M.Z. Asfari, B. Gall, N. Yoshihiro, Z. Kalaninova, S. Mullins, J. Piot, E. Stefanova, and D. Tonev, *Phys. Part. Nuclei Lett.* **13**, 480 (2016).
- [130] A. Svirikhin, Ch. Briançon, S. Dmitriev, Yu. Oganessian, E. Sokol, D. Testov, and A. Yeremin, *AIP Conference Proceedings* **1175**, 297 (2009).
- [131] M. Haddad, J. Crançon, G. Lhospice, and M. Asghar, *Radiochimica* **46**, 23 (1989).
- [132] A.H. Jaffey and J.L. Lerner, *Nucl. Phys. A* **145**, 1 (1970).
- [133] M. Lindner and D.W. Seegmiller, *Radiochimica Acta* **49**, 1 (1990).
- [134] K.F. Flynn, J.E. Gindler, R.K. Sjoblom, and L.E. Glendenin, *Phys. Rev. C* **11**, 1676 (1975).

- [135] K.D. Zhuravlev et al., Proc. 2nd Nat. Conf. on Neutron Physics, 28 May-1 June 1973., Kiev, USSR, V.4, p.57 (1974).
- [136] A. Göök, F.-J. Hamsch, S. Oberstedt, and M. Vidali, Phys. Rev. C **98**, 044615 (2018).
- [137] A. Tudora, Eur. Phys. J. A **55**, 98 (2019).
- [138] S. Hofmann, *On Beyond Uranium: Journey to the End of the Periodic Table* (Taylor and Francis, London, 2002).
- [139] A.T. Chemey and T.E. Albrecht-Schmitt, Radiochim. Acta **107** 771 (2019).
- [140] P. Möller and J.R. Nix, Nucl. Phys. A **272**, 502 (1976).
- [141] P. Möller and A.J. Sierk, Nature, **422**, 485 (2003).
- [142] W.J. Swiatecki, K. Siwek-Wilczynska, and J. Wilczynski, Acta Phys. Pol. B **34**, 2049 (2003).
- [143] W.J. Swiatecki, K. Siwek-Wilczynska, and J. Wilczynski, Phys. Rev. C **71**, 014602 (2005).
- [144] J. Błocki, Y. Boneh, J.R. Nix, J. Randrup, M. Robel, A.J. Sierk, and W.J. Swiatecki, Ann. Phys. (N.Y.) **113**, 330 (1978).
- [145] D. Boilley, T. Cap, Y. Abe, B. Cauchois, and C. Shen, J. Phys. G: Nucl. Part. Phys. **46**, 115102 (2019).
- [146] R.S. Naik, W. Loveland, P.H. Sprunger, A.M. Vinodkumar, D. Peterson, C.L. Jiang, S. Zhu, X. Tang, E.F. Moore and P. Chowdhury, Phys. Rev. C **76**, 054604 (2007).
- [147] M.G. Itkis, E. Vardaci, I.M. Itkis, G.N. Knyazheva, E.M. Kozulin, Nucl. Phys. A **944**, 204 (2015).
- [148] E.M. Kozulin, and G.N. Knyazheva, and I.M. Itkis, and M.G. Itkis, and A.A. Bogachev, and E.V. Chernysheva, and L. Krupa, and F. Hanappe, and O. Dorvaux, and L. Stuttgé, and W.H. Trzaska, and C. Schmitt, and G. Chubarian, Phys. Rev. C **90**, 054608 (2014).
- [149] G. Scamps and C. Simenel, Nature **564**, 382 (2018).
- [150] N. Dubray, H. Goutte, and J.P. Delaroche, Phys. Rev. C **77**, 014310 (2008).

- [151] W.J. Swiatecki, K. Siwek-Wilczynska, and J. Wilczynski, Phys. Rev. C **78**, 054604 (2008).
- [152] J.J. Cowan, C. Sneden, J.E. Lawler, A. Aprahamian, M. Wiescher, K. Langanke, G. Martínez-Pinedo, F.-K. Thielemann, Rev. Mod. Phys. **93**, 015002 (2021).